

ABCA7 Loss-of-Function Variants Impact Phosphatidylcholine Metabolism in the Human Brain

Djuna von Maydell^{1,2}, Shannon Wright^{1,2}, Ping-Chieh Pao^{1,2}, Colin Staab^{1,2}, Oisín King^{1,2}, Andrea Spitaleri³, Julia Maeve Bonner^{1,2}, Liwang Liu^{1,2}, Chung Jong Yu^{1,2}, Ching-Chi Chiu^{1,2}, Daniel Leible^{1,2}, Aine Ni Scannail^{1,2}, Mingpei Li^{1,2}, Carles A. Boix^{4,5}, Hansruedi Mathys^{1,2,‡}, Guillaume Leclerc⁴, Gloria Suella Menchaca^{1,2}, Gwyneth Welch^{1,2}, Agnese Graziosi^{1,2}, Noelle Leary^{1,2}, George Samaan^{1,2}, Manolis Kellis^{4,5}, Li-Huei Tsai^{1,2,*}

¹Picower Institute for Learning and Memory, Massachusetts Institute of Technology, Cambridge, MA 02139, USA.

²Department of Brain and Cognitive Sciences, Massachusetts Institute of Technology, Cambridge, MA 02139, USA.

³Department of Medical Biotechnologies and Translational Medicine, University of Milano, Via F.lli Cervi 93, Segrate (MI), 20054 Italy.

⁴MIT Computer Science and Artificial Intelligence Laboratory, Cambridge, MA 02139, USA.

⁵Broad Institute of MIT and Harvard, Cambridge, MA 02139, USA.

[‡]Present address: Department of Neurobiology, University of Pittsburgh, Pittsburgh, PA 15261. *Corresponding author. Email: lhtsai@mit.edu

Abstract

Loss-of-function (LoF) variants in the lipid transporter ABCA7 significantly increase Alzheimer's disease risk (odds ratio ≈ 2), yet the underlying pathogenic mechanisms and specific neural cell types affected remain unclear. To investigate this, we generated a single-nucleus RNA sequencing atlas of 36 human *postmortem* prefrontal cortex samples, including 12 carriers of ABCA7 LoF variants and 24 matched non-carriers. ABCA7 LoF variants were associated with transcriptional changes across all major neural cell types. Excitatory neurons, which expressed the highest levels of ABCA7, showed significant

alterations in oxidative phosphorylation, lipid metabolism, DNA damage responses, and synaptic signaling pathways. ABCA7 LoF-associated transcriptional changes in neurons were similarly perturbed in carriers of the common AD missense variant ABCA7 p.Ala1527Gly (n = 240 controls, 135 carriers) - predicted by molecular dynamics simulations to disrupt ABCA7 structure -, indicating that findings from our study may extend to large portions of the at-risk population. Human induced pluripotent stem cell (iPSC)-derived neurons carrying ABCA7 LoF variants closely recapitulated the transcriptional changes observed in human *postmortem* neurons. Biochemical experiments further demonstrated that ABCA7 LoF disrupts mitochondrial membrane potential via regulated uncoupling, increases oxidative stress, and alters phospholipid homeostasis in neurons, notably elevating saturated phosphatidylcholine levels. Supplementation with CDP-choline to enhance *de novo* phosphatidylcholine synthesis effectively reversed these transcriptional changes, restored mitochondrial uncoupling, and reduced oxidative stress. Additionally, CDP-choline normalized amyloid- β secretion and alleviated neuronal hyperexcitability in ABCA7 LoF neurons. This study provides a detailed transcriptomic profile of ABCA7 LoF-induced changes and highlights phosphatidylcholine metabolism as a key driver in ABCA7-induced risk. Our findings suggest a promising therapeutic approach that may benefit a large proportion of individuals at increased risk for Alzheimer's disease.

¹ Introduction

² Over 50 million people worldwide have dementia, with a large fraction of cases caused by
³ Alzheimer's disease [1]. Late-onset Alzheimer's Disease (AD) affects individuals over the age
⁴ of 65 and accounts for more than 95% of all AD cases [2]. Though AD is a multifactorial
⁵ disorder, twin studies suggest a strong genetic component (70% heritability) [3] contributing
⁶ to AD disease risk and progression. Large scale genome-wide association studies implicate
⁷ multiple genes in AD etiology [4–10]. After APOE4, rare loss-of-function (LoF) mutations
⁸ caused by premature termination codons (PTCs) in ATP-binding cassette transporter A7
⁹ (ABCA7), are among the strongest genetic factors for AD (odds ratio ≈ 2) [9, 11–15]. In
¹⁰ addition to LoF variants, several common single nucleotide polymorphisms in ABCA7 -
¹¹ depending on the population - moderately [9, 11–13, 16–18] to strongly [13] increase AD risk,
¹² suggesting that ABCA7 dysfunction may play a role in a significant proportion of AD cases.
¹³ Despite the prevalence and potential impact of ABCA7 variants, the mechanism by which
¹⁴ ABCA7 dysfunction increases AD risk remains poorly characterized.

¹⁵ ABCA7 is a member of the A subfamily of ABC transmembrane proteins [19] with high
¹⁶ sequence homology to ABCA1, the primary lipid transporter responsible for cholesterol
¹⁷ homeostasis and high-density lipoprotein genesis in the brain [20]. ABCA7 effluxes both
¹⁸ cholesterol and phospholipids to APOA-I and APOE in *in vitro* studies [21–26] and has
¹⁹ been shown to be a critical regulator of energy homeostasis, immune cell functions, and
²⁰ amyloid processing [27–32]. To date, study of ABCA7 LoF has been predominantly pursued
²¹ in rodent knock-out models or in non-neural mammalian cell lines. These studies show that
²² ABCA7 knock-out or missense variants cause increased amyloid processing and deposition
²³ [33–36], reduced plaque clearance by astrocytes and microglia [37, 38], and glial-mediated
²⁴ inflammatory responses [39, 40]. While these studies shed light on potential mechanisms
²⁵ of ABCA7 risk in AD, studies investigating the effects of ABCA7 LoF in human cells and
²⁶ tissue are severely lacking, with only a small number published to date [30, 36, 41, 42]. These
²⁷ human studies highlight a number of potential LoF-induced defects in human cells, including
²⁸ impacts on lipid metabolism and mitochondrial function [30]. However, comprehensive and
²⁹ unbiased profiling of multiple human neural cell types is needed to elucidate the mechanism
³⁰ by which ABCA7 LoF increases AD risk.

³¹ Single-nucleus RNA sequencing (snRNA-seq) of human neural tissue has identified cell type-
³² specific transcriptional changes associated with AD risk variants in genes such as *APOE* and
³³ *TREM2* [43–47], providing insights into disease mechanisms and potential therapies. Here,
³⁴ we generated a cell type-specific transcriptomic atlas of ABCA7 LoF in the human prefrontal
³⁵ cortex (PFC). SnRNA-seq of *postmortem* brain tissue from ABCA7 LoF variant carriers and

36 matched controls revealed widespread transcriptional alterations, particularly in excitatory
37 neurons, which expressed the highest ABCA7 levels. Expression changes in these neurons
38 indicated disruptions in lipid metabolism, mitochondrial respiration, DNA damage response,
39 and synaptic function. Similar transcriptional changes were observed in neurons carrying
40 the common missense variant p.Ala1527Gly, which was predicted to impair ABCA7 function
41 based on structural simulations. This overlap indicates that p.Ala1527Gly may exert effects
42 comparable to ABCA7 LoF, extending the relevance of our findings to a broader group of
43 the at-risk population.

44 To complement our transcriptomic findings, we examined induced pluripotent stem cell
45 (iPSC)-derived neurons harboring ABCA7 LoF variants. These neurons exhibited significant
46 transcriptional overlap with human PFC neurons affected by ABCA7 LoF. Additionally, they
47 demonstrated impaired uncoupled mitochondrial respiration, hyperpolarized mitochondrial
48 membrane potential, elevated reactive oxygen species (ROS) levels, increased secretion of
49 amyloid- β (A β), and hyperexcitability. Consistent with ABCA7's known role in phospholipid
50 transport, we also observed alterations in lipid composition, notably an increase in saturated
51 phosphatidylcholine. Enhancing *de novo* phosphatidylcholine synthesis through CDP-choline
52 supplementation effectively reversed these ABCA7 LoF-induced transcriptional changes and
53 phenotypes. These findings link metabolic disruptions to AD pathology and suggest that
54 neuronal ABCA7 may impact mitochondrial function through phosphatidylcholine imbalance,
55 highlighting a potential mechanism by which ABCA7 variants increase AD risk.

56 Results

57 Single-nuclear transcriptomic profiling of human PFC from ABCA7 LoF-variant 58 carriers

59 To investigate the cell type-specific impact of ABCA7 LoF variants in the human brain, we
60 queried whole genome sequences of >1000 subjects from the Religious Order Study or the Rush
61 Memory and Aging Project (collectively known as ROSMAP) for donors with Alzheimer's
62 disease diagnoses who are carriers of rare damaging variants in ABCA7 that result in a PTC.
63 We identified 12 heterozygous carriers of ABCA7 LoF variants, including splice region variants
64 (c.4416+2T>G and c.5570+5G>C), frameshift variants (p.Leu1403fs and p.Glu709fs), and
65 nonsense 'stop gained' variants (p.Trp1245* and p.Trp1085*) (Figure ??A-C; Data ??).
66 These variants have previously been associated with increased AD risk in genetic association
67 studies (Table ??) [11, 14] and are presumed to induce risk via ABCA7 haploinsufficiency [48].
68 Analysis of published proteomic data for a subset of the 12 ABCA7 PTC-variant carriers

69 and controls [49] (Table ??) confirmed that ABCA7 PTC-variant carriers indeed had lower
70 ABCA7 protein levels in the human *postmortem* PFC compared to non-carriers ($p=0.018$;
71 Figure ??D; Figure ??A).

72 We next selected 24 ABCA7 PTC non-carrier controls from the ROSMAP cohort that were
73 matched to the ABCA7 LoF variant-carriers based on several potentially confounding variables,
74 including Alzheimer's disease (AD) pathology, age at death, *postmortem* intervals, sex, APOE
75 genotype, and cognitive status (Figure ??C; Figure ??B,C; Data ??; Supplementary Text).
76 We confirmed that none of the 36 selected subjects carried damaging variants in other known
77 AD risk genes (*TREM2*, *SORL1*, *ATP8B4*, *ABCA1*, and *ADAM10*) [14] and verified *ABCA7*
78 genotypes in a subset of ABCA7 LoF carriers and matched controls using Sanger sequencing
79 (Figure ??D).

80 For a subset of the selected samples, raw data (fastq files) for snRNAseq of the BA10 region
81 of the prefrontal cortex (PFC) could be obtained from a previous study (10 non-carrier
82 controls from [50]). For the remaining samples, fresh-frozen tissue samples from PFC BA10
83 were obtained for analysis. SnRNAseq was performed using the 10x Genomics Chromium
84 platform. Accurate genotype assignments were confirmed by matching each single-cell library
85 to its corresponding whole genome sequencing data (Figure ??E). Following extensive quality
86 control measures—including detailed analysis and correction of batch effects (Figure ??;
87 Data ??; Methods)—our final dataset consisted of 102,710 high-quality cells (Figure ??E), out
88 of an initial total of 150,456 cells. This dataset encompassed diverse populations of inhibitory
89 neurons (In, *SYT1* & *GAD1* +), excitatory neurons (Ex, *SYT1* & *NRGN* +), astrocytes
90 (Ast, *AQP4* +), microglia (Mic, *CSF1R* +), oligodendrocytes (Oli, *MBP* & *PLP1* +), and
91 oligodendrocyte precursor cells (OPCs, *VCAN* +) (Figure ??E; Figure ??A-E). A small
92 putative vascular cell cluster did not meet our quality thresholds and was excluded from
93 further analysis. Post-quality control, cell types were robustly represented across subjects
94 (Figure ??F,G), and gene expression profiles showed high consistency within cell types (mean
95 correlation 0.95) (Figure ??H,I).

96 Cell type-specific perturbations in the presence of ABCA7 LoF

97 To investigate gene expression changes related to ABCA7 LoF across major cell types, we
98 identified genes significantly perturbed ($p<0.05$, linear model; total genes = 2,389) in at least
99 one of six major cell types (Ex, In, Ast, Mic, Oli, or OPC). We controlled for known and
100 unknown covariates and considered only genes detected in $>10\%$ of cells within each specific
101 cell type (Methods; Data ??). Next, we visualized these perturbed genes by projecting their
102 high-dimensional perturbation scores (score = $\text{sign}(\log(\text{FC})) \times -\log_{10}(p\text{-value})$ for each cell

103 type) onto two dimensions, as shown in Figure ??F. Genes exhibiting similar perturbation
104 patterns across cell types are positioned closer together in this two-dimensional visualization.

105 The two-dimensional visualization effectively captured the transcriptional landscape of ABCA7
106 LoF gene changes across all major cell types (Figure ??F; Figure ??A). To summarize this
107 landscape in terms of biological pathways, we grouped genes into clusters based on their
108 positions in the projection and analyzed each cluster for enrichment in biological pathways
109 using the Gene Ontology Biological Process database (Figure ??G; Methods). This analysis
110 identified several biological pathways correlated with ABCA7 LoF in the *postmortem* human
111 PFC, including pathways related to cellular stress and apoptosis, synaptic function, DNA
112 repair, and metabolism (Figure ??G; Data ??).

113 Decomposition of the ABCA7 LoF transcriptional signature revealed both shared and cell-
114 specific gene perturbations across major PFC cell types (Figure ??G,H). Microglia exhibited
115 significant downregulation of genes involved in cellular stress responses (*e.g.*, *HSPH1*; cluster
116 11). A similar, though less pronounced, downregulation was observed in neurons and OPCs
117 (FDR-adjusted $p < 0.01$, $| \text{score} | > 0.25$; Figure ??H). Microglia and astrocytes showed
118 increased expression of transcriptional regulatory genes (clusters 9 and 10, respectively).
119 OPCs and oligodendrocytes demonstrated alterations in inflammatory signaling pathways
120 (*e.g.*, *IL10RB* in cluster 0 and *STAT2* in cluster 8; Figure ??H). Neurons displayed elevated
121 expression of DNA repair genes (*e.g.*, *FANCC*; cluster 12) and reduced expression of synaptic
122 transmission genes (*e.g.*, *NLGN1*, *SHISA6*; cluster 1). Excitatory neurons uniquely exhibited
123 enhanced expression of genes involved in cellular respiration (*e.g.*, *NDUFS2*; cluster 7) and
124 reduced expression of genes related to triglyceride biosynthesis (*e.g.*, *PPARD*; cluster 5;
125 Figure ??H). Overlapping differentially expressed genes across cell types are summarized in
126 Figure ??A,B.

127 Together, these findings indicate that ABCA7 LoF variants may induce widespread, cell
128 type-specific transcriptional changes in the human PFC. This single-cell atlas provides a
129 rich resource for future studies aiming to elucidate the contributions of individual neural
130 cell types to ABCA7 LoF-driven forms of AD risk. This resource will be made available for
131 exploration via the UCSC Single Cell Browser and for further analysis via Synapse (accession
132 ID: syn53461705).

133 ABCA7 is expressed most highly in excitatory neurons

134 Our snRNAseq data suggest that excitatory neurons expressed the highest levels of ABCA7,
135 compared to other major cell types in the brain (Figure ??A). ABCA7 transcripts were

¹³⁶ detected (count>0) in 30% of excitatory neurons and 15% of inhibitory neurons, while
¹³⁷ the detection rate was considerably lower (<10%) for microglia and astrocytes and an order
¹³⁸ of magnitude lower (<3%) for oligodendrocytes and OPCs (Figure ??A, B). We validated
¹³⁹ this expression pattern in an independent published dataset [51] (Table ??), where bulk
¹⁴⁰ RNA sequencing of NeuN- (glial) and NeuN+ (neuronal) cell populations derived from six
¹⁴¹ human *postmortem* temporal cortex samples showed significantly higher ABCA7 levels in
¹⁴² the neuronal population versus the glial cell population ($p=0.021$; Figure ??C). Several
¹⁴³ control genes, whose expression patterns in glial versus neuronal cells are well established
¹⁴⁴ (*ABCA1*, *APOE*, and *NEUROD1*), had expected expression patterns that matched those
¹⁴⁵ in the snRNAseq data (Figure ??B,C). These results indicate that neurons, particularly
¹⁴⁶ excitatory neurons, are the primary ABCA7-expressing cell type in the aged human PFC.
¹⁴⁷ Given the relatively higher expression of ABCA7 in excitatory neurons and the evidence of
¹⁴⁸ transcriptional perturbations by ABCA7 LoF in this cell type, we focused our subsequent
¹⁴⁹ analysis specifically on excitatory neurons.

¹⁵⁰ ABCA7 LoF perturbations in excitatory neurons

¹⁵¹ As an alternative approach to the unsupervised clustering of gene perturbation scores among
¹⁵² all cell types, we next used prior knowledge of biological pathway structure to perform
¹⁵³ an in-depth characterization of perturbed biological processes specifically in ABCA7 LoF
¹⁵⁴ excitatory neurons. To this end, we first estimated statistical overrepresentation of biological
¹⁵⁵ gene sets (WikiPathways, N pathways = 472) among up and down-regulated genes in ABCA7
¹⁵⁶ LoF excitatory neurons vs controls (by GSEA; Methods). We observed a total of 34 pathways
¹⁵⁷ with evidence for transcriptional perturbation at $p<0.05$ in excitatory neurons (Data ??).
¹⁵⁸ Enrichments of these pathways were driven by 268 unique genes (“leading edge” genes [52];
¹⁵⁹ Data ??).

¹⁶⁰ To extract unique information from leading-edge genes and limit pathway redundancy, we next
¹⁶¹ separated these genes and their associated pathway annotations into non-overlapping groups,
¹⁶² formalized as a graph partitioning problem (Figure ??A; Figure ??; Methods; Supplementary
¹⁶³ Text). Establishing gene-pathway groupings of approximately equal size revealed eight
¹⁶⁴ biologically interpretable “clusters” associated with ABCA7 LoF in excitatory neurons
¹⁶⁵ (Figure ??A,B; Data ??). Predominantly, these gene clusters centered around two themes: (1)
¹⁶⁶ energy metabolism and homeostasis (PM.0, PM.1) and (2) DNA damage (PM.2, PM.3), cell
¹⁶⁷ stress (PM.4, PM.5), and synaptic dysfunction (PM.7) (Figure ??B). **Cortical layer-specific**
¹⁶⁸ analysis indicated that these perturbation patterns remained largely consistent across cortical
¹⁶⁹ layers, from deeper to superficial regions (Figure ??).

170 Clusters PM.0 and PM.1 were primarily defined by genes involved in cellular energetics,
171 including genes related to lipid metabolism, mitochondrial function, and oxidative phospho-
172 rylation (OXPHOS) (Figure ??B). Cluster PM.0, characterized by transcriptional regulators
173 of lipid homeostasis (*e.g.*, *NR1H3*, *ACLY*, *PPARD*), exhibited evidence for down-regulation
174 in ABCA7 LoF and featured pathways related to "SREBP Proteins" and "Adipogenesis"
175 (Figure ??B; Data ??). Cluster PM.1 comprised multiple mitochondrial complex genes (*e.g.*,
176 *COX7A2*, *NDUFV2*) responsible for ATP generation from carbohydrate and lipid catabolism
177 and showed up-regulation in ABCA7 LoF (Figure ??B; Data ??). Clusters PM.2-6 were
178 characterized by DNA damage and proteasomal, inflammatory, and apoptotic mediators.
179 Clusters PM.2, PM.3, and PM.6 were up-regulated in ABCA7 LoF excitatory neurons and
180 characterized by pathway terms such as "DNA Damage Response" (PM.2 & PM.3) and "DNA
181 Replication" (PM.6) (Figure ??B; Data ??). They included up-regulated DNA damage/repair
182 and proteasomal genes (*e.g.*, *RECQL*, *TLK2*, *BARD1*, *RBL2*, *MSH6*, *PSMD5*). Genes in
183 clusters PM.4, linked to "Proteasome Degradation" and "ciliogenesis"; PM.5, associated with
184 "Apoptosis" and "TNFalpha Signaling Pathway"; and PM.7, linked to "GABA receptor Sig-
185 naling," "Gastric Cancer Network 1," and "Prader-Willi and Angelman Syndrome", included
186 both up- and down-regulated genes (Figure ??B; Data ??).

187 Together, these data suggest that ABCA7 LoF may disrupt energy metabolism in excita-
188 tory neurons and that these disruptions coincide with a state of increased cellular stress,
189 characterized by genomic instability and neuronal dysfunction.

190 **ABCA7 LoF and common missense variants lead to overlapping neuronal pertur-
191 bations**

192 ABCA7 LoF variants substantially increase AD risk (Odds Ratio = 2.03) [11] but are rare
193 and therefore only contribute to a small portion of AD cases [48]. To evaluate whether
194 ABCA7 LoF transcriptomic effects in neurons generalize to more common, moderate-risk
195 genetic variants in ABCA7, we examined the ROSMAP WGS cohort for carriers of the
196 prevalent ABCA7 missense variant p.Ala1527Gly (rs3752246: Minor Allele Frequency ≈
197 0.18; % carriers 1 allele ≈30%; Figure ??C). Although Gly1527 is listed as the reference
198 allele, it represents the less common variant associated with increased AD risk (Odds Ratio
199 = 1.15 [1.11-1.18]) [7, 14, 18]. We identified 133 individuals carrying at least one copy of the
200 p.Ala1527Gly risk variant and 227 non-carriers (Figure ??D), all with available snRNAseq
201 data from *postmortem* PFC [53]. We ensured that none of these 360 individuals were part of
202 our earlier ABCA7 LoF snRNAseq cohort or carried ABCA7 LoF variants. Using this cohort,
203 we investigated whether excitatory neurons from p.Ala1527Gly carriers exhibited evidence of

204 transcriptomic perturbations in the ABCA7 LoF-associated clusters PM.0-7.

205 Remarkably, all clusters displayed directional trends in p.Ala1527Gly neurons consistent with
206 the directionality observed in ABCA7 LoF neurons (Figure ??B,E,F), while controlling for
207 pathology, age, sex, and other covariates (Methods). Notably, 4 out of 8 clusters exhibited
208 substantial evidence of perturbation in p.Ala1527Gly variant carriers, with perturbation
209 directions aligning with predictions for ABCA7 LoF (Figure ??E,F). Specifically, we observed
210 an up-regulation in the DNA damage cluster PM.3 and the proteasomal cluster PM.4 in
211 p.Ala1527Gly carriers compared to controls, suggesting a similar cell stress and genomic
212 instability signature to ABCA7 LoF carriers (Figure ??E,F), and a borderline significant
213 up-regulation of the mitochondrial cluster PM.1, again consistent with ABCA7 LoF (Fig-
214 ure ??E,F). Finally, we observed significant perturbation to the lipid cluster PM.0, which
215 was down-regulated (Figure ??E,F) similar to our observations in ABCA7 LoF carriers.

216 Because missense variants often influence protein dynamics—and glycine substitutions typ-
217 ically introduce greater local flexibility than alanine—we next examined whether the con-
218 vergent transcriptional signature associated with ABCA7 variants could be explained by
219 structural changes in the protein. To directly investigate local structural consequences
220 of the p.Ala1527Gly variant, we performed molecular dynamics simulations using newly
221 available cryo-EM structures of ABCA7 in both the ATP-bound closed (Figure ??G,H) and
222 ATP-unbound open (Figure ??A,B) conformations [54, 55]. Specifically, simulations were
223 conducted on a 239-residue region of ABCA7 embedded within a lipid bilayer, comparing the
224 Ala1527 and Gly1527 variants over a 300-ns timescale (Figure ??I; Figure ??C; Figure ??;
225 Methods; Supplementary Text).

226 Our simulations revealed that the AD risk-associated Gly1527 variant increased local structural
227 flexibility in the ATP-bound closed conformation, indicated by pronounced conformational
228 fluctuations over time (Figure ??J). In contrast, the Ala1527 variant exhibited limited
229 conformational fluctuations, suggesting minimal local structural flexibility in the closed state
230 (Figure ??J). Both variants demonstrated stable conformational behavior in the ATP-unbound
231 open state (Figure ??C-E). These results are further supported by analyses of ϕ/ψ dihedral
232 angle distributions and secondary structure persistence, as detailed in the Supplementary
233 Text (Figure ??).

234 Together, these data suggest that the Gly1527 variant may introduce increased local flexibility,
235 potentially disrupting the stability of secondary structural elements specifically within the
236 ATP-bound closed conformation. Given that this conformation is proposed to mediate lipid
237 presentation to apolipoproteins [26, 54], the p.Ala1527Gly substitution may impact the

efficiency of lipid extrusion, consistent with recent experimental findings from [26]. Combined with our transcriptomics analyses, these structural insights suggest that both rare, high-effect ABCA7 LoF variants and common, mild-effect variants may influence AD risk through similar ABCA7-dependent mechanisms, indicating that our in-depth studies of rare variants may generalize to broader at-risk populations.

Deriving human neurons with ABCA7 LoF variants

To complement the correlative analyses in ABCA7 LoF human tissue, we next used CRISPR-Cas9 genome editing to generate two isogenic iPSC lines, each homozygous for a different ABCA7 LoF variant, from a parental line without ABCA7 variants (WT). The first LoF variant, ABCA7 p.Glu50fs*3, was generated by a single base-pair insertion in ABCA7 exon 3, resulting in a PTC early in the ABCA7 gene (Figure ??A; Figure ??A-C). The second LoF variant, ABCA7 p.Tyr622*, was generated by a single base-pair mutation in ABCA7 exon 15 (Figure ??A; Figure ??A-C). This PTC re-creates a variant previously observed in patients as associated with AD [11] and thus provides clinical context to ABCA7 dysfunction. Both variants are expected to generate severely truncated ABCA7 proteins or, due to nonsense-mediated mRNA decay, no ABCA7 protein at all. However, transcript rescue from nonsense-mediated decay and possible generation of mutated forms of ABCA7 through mechanisms such as exon skipping, which have previously been reported for multiple ABCA7 LoF variants [56], cannot be excluded.

We differentiated isogenic iPSCs into neurons (iNs) via lentiviral delivery of a doxycycline-inducible NGN2 expression cassette as previously described [57] (Figure ??A). At 2 and 4 weeks post-NGN2 induction, cells expressed neuronal markers TUJ1 and MAP2 and exhibited robust neuronal processes as demonstrated by pan-axonal staining (Figure ??B,C). Both WT and ABCA7 LoF lines were capable of firing action potentials upon current injections (Figure ??A,B). Although the ABCA7 genotype did not alter resting membrane potential (Figure ??E), ABCA7 LoF iNs fired action potentials more readily and at lower current injection thresholds compared to WT iNs (Figure ??F,G), indicating a hyperexcitability phenotype. Collectively, these data confirm successful neuronal differentiation from iPSCs, robust electrophysiological activity, and recapitulation of Alzheimer's disease-associated neuronal hyperexcitability.

ABCA7 LoF iNs Recapitulate Excitatory Neuronal Transcriptional Signatures

To investigate whether transcriptional changes associated with ABCA7 LoF observed in *postmortem* human neurons are recapitulated in iNs, we performed bulk mRNA sequencing on

²⁷¹ ABCA7 WT, p.Glu50fs*3, and p.Tyr622* iNs (N=2, N=5, and N=5, respectively) after four
²⁷² weeks in culture (Data ??). Gene perturbation scores (defined as score = sign(log(FC)) ×
²⁷³ − log₁₀(p-value)) showed a strong correlation between p.Glu50fs*3 vs. WT and p.Tyr622* vs.
²⁷⁴ WT comparisons (Pearson correlation coefficient = 0.84; Figure ??B), indicating consistency
²⁷⁵ in the transcriptional impact of ABCA7 variants.

²⁷⁶ We next conducted gene set enrichment analysis (GSEA) on the differentially expressed genes
²⁷⁷ from these comparisons, identifying 15 significantly perturbed pathways in each comparison,
²⁷⁸ p.Glu50fs*3 vs. WT and Y in p.Tyr622* vs. WT (FDR-adjusted p < 0.05; WikiPathways).
²⁷⁹ These pathways were driven by 356 and 334 unique "leading edge" genes, respectively [52].
²⁸⁰ K/L partitioning of these leading edge genes identified 9 clusters for p.Tyr622* (Figure ??C)
²⁸¹ and 10 clusters for p.Glu50fs*3 (Figure ??A). Eight of nine p.Tyr622* T clusters and eight of
²⁸² ten p.Glu50fs*3 G clusters showed significant overlap (FDR-adjusted p < 0.05) (Figure ??B),
²⁸³ indicating substantial concordance between the two ABCA7 variant lines.

²⁸⁴ We also observed that transcriptional signatures in ABCA7 LoF iNs closely aligned with those
²⁸⁵ identified in *postmortem* excitatory neurons. Specifically, we found significant overlap in 5
²⁸⁶ out of 9 p.Tyr622*-associated clusters (Figure ??D) and in 7 out of 10 p.Glu50fs*3-associated
²⁸⁷ clusters (Figure ??C) with the clusters identified in *postmortem* excitatory neurons, with the
²⁸⁸ majority (4 out of 5 and 6 out of 7, respectively) showing concordant directional changes.

²⁸⁹ Due to the transcriptional similarity between the two LoF lines, our primary analysis
²⁹⁰ focuses on the patient variant p.Tyr622*, with results for the p.Glu50fs*3 variant provided
²⁹¹ in supplementary materials (Figure ??). Consistent with findings from *postmortem* data,
²⁹² p.Tyr622* iNs exhibited downregulated clusters associated with lipid metabolism (T.9 and
²⁹³ T.13) and upregulated clusters related to cell cycle regulation and proteasomal activity
²⁹⁴ (T.8 and T.14) compared to WT iNs (Figure ??E). Notably, a mitochondrial cluster (T.10)
²⁹⁵ demonstrated the most robust overlap with *postmortem* data (PM.1) and was consistently up-
²⁹⁶ regulated in both the p.Tyr622* and p.Glu50fs*3 lines, mirroring the findings in *postmortem*
²⁹⁷ neurons (Figure ??D; Figure ??C). The probability of observing this degree of overlap by
²⁹⁸ chance alone is very low ($p < 5 \times 10^{-5}$ in both cases, binomial test). Together, these data
²⁹⁹ support a causal relationship between ABCA7 LoF variants and multiple transcriptional
³⁰⁰ signatures observed in *postmortem* excitatory neurons, including mitochondrial, proteasomal,
³⁰¹ cell cycle, and lipid metabolism components.

302 **ABCA7 LoF impairs mitochondrial uncoupling in neurons**

303 To further characterize mitochondrial alterations in ABCA7 LoF iNs, extending beyond the
304 gene sets used for K/L cluster analysis, we examined the expression of 1,136 mitochondrial
305 genes curated from the MitoCarta database in our bulk RNAseq data. Among the most
306 significantly upregulated genes in p.Tyr622* versus WT iNs were genes encoding components
307 of mitochondrial apoptosis pathways (e.g., *CASP3*, *BID*) and OXPHOS subunits (previously
308 captured in clusters PM.1 and T.10) (Figure ??F; Table ??). Conversely, downregulated genes
309 were significantly enriched ($\text{padj} < 0.05$) for key metabolic processes, including β -oxidation
310 (*ACAD* and *CPT* genes), mitochondrial metabolite transport (*SLC25* genes), and oxidative
311 stress detoxification (*CAT*) (Figure ??F; Table ??). These MitoCarta mitochondrial gene
312 expression profiles were highly correlated between p.Tyr622* and p.Glu50fs*3 relative to WT
313 iNs (Figure ??E).

314 To directly assess mitochondrial function in ABCA7 LoF neurons, we measured the oxygen
315 consumption rate (OCR) of WT and ABCA7 LoF iNs over time using the Seahorse metabolic
316 flux assay (Figure ??A,B). The OCR-driven movement of protons across the inner mito-
317 chondrial membrane during OXPHOS builds and maintains the mitochondrial membrane
318 potential ($\Delta\Psi_m$) (Figure ??C), and measuring OCR in the presence of mitochondrial in-
319 hibitors provides several functional readouts. Because OCR can be influenced by cell viability
320 and mitochondrial abundance [58, 59], we only report internally normalized OCR ratios rather
321 than absolute values [60] for WT, ABCA7 p.Glu50fs*3, and ABCA7 p.Tyr622* iNs. To assess
322 the spare respiratory capacity, we normalized the OCR measured following pharmacological
323 collapse of the proton gradient to the basal OCR, with higher values indicating more spare
324 respiratory capacity [60] (Figure ??D). We then quantified the proportion of basal oxygen
325 consumption that can be attributed to rebuilding the membrane potential lost due to proton
326 leakage through the membrane (i.e., uncoupled mitochondrial OCR) rather than due to ATP
327 synthesis [60] (Figure ??E).

328 While spare respiratory capacity was comparable between WT and ABCA7 LoF iNs (Fig-
329 ure ??F), ABCA7 LoF iNs showed significantly reduced uncoupled mitochondrial respiration
330 (Figure ??G). Uncoupled mitochondrial oxygen consumption rates in WT iNs ($\approx 20\%$; Fig-
331 ure ??G) align with previously reported values for neurons and other cell types [61–63],
332 indicating that ABCA7 LoF iNs exhibit abnormally low mitochondrial uncoupling. Consistent
333 with this observation, expression levels of UCP2 - a member of the mitochondrial uncoupling
334 protein family expressed in the brain [64] - were reduced in ABCA7 LoF iNs (Figure ??G).
335 Because decreased mitochondrial uncoupling often correlates with elevated mitochondrial

membrane potential ($\Delta\Psi_m$) [65, 66], we next assessed $\Delta\Psi_m$ in NeuN-positive soma using the fixable MitoHealth dye, which accumulates in mitochondria proportionally to membrane potential. We observed significantly increased MitoHealth fluorescence in both p.Tyr622* and p.Glu50fs* iNs compared to WT per NeuN surface (Figure ??H). To further confirm these findings, we measured $\Delta\Psi_m$ in soma and neuronal processes using the fluorescent cation tetramethylrhodamine methyl ester (TMRM) in non-quenching mode. TMRM accumulation was higher in p.Tyr622* iNs relative to WT (Figure ??I), and the specificity of this TMRM signal was validated by showing drastically reduced TMRM signal intensity after depolarization of the $\Delta\Psi_m$ with the uncoupler FCCP (Figure ??H). Together, these results indicate that ABCA7 LoF iNs exhibit elevated $\Delta\Psi_m$.

Regulated mitochondrial uncoupling serves as a mechanism to control mitochondrial membrane potential and mitigate reactive oxygen species (ROS) generation [65, 67]. To assess whether ABCA7 LoF iNs exhibited elevated ROS levels, we incubated p.Tyr622* iNs with CellROX dye, a fluorescent indicator of oxidative stress. We observed significantly increased CellROX fluorescence in p.Tyr622* iNs compared to WT iNs (Figure ??J), indicating elevated ROS accumulation in ABCA7 LoF iNs. Together, these data suggest that ABCA7 LoF variants decrease mitochondrial uncoupling and increase oxidative stress in neurons.

ABCA7 LoF induces phosphatidylcholine imbalance in neurons

Since ABCA7 functions as a lipid transporter, we examined the lipidome of WT and ABCA7 LoF iNs using LC-MS (Data ??). Comparing lipidomic profiles between WT and p.Glu50fs*3 iNs revealed significant alterations across multiple lipid classes, including neutral lipids, phospholipids, sphingolipids, and steroids (Figure ??A,B). Among these, triglycerides (TGs)—particularly species enriched in long-chain, predominantly polyunsaturated fatty acids—were frequently altered, showing significant upregulation in p.Glu50fs*3 iNs (Figure ??B,C).

In line with ABCA7's established preference for phospholipids [26, 68, 69], several phospholipid species also exhibited notable differences (Figure ??B). Phosphatidylcholines (PCs), which are essential structural components of biological membranes and potential ABCA7 substrates [26, 54], were most prominently affected; the majority ($\approx 64\%$ of perturbed PC species) showed increased abundance in p.Glu50fs3 iNs (Figure ??B). Further analysis based on fatty acid saturation—an important factor influencing membrane fluidity—revealed significant enrichment of saturated PCs among the upregulated species (hypergeometric $p=0.026$) (Figure ??D). In contrast, polyunsaturated fatty acid-containing (PUFA) PCs showed mixed directionality, with several highly unsaturated species showing decreased abundance (e.g.,

³⁷⁰ PC(44:7) and PC(38:7)) (Figure ??E,F).

³⁷¹ To determine whether neutral lipid and PC imbalances were conserved in p.Tyr622* iNs,
³⁷² we performed targeted lipidomic analysis in positive ionization mode. Consistent with
³⁷³ p.Glu50fs*3 iNs, upregulated lipids in p.Tyr622* iNs were significantly enriched for saturated
³⁷⁴ PCs (hypergeometric $p=0.044$) (Figure ??K; Figure ??G,H). However, PUFA PCs and
³⁷⁵ long-chain triglycerides were not reliably detected in this LC-MS run (Figure ??I,J), leaving
³⁷⁶ it unclear whether p.Tyr622* iNs exhibit the same changes in PUFA PC or long-chain
³⁷⁷ triglycerides as p.Glu50fs*3 iNs.

³⁷⁸ *De novo* PC synthesis occurs via the Kennedy pathway, and subsequent remodeling of the
³⁷⁹ fatty acyl chains is catalyzed by LPCAT enzymes through the Lands cycle, with LPCAT3
³⁸⁰ specifically introducing PUFA chains into PCs [70–72]. LPCAT3 expression was reduced in
³⁸¹ p.Tyr622* and p.Glu50fs*3 iNs compared to WT (Figure ??K,L), aligning with increased
³⁸² levels of saturated PCs in these cells. Overall, our data indicate accumulation of neutral
³⁸³ lipids in ABCA7 LoF iNs, including long-chain polyunsaturated triglycerides and sterol lipids
³⁸⁴ (zymosterol), and reveal imbalances in PC composition, with higher saturated species.

³⁸⁵ Treatment with CDP-choline reverses impacts of ABCA7 LoF in neurons

³⁸⁶ Previous work indicated that exogenous choline supplementation normalized phospholipid
³⁸⁷ saturation levels in yeast and ameliorated APOE4-related lipid phenotypes [73, 74]. We
³⁸⁸ therefore next examined whether CDP-choline treatment could similarly mitigate ABCA7
³⁸⁹ LoF-induced phenotypes in iNs.

³⁹⁰ Targeted LC-MS analysis confirmed that CDP-choline treatment increased its concentration
³⁹¹ in the media from undetectable to detectable levels (Figure ??A). Additionally, both CDP
³⁹² and choline specifically accumulated in media conditioned by p.Tyr622* cells after treatment
³⁹³ (Figure ??A), indicating extracellular hydrolysis of CDP-choline. While intracellular CDP
³⁹⁴ and CDP-choline could not reliably be detected in this experiment, intracellular choline
³⁹⁵ levels significantly increased after treatment (Figure ??B) and expression levels of choline
³⁹⁶ transporters were significantly upregulated (Figure ??C). This suggests that choline was
³⁹⁷ successfully taken up by p.Tyr622* iNs upon CDP-choline treatment.

³⁹⁸ We anticipated that higher intracellular choline availability would lead to increased phos-
³⁹⁹ pholipid synthesis. Lipidomic analysis indeed revealed elevated levels of phospholipids,
⁴⁰⁰ particularly choline-containing phospholipids (PC and lysophosphatidylcholines (LPC)) and
⁴⁰¹ sphingolipids (sphingomyelins (SM)), alongside a reduction in a single TG species, with
⁴⁰² other neutral lipid species showing a similar downward trend (Figure ??A). Consistent with

these changes, we observed increased expression of *PCYT1B*, the enzyme responsible for the rate-limiting step in PC synthesis through the Kennedy pathway (Figure ??C). Additionally, expression of several LPCAT genes, including *LPCAT3*, was elevated after treatment (Figure ??D), coinciding with observed increases in both saturated and unsaturated PC species (Figure ??A; Figure ??E). These findings suggest that CDP-choline treatment promotes synthesis and remodeling of choline-containing lipids.

Next, we characterized changes induced by CDP-choline treatment using LC-MS-based metabolomics and bulk RNAseq. While most of the metabolites increasing or decreasing after treatment could not be annotated, a principal component analysis of the overall metabolite changes indicated that CDP-choline treatment reversed the separation of WT and pTyr622* iN along the axis of the first principal component (PC1; Figure ??F). Transcriptionally, CDP-choline treatment also induced significant changes, clearly distinguishing treated from untreated samples (Figure ??G). The transcriptional signature of CDP-choline treatment negatively correlated with that of p.Tyr622* (Figure ??B), suggesting partial restoration toward the WT state. Performing K/L cluster analysis on the p.Tyr622* vs CDP-choline treated p.Tyr622* samples (Figure ??C), we observed significant overlap in 7 of the 9 clusters identified in the p.Tyr622* vs WT comparison (Figure ??D), with 5 of these clusters showing reversed directional changes following treatment (Figure ??E).

Specifically, clusters related to proteasomal and ribosomal functions (T+C.25 and T+C.31)—previously upregulated in p.Tyr622* (see T.14 and T.12)—were downregulated following CDP-choline treatment (Figure ??D). Most notably, mitochondrial cluster T+C.26—which strongly overlapped with cluster T.10, the cluster most consistent with *postmortem* PM.1—was also reversed after treatment (Figure ??E). Further analysis using the MitoCarta database confirmed a significant reversal in expression of genes encoding mitochondrial proteins, including reduced expression of apoptosis-related genes (*BID*, *CASP3*; Figure ??F), restoration (upregulation) of the mitochondrial metabolic signature (Table ??), and increased expression of regulators of mitochondrial fusion (*MFN2*, *OPA1*), a process which enables high metabolic capacity, dissipation of mitochondrial membrane potential, and mitochondrial biogenesis [75]. Overall, ABCA7 LoF-related changes to expression of MitoCarta genes were significantly reversed following CDP-choline treatment (Figure ??H).

To determine whether CDP-choline treatment could restore mitochondrial uncoupling to WT levels, we repeated the Seahorse assay on p.Tyr622* iNs with and without CDP-choline treatment (Figure ??I,J). CDP-choline treatment significantly increased uncoupled respiration in p.Tyr622* iNs, restoring it to WT levels (Figure ??G), with no significant change in

438 spare respiratory capacity (Figure ??K). Consistent with this finding, both TMRM staining
439 (Figure ??H) and MitoHealth fluorescence per NeuN-positive surface (Figure ??L) confirmed
440 a decrease in the mitochondrial membrane potential ($\Delta\Psi_m$) in treated cells. Additionally,
441 CDP-choline treatment significantly decreased CellROX fluorescence (Figure ??I), indicating
442 a reduction in oxidative stress.

443 CDP-Choline Ameliorates AD-Associated Phenotypes in Cortical Organoids

444 Next, we tested whether CDP-choline treatment could improve key AD-associated phenotypes,
445 since previous studies have linked ABCA7 dysfunction to altered amyloid- β (A β) processing
446 [33–36, 76]. Indeed, p.Tyr622* iNs secreted significantly higher levels of A β 40 and showed a
447 trending increase in A β 42 secretion into the media, as measured by enzyme-linked immunosor-
448 bent assay (ELISA), although absolute levels remained relatively low (Figure ??A). To study
449 CDP-choline’s effects in a model with stronger pathology, we differentiated p.Tyr622* and
450 WT lines into cortical organoids matured for \approx 6 months (Figure ??B), a stage at which
451 we observed robust A β secretion (approximately two- to four-fold higher levels of A β 40 and
452 A β 42 compared to iNs)(Figure ??C). Treatment with 1 mM CDP-choline for four weeks
453 reduced A β 40 and A β 42 secretion from p.Tyr622* organoids to WT levels (Figure ??K). This
454 effect was not observed at lower concentrations or shorter treatment durations (Figure ??C).
455 Additionally, treatment of dissociated cortical organoids with 100 μ M CDP-choline for two
456 weeks significantly reduced neuronal hyperexcitability in p.Tyr622* organoids, as shown by
457 electrophysiology (Figure ??K).

458 Discussion

459 Loss-of-function (LoF) mutations in the lipid transporter ABCA7 are among the strongest
460 genetic risk factors for late-onset AD. Here, we generated a transcriptional atlas of ABCA7
461 LoF effects across all major brain cell types in the human prefrontal cortex. Our dataset
462 showed the highest levels of ABCA7 expression in excitatory neurons and strong evidence
463 that ABCA7 LoF led to transcriptional perturbation in pathways related to lipid biosynthesis,
464 mitochondrial respiration, and cellular stress, including up-regulation of DNA damage path-
465 ways, and changes to inflammatory and synaptic genes. Using iPSC-derived isogenic neuronal
466 lines (iN) with and without ABCA7 LoF variants, we show that ABCA7 LoF leads to de-
467 creased mitochondrial uncoupling, elevated mitochondrial membrane potential, and increased
468 reactive oxygen species (ROS). Consistent with ABCA7’s role as a phospholipid transporter,
469 ABCA7 LoF iNs exhibited significant imbalances in phosphatidylcholine composition, char-
470 acterized by increased saturated PCs and a decrease to several highly polyunsaturated

⁴⁷¹ (PUFA) PCs. Similar changes in phospholipid saturation were recently observed in neuronal
⁴⁷² models of ALS/FTD, highlighting the broader significance of phospholipid saturation in
⁴⁷³ neurodegenerative conditions [77]. Treatment of ABCA7 LoF iN with CDP-choline increased
⁴⁷⁴ phosphatidylcholine synthesis, upregulated expression of phosphatidylcholine remodeling
⁴⁷⁵ enzymes, and rescued mitochondrial uncoupling, mitochondrial membrane potential, and
⁴⁷⁶ oxidative stress. In addition, CDP-choline supplementation mitigated hyperexcitability and
⁴⁷⁷ amyloid- β secretion in ABCA7 LoF neurons. Together, our data indicate that the observed
⁴⁷⁸ effects of ABCA7 LoF on neurons may be at least partially mediated by imbalances in
⁴⁷⁹ phosphatidylcholine metabolism.

⁴⁸⁰ While the precise mechanism linking ABCA7 LoF to phosphatidylcholine imbalance remains
⁴⁸¹ unclear, disrupted ABCA7 floppase activity—responsible for phospholipid flipping across
⁴⁸² membrane leaflets—likely impacts membrane fluidity and curvature [78, 79], important
⁴⁸³ determinants of numerous cellular functions [80, 81]. Changes in membrane composition
⁴⁸⁴ may also broadly affect lipid metabolism by altering the activity of transcriptional regulators
⁴⁸⁵ controlling lipid biosynthesis and remodeling genes (including LPCATs), which are responsive
⁴⁸⁶ to shifts in membrane properties [82, 83]. Consistent with our observations and previous
⁴⁸⁷ reports, CDP-choline supplementation supports *de novo* synthesis of phosphatidylcholine
⁴⁸⁸ species containing both saturated and polyunsaturated fatty acids [84]. Thus, CDP-choline
⁴⁸⁹ may help restore phosphatidylcholine balance in ABCA7 LoF neurons by supporting the
⁴⁹⁰ synthesis and remodeling of diverse phosphatidylcholine species. Given that phosphatidyl-
⁴⁹¹ choline species are ubiquitous components of biological membranes—including abundant lipids
⁴⁹² within mitochondrial membranes [85]—imbalances in their fatty acyl chain composition could
⁴⁹³ broadly impact cellular functions [71, 86], including mitochondrial activity. Indeed, alterations
⁴⁹⁴ in phospholipid saturation and composition have been linked to changes in mitochondrial
⁴⁹⁵ dynamics, cristae morphology, bioenergetics, and membrane potential [85, 87]. However,
⁴⁹⁶ additional studies are needed to clarify the precise mechanisms by which phosphatidylcholine
⁴⁹⁷ imbalances influence mitochondrial function and uncoupling dynamics.

⁴⁹⁸ Mitochondrial dysfunction, including impaired mitochondrial uncoupling, is increasingly
⁴⁹⁹ recognized as critical in aging, AD, and other neurodegenerative diseases. Although mito-
⁵⁰⁰ chondrial uncoupling was recently linked to frontotemporal dementia, its specific role in AD
⁵⁰¹ remains poorly investigated [88–91]. Neurons maintain high mitochondrial OXPHOS to meet
⁵⁰² their significant energy demands [92, 93]. Mitochondrial uncoupling, actively regulated by
⁵⁰³ mitochondrial proteins [94], supports mitochondrial health by modulating mitochondrial
⁵⁰⁴ membrane potential, reducing reactive oxygen species [90, 95], and promoting mitochondrial
⁵⁰⁵ biogenesis [96–98]. Impaired mitochondrial uncoupling, as observed in ABCA7 LoF neurons,

506 can elevate oxidative stress, impair synaptic and calcium signaling, and contribute to neurode-
507 generation [96–98]. Increased oxidative stress also triggers DNA damage and inflammatory
508 responses [99–102], which are elevated in the presence of ABCA7 LoF based on transcriptomic
509 signatures.

510 In line with our findings linking phosphatidylcholine imbalances to mitochondrial impairments
511 in ABCA7 LoF neurons, a recent study in ABCA7 deficient neurospheroids independently
512 revealed a link between phosphatidylglycerol deficiency and mitochondrial function [30],
513 further highlighting the importance of lipid-centric therapeutic interventions for ABCA7
514 LoF. Here, we offer a therapeutic strategy to reverse these dysfunctions - including ABCA7
515 LoF-induced AD pathology and neuronal hyperexcitability -through CDP-choline treatment,
516 a readily available and safe dietary supplement [103–105]. Recent work from our lab implicates
517 phosphatidylcholine and fatty acyl saturation imbalances in APOE4 dysfunction [74], and in
518 cognitive resilience to AD pathology [106], suggesting that phosphatidylcholine disruptions
519 may be central to AD risk in large fractions of the population. Indeed, our work suggests that
520 the common missense variant p.Ala1527Gly likely has convergent effects with ABCA7 LoF.
521 Genetic interactions with other risk factors, including APOE4, may exacerbate otherwise
522 subtle ABCA7 dysfunction, and contribute to risk in a significant subset of AD cases [107–110].
523 As such, our study supports a growing body of literature, including recent studies on APOE4
524 [111, 112] that implicates lipid disruptions in the etiology of AD, and pinpoints additional
525 genotypes that may benefit from interventions on phosphatidylcholine metabolism.

526 **Acknowledgments:** We thank the individuals who donated postmortem brain samples,
527 and their families, for enabling this research; Y. Zhou, E. McNamara and T. Garvey for
528 administrative support and animal care; U. Geigenmüller for reviewing and editing the
529 manuscript and for helpful discussions; Rebecca Pinals for helpful discussions and input on
530 the manuscript; J. Davila-Velderrain and R. Firenze for providing input on the manuscript;
531 the MIT SuperCloud and Lincoln Laboratory Supercomputing Center for providing HPC
532 and consultation resources that have contributed to the research results reported within this
533 paper; the Harvard Center for Mass Spectrometry (HCMS) for lipidomic and metabolomic
534 sample runs and Charles Vidoudez (HCMS) for consultation on the lipidomic data analysis;
535 the MIT BioMicro Center for bulk and single-nucleus RNA-sequencing runs and Stuart Levine
536 and his Team for consultations on data processing; ROSMAP resources can be requested at
537 <https://www.radc.rush.edu>. Graphic illustrations were generated using BioRender under
538 agreement # X25SQ61W7.

539 **Funding:** This work was supported in part by the Cure Alzheimer's Fund, The Freedom
540 Together Foundation, the Carol and Gene Ludwig Family Foundation, James D. Cook
541 and NIH grants R56-AG081376, RF1-AG062377, RF1-AG054321, RO1-AG054012 (L.-H.T.),
542 and RO1-AG075901 (P.I. Ernest Fraenkel).

543 **Author contributions:** DVM and L-HT designed the study, with L-HT supervising the
544 overall project and acquiring funding alongside MK. Experimental work included snRNA-seq
545 experiments performed by DVM, JMB, HR, and LL; Seahorse assays conducted by SEW;
546 and differentiation and maintenance of iPSC lines, induced neurons, and cortical organoids
547 by SEW, CS, P-CP, and OK. SEW and P-CP prepared samples for LC-MS analysis and
548 performed amyloid ELISA experiments and neuronal marker staining. P-CP conducted
549 TMRM and CellRox assays and SEW performed MitoHealth assays. P-CP, CS, and OK
550 prepared bulk RNA samples. LL conducted electrophysiological recordings and analysis,
551 and CJY generated the p.Tyr622* cell line. AS performed molecular dynamic simulations,
552 analyses, and visualizations and DVM performed formal data analysis and visualization, with
553 contributions from C-AB, GL, and AS. Experimental and technical support was provided by
554 A-NS, ML, G-SM, GW, AG, NL, and GS. C-CC and DL helped with revision experiments.
555 DVM, SEW, and L-HT wrote the first draft of the manuscript. DVM and L-HT wrote the
556 revised draft of the manuscript.

557 **Competing interests:** Authors declare that they have no competing interests.

558 **Ethics Statement:** The study protocol involving the use of human stem cells was approved
559 by the Coriell Institutional Review Board (Coriell IRB) in compliance with DHHS regulations
560 (45 CFR Part 46). The initial cell lines were obtained from the Coriell Institute, which
561 ensured that informed consent was received from all donors. Donors were informed that their
562 tissue donations would be used for the creation of cell lines intended for educational and
563 research purposes, and that all biological materials would be anonymized. More information
564 can be found here. For postmortem human brain samples, informed consent was obtained
565 from each subject, and the Religious Orders Study and Rush Memory and Aging Project
566 were approved by an Institutional Review Board (IRB) of Rush University Medical Center.

567 **Data availability:** All postmortem human data can be accessed through the Synapse AD
568 Knowledge Portal (syn53461705), which also includes associated ROSMAP metadata. These
569 data are subject to controlled access in compliance with human privacy regulations. To
570 obtain the data, a data use agreement (DUA) must be completed. This requirement ensures
571 the anonymity of ROSMAP study participants. A DUA can be established with either the
572 Rush University Medical Center (RUMC) or SAGE, the organization that manages Synapse.
573 The necessary forms are available for download on their respective websites. All iPSC-related
574 data are accessible through links provided in our code repositories. For a complete list of data
575 availability and download links, please refer to the code repositories listed below. Additionally,
576 relevant processed datasets are available in the supplementary files of this manuscript.

577 **Code availability:** All code used in this study is available on GitHub ([https://github.com](https://github.com/djunamay/ABCA7l0f2)
578 /djunamay/ABCA7l0f2).

Main Figures

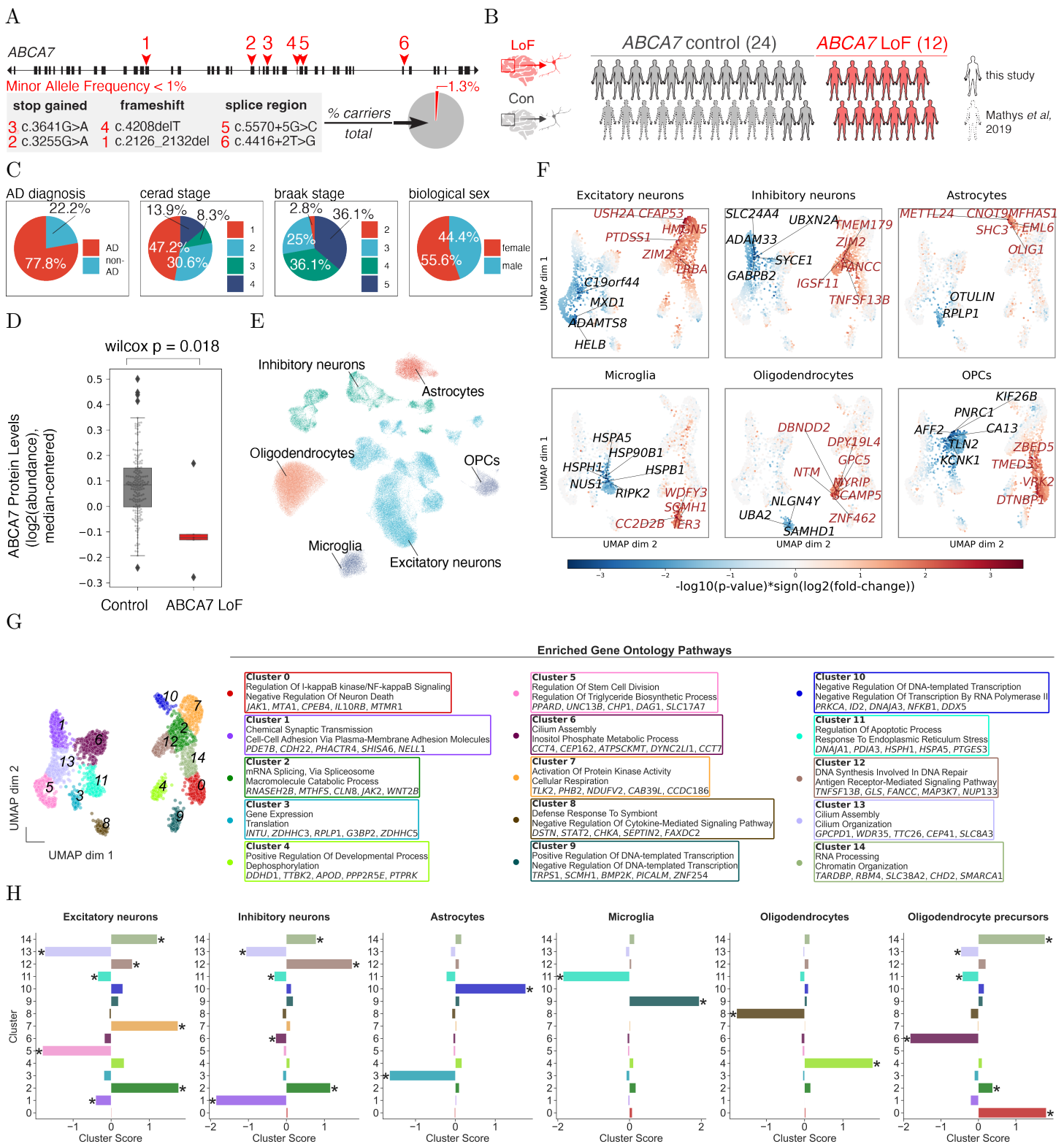


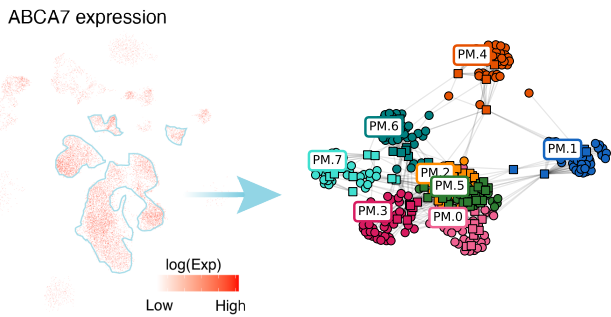
Figure 1: Single-nuclear RNA-sequencing Atlas of Human postmortem Prefrontal Cortex Reveals Cell Type-specific Gene Changes in ABCA7 LoF.

(A) ABCA7 gene structure indicating variant locations studied here (average minor allele frequency <1%). Exons are black rectangles; introns, black lines. Pie chart indicates frequency of ABCA7 PTC-variant

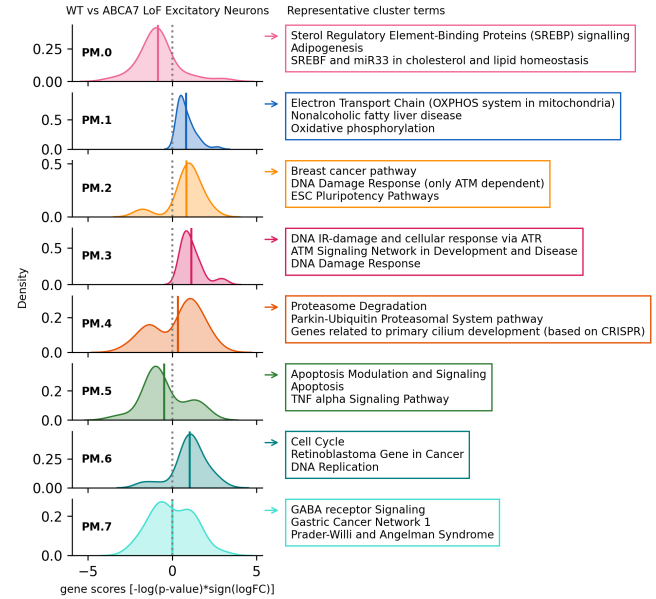
carriers in ROSMAP cohort.

- (B) Overview of human snRNA-seq cohort (created with BioRender.com).
- (C) Metadata summary of snRNA-seq cohort ($N = 36$ individuals).
- (D) ABCA7 protein abundance in postmortem prefrontal cortex from controls ($N = 180$) vs. ABCA7 LoF carriers ($N = 5$). Statistical comparison by Wilcoxon rank sum test. Boxes indicate quartiles; whiskers represent data within $1.5 \times$ interquartile range.
- (E) 2D UMAP projection of single-cell gene expression, colored by transcriptionally defined cell type.
- (F) 2D UMAP projection of ABCA7 LoF gene perturbation scores ($S = -\log_{10}(p) \times \text{sign}(\log_2(\text{FC}))$). Red: $S > 1.3$, Blue: $S < -1.3$; point size reflects $|S|$. Up to top 10 genes labeled.
- (G) 2D UMAP projection colored by gene cluster assignment (Gaussian mixture model; see Methods). Top pathway enrichments per cluster shown (GO BP, hypergeometric enrichment, $p < 0.01$).
- (H) Cell type-specific gene cluster scores ($SC = \text{mean}(S_i)$ for genes i in cluster c). * indicates permutation FDR-adjusted $p < 0.01$ and $|SC| > 0.25$.

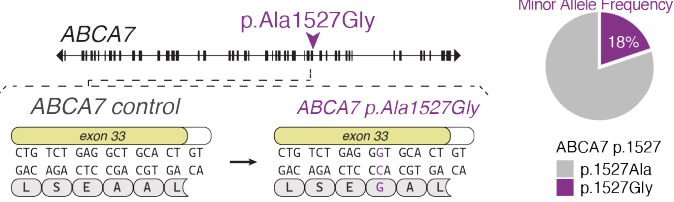
A



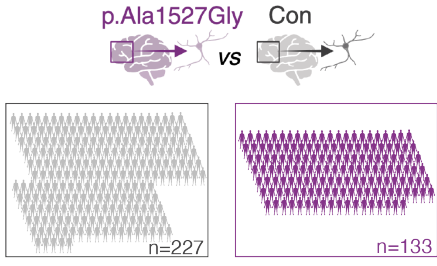
B



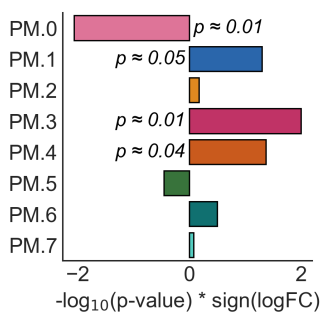
C



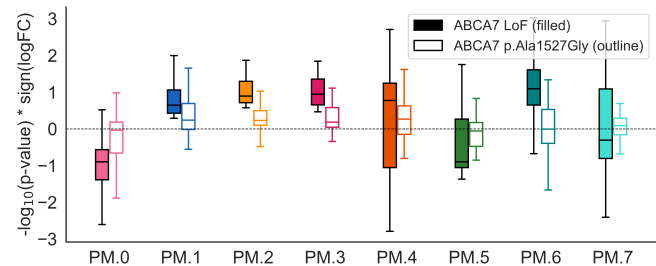
D



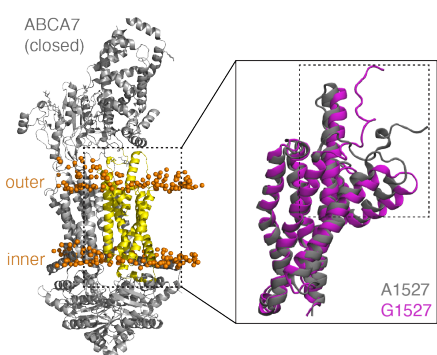
E



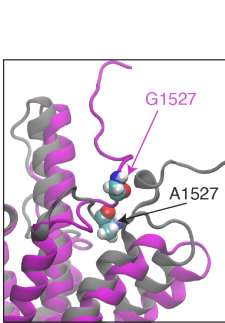
F



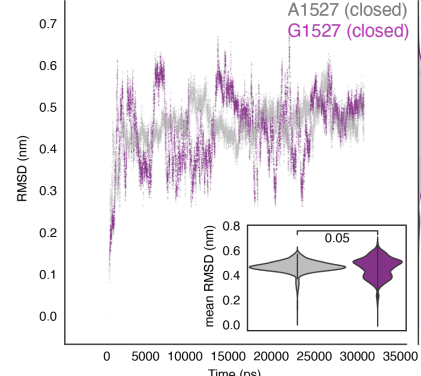
G



H



I



J

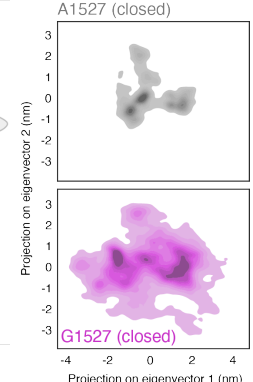


Figure 2: Transcriptional Perturbations in Excitatory Neurons in ABCA7 LoF and ABCA7 p.Ala1527Gly Variant Carriers.

- (A) (left) 2D UMAP projection of all cell types colored by log-transformed values of log-normalized ABCA7 expression (log(Exp)). (right) Kernighan-Lin (K/L) clustering of leading-edge genes from significantly perturbed pathways ($p < 0.05$) in ABCA7 LoF excitatory neurons. Colors indicate distinct K/L clusters (0–7).
- (B) Gaussian kernel density plots of gene perturbation scores ($S = -\log_{10}(p) \times \text{sign}(\log_2(\text{FC}))$) per K/L cluster. Positive S indicates upregulation in ABCA7 LoF. Solid lines show distribution means. Representative pathways with highest intra-cluster connectivity annotated per cluster.

- (C) Schematic of ABCA7 gene highlighting the p.Ala1527Gly codon change (purple arrow). Minor allele frequency (MAF) shown at right.
- (D) Overview of snRNA-seq cohort comparing ABCA7 p.Ala1527Gly carriers (homozygous/heterozygous) to non-carrier controls (MAF \approx 18%).
- (E) Perturbation (FGSEA scores) of ABCA7 LoF-associated gene clusters from (B) in excitatory neurons from p.Ala1527Gly carriers vs. controls. Top p -values ($p < 0.1$) indicated. Positive scores represent upregulation in carriers.
- (F) Distribution of gene perturbation scores (S) for each K/L cluster comparing ABCA7 p.Ala1527Gly (no fill) vs. LoF variants (solid fill). Positive S indicates upregulation.
- (G) Closed-conformation ABCA7 protein structure, highlighting domain (residues 1517–1756, yellow) used for molecular simulations. Lipid bilayer shown in orange. Expanded inset highlights Ala1527 (light grey) and Gly1527 (purple) residues.
- (H) Expanded inset from (G) with residues of interest indicated.
- (I) Root mean squared deviations (RMSD) of the closed-conformation ABCA7 domain (G) carrying Ala1527 (light grey) or Gly1527 (purple) during simulation, relative to reference closed conformation. Inset violin plot shows average C_α atom positional fluctuations.
- (J) Projection of C_α positional fluctuations onto the first two principal components during simulation for Ala1527 (top, light grey) and Gly1527 (bottom, purple).

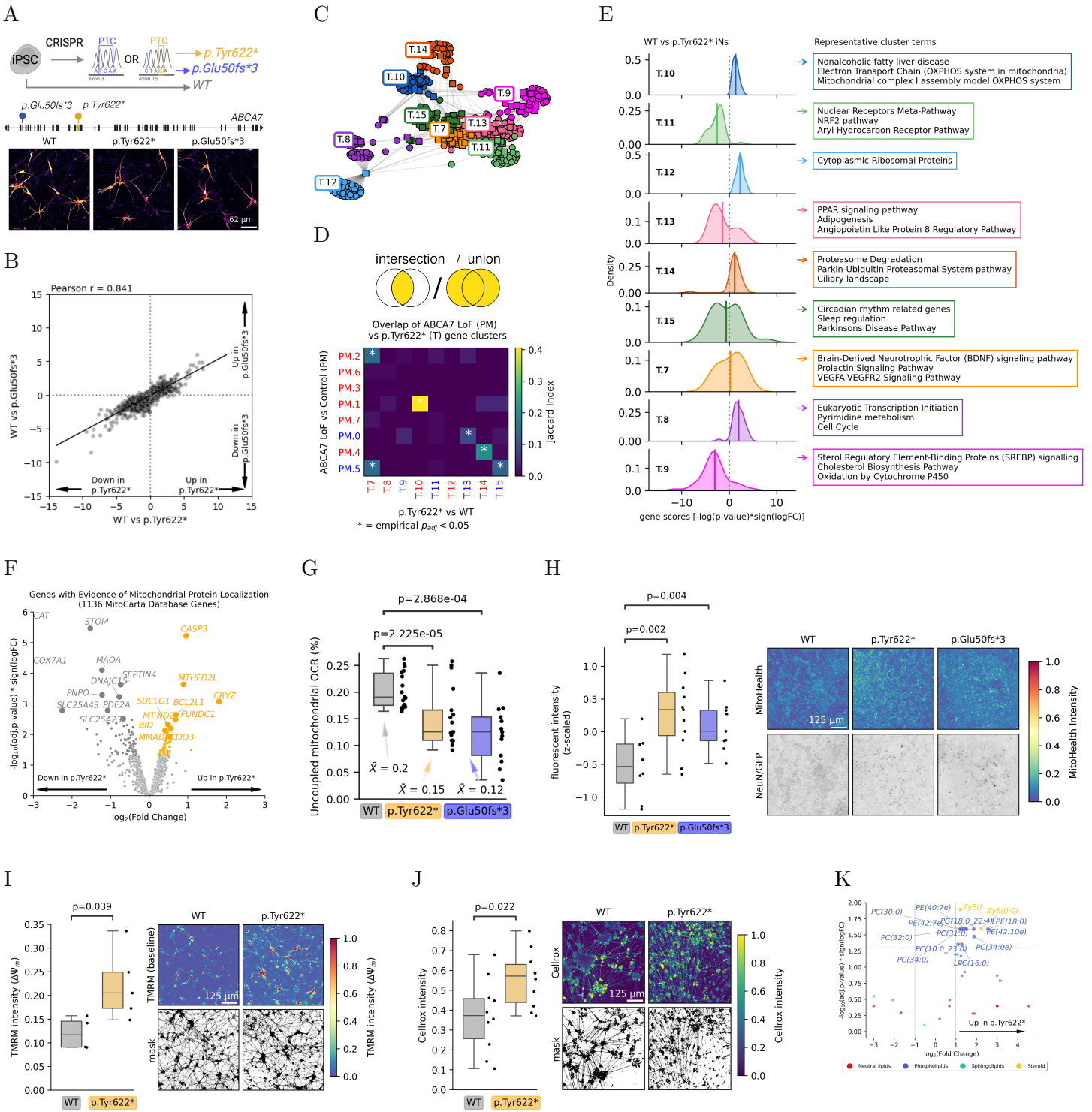


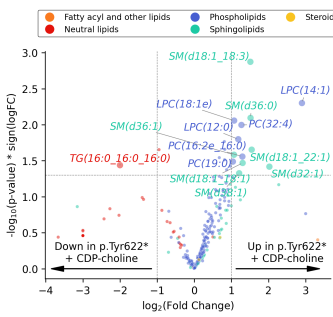
Figure 3: ABCA7 LoF Impacts Regulation of Mitochondrial Uncoupling in Neurons.

- (A) Schematic of iPSC-derived isogenic neuronal lines harboring ABCA7 loss-of-function (LoF) variants. Gene structure shows exons (black rectangles) and introns (black lines). CRISPR-Cas9 introduced premature termination codons in exon 3 (p.Glu50fs3, blue) or exon 15 (p.Tyr622*, orange). Confocal images show MAP2 staining in iNs differentiated for 4 weeks (genotypes indicated).
- (B) Correlation of gene perturbation scores ($S = -\log_{10}(p) \times \text{sign}(\log_2(\text{FC}))$) by bulk mRNAseq comparing p.Glu50fs3 vs. WT and p.Tyr622* vs. WT iNs cultured for 4 weeks.
- (C) Kernighan-Lin (K/L) clustering of leading-edge genes from significantly perturbed pathways (Ben-

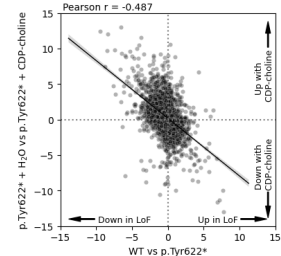
jamini–Hochberg (BH) FDR-adjusted $p < 0.05$) in p.Tyr622* vs. WT iNs. Colors represent distinct K/L clusters.

- (D) Heatmap of Jaccard index overlap between K/L gene clusters from p.Tyr622* neurons and clusters identified in human postmortem excitatory neurons. Red text denotes clusters with average score S upregulated in ABCA7 LoF; blue text denotes clusters with average S downregulated in ABCA7 LoF.
- (E) Gaussian kernel density plots of gene perturbation scores (S) within each cluster. Positive S indicates upregulation in p.Tyr622*. Solid lines denote cluster means. Top enriched pathways with highest intra-cluster connectivity indicated.
- (F) Volcano plot of differential expression of genes with mitochondrial-localized protein products (Mito-Carta) between p.Tyr622* and WT neurons.
- (G) Seahorse-measured mitochondrial uncoupled oxygen consumption rate (OCR) in WT and ABCA7 LoF and WT iNs cultured for 4 weeks. Each datapoint represents OCR from a single well. $N = 18$ (WT), 17 (p.Tyr622*), 13 (p.Glu50fs3) wells, across two differentiation batches. Statistical comparison by independent-sample t -test.
- (H) Mitochondrial membrane potential quantified via HCS MitoHealth dye fluorescence intensity in ABCA7 LoF iNs cultured for 4 weeks. Each datapoint represents average intensity per well (NeuN+ volumes averaged). Statistical comparison via linear mixed-effects model, accounting for well-of-origin random effects. $N = 8$ (WT), 11 (p.Tyr622*), 9 (p.Glu50fs3) wells; ≈ 3000 cells/condition, from three differentiation batches. Each NeuN/GFP image intensity was scaled relative to its maximum value, followed by gamma correction ($\gamma = 0.5$) for visualization.
- (I) Baseline mitochondrial membrane potential quantified by average TMRM fluorescence intensity per masked region (thresholded at 75th percentile) in ABCA7 LoF and WT iNs cultured for 4 weeks. Each datapoint represents average intensity per well. $N = 4$ (WT), 5 (p.Tyr622*) wells. Statistical comparison by independent-sample t -test.
- (J) Oxidative stress quantified by average CellROX fluorescence intensity per masked region (thresholded at 75th percentile) in p.Tyr622* and WT iNs cultured for 4 weeks. Each datapoint represents average intensity per well. $N = 10$ wells per genotype. Statistical comparison by independent-sample t -test.
- (K) Volcano plot of differentially abundant lipid species between p.Tyr622* and WT iNs cultured for 4 weeks, colored by lipid class. Statistical comparisons by independent-sample t -tests followed by BH FDR adjustment. $N = 10$ wells (WT) and 8 wells (p.Tyr622*).

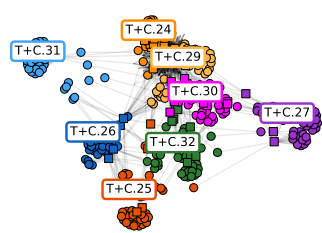
A



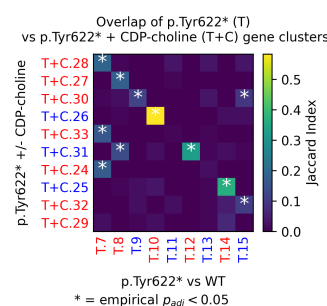
B



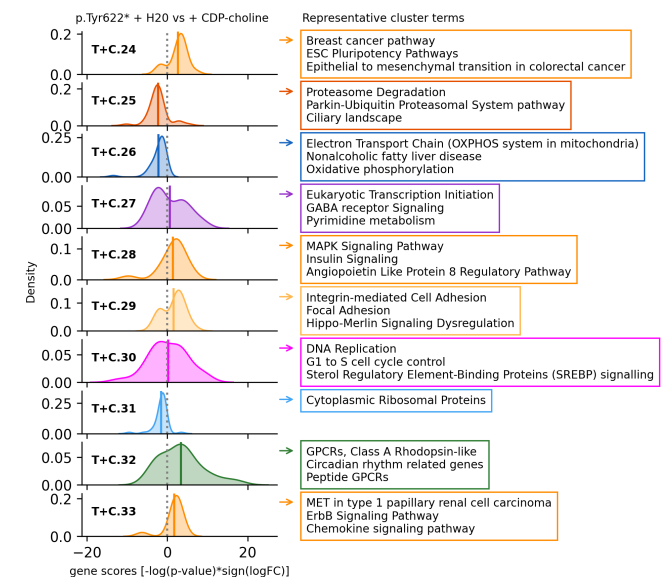
C



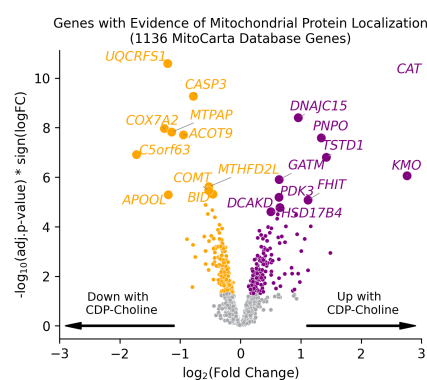
D



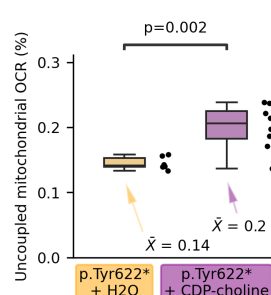
E



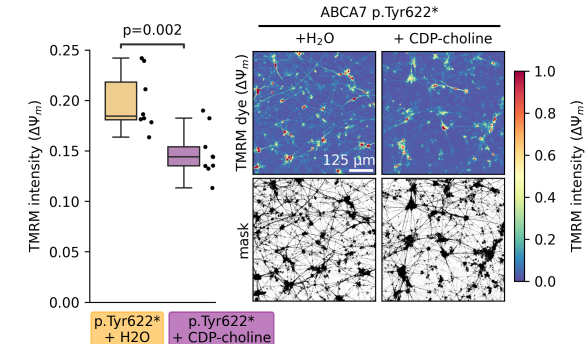
F



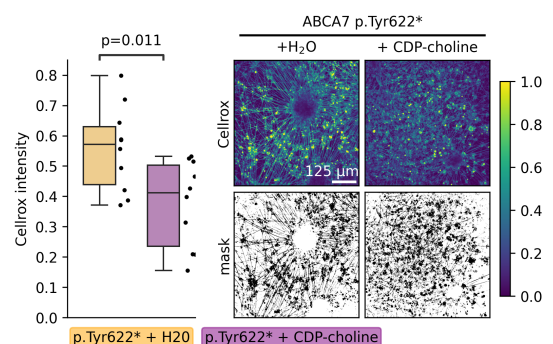
G



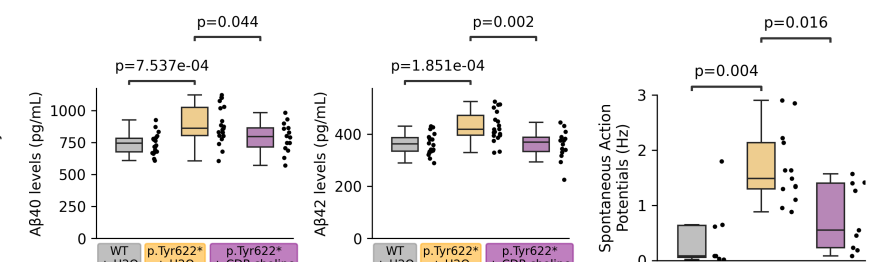
H



I



J



K

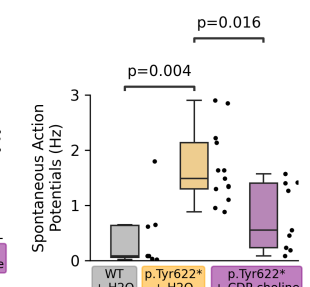


Figure 4: CDP-choline Treatment Rescues ABCA7 LoF-Induced Disruptions in Neurons.

- (A) Volcano plot of differentially abundant lipid species in p.Tyr622* iNs cultured for 4 weeks (treated with or without 100 μ M CDP-choline during the final 2 weeks), colored by lipid class. Statistical comparisons by independent-sample t -tests. $N = 5$ wells per genotype.
- (B) Correlation of gene perturbation scores ($S = -\log_{10}(p) \times \text{sign}(\log_2(\text{FC}))$) comparing p.Tyr622* vs WT and p.Tyr622* \pm CDP-choline iNs.
- (C) Kernighan-Lin (K/L) clustering of leading-edge genes from significantly perturbed pathways (BH FDR-adjusted $p < 0.05$) comparing p.Tyr622* \pm CDP-choline iNs. Colors represent distinct K/L

gene clusters, matched to p.Tyr622* vs. WT cluster colors based on Jaccard analysis in (D).

- (D) Heatmap of Jaccard index overlap between K/L clusters from p.Tyr622* vs. WT and p.Tyr622* \pm CDP-choline iNs.
- (E) (left) Gaussian kernel density plots of gene perturbation scores (S , positive values indicate upregulation with CDP-choline treatment) for each cluster. Solid lines denote cluster means. (right) Representative pathways annotating the most genes per cluster.
- (F) Volcano plot of differential expression of genes with mitochondrial-localized protein products (Mito-Carta) for p.Tyr622* \pm CDP-choline iNs.
- (G) Mitochondrial uncoupling quantified by Seahorse assay (proportion of basal oxygen consumption due to proton leak) in p.Tyr622* \pm CDP-choline iNs cultured for 4 weeks (treated with or without 100 μ M CDP-choline during the final 2 weeks). Each datapoint represents OCR from a single well. Statistical comparisons via independent-sample t -tests. $N = 6$ (vehicle), 8 (CDP-choline) wells.
- (H) Average TMRM fluorescence intensity per mask (thresholded at 75th percentile) in p.Tyr622* \pm CDP-choline iNs cultured for 4 weeks (treated with or without 100 μ M CDP-choline during the final 2 weeks), under baseline and FCCP-treated conditions. $N = 8$ wells in each condition.
- (I) Average CellROX fluorescence intensity per mask (thresholded at 75th percentile) in p.Tyr622* \pm CDP-choline iNs cultured for 4 weeks (treated with or without 100 μ M CDP-choline during the final 2 weeks). Each datapoint represents average intensity per well. $N = 10$ wells in each condition.
- (J) Quantification of secreted A β levels from media of cortical organoids derived from WT or p.Tyr622* iPSCs (cultured for 182 days), treated with or without 1 mM CDP-choline for 4 weeks. Each datapoint represents A β levels measured for a single cortical organoid. $N = 20$ (WT), 19 (p.Tyr622*), and 14 (p.Tyr622* + 1 mM CDP-choline) organoids.
- (K) Spontaneous action potentials recorded from dissociated cortical organoids derived from p.Tyr622* iPSCs (cultured for 150 days, followed by 2 weeks treatment post-dissociation), treated with or without 100 μ M CDP-choline. Each datapoint represents an individual cell. $N = 7$ (WT), 13 (p.Tyr622*), and 9 (p.Tyr622* + 100 μ M CDP-choline) cells.

Supplementary Materials for

ABCA7 Loss-of-Function Variants Impact Phosphatidylcholine Metabolism
in the Human Brain

579 **Materials and Methods**

580 Experimental Methods on human *postmortem* brain tissue

581 **Isolation of nuclei from frozen postmortem brain tissue.** For batch #1: The protocol
582 for the isolation of nuclei from frozen postmortem brain tissue (region BA10) was adapted
583 for smaller sample volumes from a previous study [50]. All procedures were carried out on
584 ice or at 4°C. In brief, postmortem brain tissue was homogenized in 700 µl Homogenization
585 Buffer (320 mM sucrose, 5 mM CaCl₂, 3 mM Mg(CH₃COO)₂, 10 mM Tris HCl pH 7.8,
586 0.1 mM EDTA pH 8.0, 0.1% IGEPAL CA-630, 1 mM β-mercaptoethanol, and 0.4 U µl-1
587 recombinant RNase inhibitor (Clontech)) using a Wheaton Dounce tissue grinder (15 strokes
588 with the loose pestle). Homogenized tissue was filtered through a 40-µm cell strainer, mixed
589 with an equal volume of Working Solution, which is prepared by mixing Diluent (30mM
590 CaCl₂, 18mM Mg(CH₃COO)₂, 60mM Tris pH 7.8, 0.6mM EDTA, 6mM β-mercaptoethanol)
591 with Optiprep density gradient solution (Sigma-Aldrich D1556-250ML) in a 1:5 ratio. The
592 sample mix was then loaded on top of an Optiprep density gradient consisting of 750 µl 30%
593 OptiPrep solution (1.5:1 ratio of Working Solution:Homogenization Buffer) on top of 300 µl
594 40% OptiPrep solution (4:1 ratio of Working Solution:Homogenization Buffer). The nuclei
595 were separated by centrifugation (5 min, 10,000 g, 4 °C). Approximately 100µl of nuclei
596 were collected from the 30%/40% interface and washed twice with 1 ml of PBS containing
597 0.04% BSA, centrifuging 300g for 3 min (4 °C) in between, then resuspended in 100µl PBS
598 containing 0.04% BSA. The nuclei were counted on C-Chip disposable hemocytometer and
599 diluted to 1000 nuclei per µl in PBS containing 0.04% BSA.

600 For batch #2: These samples (fresh postmortem brain; PFC BA10) were prepared as part of
601 and according to a previous study [50].

602 Informed consent and Anatomical Gift Act consent were obtained from each participant.
603 The Religious Orders Study and Rush Memory and Aging Project were approved by the
604 Institutional Review Board (IRB) of Rush University Medical Center. All participants signed
605 a repository consent, allowing their data and biospecimens to be shared.

606 **Droplet-based snRNA-seq.** For batch #1: cDNA libraries were generated using
607 the Chromium Single Cell 3 Reagent Kits v3 following the manufacturer's protocol (10x
608 Genomics). Libraries were sequenced on the NovaSeq 6000 S2 platform (paired-end, 28 + 91
609 bp, with an 8-nucleotide index). Samples were distributed across two lanes and sequenced
610 twice on separate flow cells to enhance sequencing depth.

612 For batch #2: Libraries were prepared using Chromium Single Cell 3 Reagent Kits
613 v2 and sequenced with the NextSeq 500/550 High Output v2 kits (150 cycles), as described
614 in our previously published study [50].

615

616 Raw sequencing reads from all samples were processed jointly for alignment and gene counting.

617

618 Culture and generation of human isogenic iPSCs

619 A control parental line was derived from a 75-year-old female (AG09173) with an APOE3/3
620 genotype by the Picower Institute for Learning and Memory iPSC Facility as first described
621 [113]. Two ABCA7 LoF isogenic lines were derived from parental AG09173. ABCA7
622 p.Glu50fs*3, generated by Synthego (www.synthego.com), contains a premature termination
623 codon in exon 3 (Figure ??1A), which to our knowledge has not been discovered in patients,
624 but is functionally analogous to patient loss-of-function mutations.

625 ABCA7 p.Tyr622* contains a patient-derived mutation (Y622*) [114] and was gen-
626 erated in house by CRISPR-Cas9 genome editing. The CRISPR/Cas9-ABCA7-
627 Y622* sgRNA plasmid was prepared followed by the published protocol [115].
628 In brief, a sgRNA sequence within 10 nucleotides from the target site was de-
629 signed using the CRISPR/Cas9 Design Tool (<http://crispr.mit.edu>). The oligomer
630 pairs (forward: 5'-CACCGCCCCTACAGCCACCCGGGCG-3' and reverse: 5'-
631 AAACCGCCCAGGGTGGCTGTAGGGGC-3') were annealed and cloned into pSpCas9-
632 2A-GFP (PX458) plasmid (Addgene #48138). Plasmid DNA was submitted for Sanger
633 sequencing to confirm correct ABCA7 sgRNA sequence (Figure ??1B).

634 AG09173 iPSCs were dissociated with Accutase (Thermo Fisher Scientific) supplemented
635 with 10 M ROCK inhibitor (Tocris) for electroporation using Amaxa and Human Stem
636 Cell Nucleofector Kit I (Lonza). 5x10⁶ cells were resuspended in 100 l of reaction buffer
637 supplemented with 7.5 g of CRISPR/Cas9-ABCA7 sgRNA plasmid and 15 g of single-strand
638 oligodeoxynucleotide (ssODN) template (5'-GGTGCAGCCCCCAGGCCAATCCAGGA
639 GCTGCACCCCTAACGCTCCGTTGCCTCTCACAGCTGGAGACATCCTCCCTAG
640 AGCCACCCGGCGTCGTCTCCTGTTGGCAGCCTCGCGGTGGCCACGGT
641 GACCCAGAGCTTCCTGCTCAGCGCCTCTTCTCCCGCGCCAACCTGG-3'). This
642 reaction mixture was nucleofected with program A-23, resuspended with media supplemented
643 with 10 M ROCK inhibitor and seeded on MEF plates. Two days after electroporation,
644 cells were dissociated and filtered through Falcon polystyrene test tubes (Corning #352235),
645 transferred to Falcon polypropylene test tubes (Corning #352063) and sorted by BD FACS

646 Aria IIU in FACS Facility at the Whitehead Institute and seeded as single cells in media
647 supplemented with 1X Penicillin-Streptomycin (P/S, Gemini Bio-products) and 10 M ROCK
648 inhibitor. After sufficient colony growth, each colony was transferred in part to a 12-well
649 plate while the remainder was collected and used to extract genomic DNA (Qiagen DNeasy
650 Blood Tissue Kit, Cat. No. 69504) and screen for the Y622* mutation by sanger sequencing.

651 All lines used were confirmed to have normal karyotypes before use and periodically reviewed
652 (Cell Line Genetics) (Figure ??0C). All human iPSCs were maintained at 37°C and 5%
653 CO₂, in feeder-free conditions in mTeSR-1 medium (Cat #85850; STEMCELL Technologies)
654 on Matrigel-coated plates (Cat # 354277; Corning; hESC-Qualified Matrix). iPSCs were
655 passaged at 60–80% confluence using ReLeSR (Cat# 05872; STEMCELL Technologies) and
656 reseeded between 1:6 and 1:24 (depending on desired density) onto Matrigel-coated plates.

657 **Experimental Methods on iNs**

658 **rTTA and NGN2 Virus production.** HEK293T cells (ATCC, Cat#CRL-3216) were
659 maintained in DMEM/F-12, GlutaMAX (ThermoFisher, Cat#10565018), 10% fetal bovine
660 serum (GeminiBio, SKU#100-106), 1% MEM Non-essential amino acids (Sigma, Cat#M7145),
661 1% sodium pyruvate (ThermoFisher, Cat#11360070), and 1% Penicillin-Streptomycin (Gemi-
662 niBio, SKU#400-109). Cells were passaged for maintenance with TrypLE (ThermoFisher,
663 Cat#12605010) at 70-80% confluence and reseeded 1:10 in 10 cm tissue culture plates.

664 For transfection, HEK293T cells were seeded at 5x10⁶ cells per 10 cm plate. Transfection
665 mixtures containing the components required for 3rd generation lentiviral production (per
666 10 cm dish: 10 µg EF1a-rtTA-Hygro (Addgene #66810) or pLV-TetO-hNGN2-eGFP-Puro
667 (Addgene #79823), 5 µg pMDL g/pRRE, 2.5 µg pRSV-Rev, 2.5 µg MD2.G, and 48 µL
668 polyethyleneimine (1 mg/mL) in 600 uL OptiMEM (Fisher, Cat#51-985-034)). Mixtures
669 were inverted 10X and incubated at RT for 20 min, then added dropwise to the dish.
670 Transfection media was removed 16h later and replaced with 10 mL fresh media. Three days
671 after transfection, media was collected and centrifuged at 3000 xg for 5 min at 4°C to pellet
672 any contaminating cells. Supernatant was transferred to sterile Millex glass ultracentrifuge
673 tubes and centrifuged at 25,000 rpm for 2 hours using a SW32Ti rotor in a Beckman Optima
674 L-90K Ultracentrifuge. The pellets were resuspended in 1 mL PBS per 10 cm plate, and
675 stored at -80°C until use.

676 **Lentivirus-mediated NGN2 induction in iPSCs and drug treatments.** iPSCs
677 were dissociated into single cell suspension with Cell Dissociation Buffer (Life Technologies,
678 Cat#13151-014), centrifuged at 300 xg for 5 min, and resuspended in mTeSR1 media with

679 Rock inhibitor (Rockout; Abcam, ab285418). Single-cell suspension was plated in a 6-well
680 plate coated with Matrigel for an optimized seeding density of 50-60% confluence 24 hours
681 after plating. One day after plating, cells were co-transduced with 80 μ L pLV-TetO-hNGN2-
682 eGFP-Puro and 80 μ L EF1a-rtTA-Hygro added in 1 mL fresh media per well and incubated
683 overnight at 37°C. NGN2 expression was then induced 24 hours later with addition of 2
684 mL fresh media supplemented with doxycycline (DOX, 1 μ g/mL, final concentration) and
685 Rock inhibitor. Puromycin (1 μ g/mL) selection of non-NGN2 expressing cells was performed
686 with media change 24 hours after induction, with continued DOX supplementation. After 24
687 hours of puromycin selection, immature neurons were re-plated onto PDL/laminin coated
688 plates at 1x106 cells/well on 6-well plates or 5x104 cells/well on 96-well plates. Neurons
689 were maintained in BrainPhys Neuronal Media (STEMCELL Technologies, Cat#05793)
690 with Neurocult SM1 Neuronal Supplement (STEMCELL Technologies, Cat#05711), N2-
691 supplement-A (STEMCELL Technologies, Cat#07152), laminin (1ug/mL), and DOX (1
692 μ g/mL) with half media changes every 3-4 days. Neuronal cultures were maintained for 28
693 days before experimentation.

694 iPSC-derived neurons were treated with cytidine 5'-diphosphocholine (CDP-choline; Millipore
695 Sigma 30290) to final concentrations of 100 μ M beginning at day 14 and repeated with each
696 media change until 28 days matured. Choice of treatment concentration and duration was
697 based on a previous study by our lab [74].

698 **Electrophysiological recordings.** Cells were placed in a recording chamber and perfused
699 with oxygenated artificial cerebrospinal fluid (ACSF) contains (in mM) 125 NaCl, 2.5 KCl,
700 1.2 NaH₂PO₄ • H₂O, 2.4 CaCl₂ • 2H₂O, 1.2 MgCl₂ • 6H₂O, 26 NaHCO₃ and 11 D-Glucose
701 at a constant rate of 2 mL/min at 32°C. Cells were visualized using infrared differential
702 interference contrast (IR-DIC) imaging on an Olympus BX-50WI microscope.

703 Recordings were performed using Axon Multiclamp 700B and Clampex 11.2 (Molecular
704 Devices). Action potentials were generated by injecting various steps of currents using current
705 clamp configuration. Whole-cell currents were recorded from a holding potential of -80 mV
706 by stepping to various voltages using voltage clamp configuration. Cell-attached recording
707 configuration was used to measure spontaneous firing activity. Signals were filtered at 1 kHz
708 using the amplifier's four-pole, low-pass Bessel filter, digitized at 10 kHz with a Digidata
709 1550B interface (Molecular Devices). Pipette solution contained (in mM) 120 K gluconate, 5
710 KCl, 2 MgCl₂ • 6H₂O, 10 HEPES, 4 ATP, 0.2 GTP. pClamp 11.2 (Molecular Devices) and
711 GraphPad Prism 10 software suites were used for data acquisition and analysis. Data are
712 presented as means \pm standard errors of means (SEM).

⁷¹³ **A β Enzyme linked immunosorbent assays on iNs.** Media was collected from 4 week
⁷¹⁴ old iNs and flash frozen. ELISAs were performed on thawed media according to manufacturer's
⁷¹⁵ instructions to measure A40 (ThermoFisher Scientific, KHB3481) and A42 (ThermoFisher
⁷¹⁶ Scientific, KHB3441) respectively.

⁷¹⁷ **Mitochondrial Health cell stain.** HCS Mitochondrial Health kit (ThermoFisher,
⁷¹⁸ Cat#H10295) were used on live cells according to manufacturer's protocols. In brief, 50 μ L
⁷¹⁹ of media containing 1.5 μ L MitoHealth dye was added to each well and incubated on live
⁷²⁰ cells for 30 min at 37°C. Next, neurons were fixed in 4% paraformaldehyde/4% sucrose in
⁷²¹ PBS at 4°C for 15 min at room temperature, washed 3X with PBS, then permeabilized with
⁷²² 0.1% Triton-X in PBS for 5 min at room temperature. Cells were blocked in 2% Bovine
⁷²³ Serum Albumin (BSA, Fisher Bioreagents, BP9703) in PBS for 20 min at room temperature,
⁷²⁴ then incubated in primary antibodies diluted in blocking solution (NeuN; 1:500) overnight
⁷²⁵ at 4°C. Cells were washed 3X for 5 min with PBS, then incubated in secondary antibodies
⁷²⁶ diluted in blocking solution (1:1000) for 2 hours at room temperature. Cells were washed
⁷²⁷ 3X for 5 min with PBS, then incubated for 10 min with 1:2000 Hoechst 33342 (Invitrogen,
⁷²⁸ H3570). Cells were washed 1X with PBS, and wells flooded with PBS for imaging.
⁷²⁹ Confocal images were acquired on a Zeiss LSM900. Acquisition settings were kept constant
⁷³⁰ within each imaging batch (where conditions of interest were uniformly distributed across
⁷³¹ plates). The minimum and maximum z-plane was manually determined for each culture well,
⁷³² to accommodate differences in culture thickness. Cultures were imaged at 1 μ m intervals
⁷³³ along the z-axis.

⁷³⁴ **Live imaging of TMRM.** Stock solutions were initially prepared at concentrations of 10
⁷³⁵ μ M TMRM (ThermoFisher, I34361), 100 μ M FCCP (Cayman Chemical, 15218), and 100 μ M
⁷³⁶ oligomycin from Streptomyces diastatochromogenes (Sigma, O4876-25MG), achieving final
⁷³⁷ working concentrations of 0.1 μ M TMRM, 1 μ M FCCP, and 1 μ M oligomycin. For imaging,
⁷³⁸ 3 μ L of the 10 μ M TMRM stock solution was added to each well of iNs cultured in 300 μ L
⁷³⁹ of media on a 96-well plate. Cells were incubated with TMRM dye for 30 minutes at 37°C.
⁷⁴⁰ Live-cell imaging was then performed using a Zeiss LSM 900 confocal microscope equipped
⁷⁴¹ with ZEN software. After initial TMRM images were acquired, 3 μ L of the 100 μ M FCCP
⁷⁴² stock was added to each well, and images were captured immediately. Subsequently, 3 μ L of
⁷⁴³ the 100 μ M oligomycin stock was added, followed by immediate image acquisition. Confocal
⁷⁴⁴ images were acquired as single optical sections (single-plane imaging) on a Zeiss LSM900
⁷⁴⁵ microscope.

⁷⁴⁶ **Live imaging of CellROX.** iNs were maintained in 300 μ L of media per well in a 96-well
⁷⁴⁷ plate. A stock solution of CellROX Orange Reagent (ThermoFisher, C10443) was prepared
⁷⁴⁸ at a concentration of 500 μ M. For staining, 3 μ L of the 500 μ M CellROX dye was added
⁷⁴⁹ directly to each well containing iNs in 300 μ L media. Cells were incubated with the dye for
⁷⁵⁰ 30 minutes at 37°C. After incubation, live-cell images were acquired as single optical sections
⁷⁵¹ (single-plane imaging) on a Zeiss LSM900 microscope.

⁷⁵² **Seahorse Metabolic Assays.** iPSCs were differentiated as described above directly on
⁷⁵³ 96-well Agilent Seahorse XFe96/XF Pro cell culture microplates and matured for 28 days
⁷⁵⁴ before assaying on a Seahorse XFe96 Analyzer. Seahorse XF Cell Mito Stress Test and
⁷⁵⁵ Oxidation Stress Tests were performed according to manufacturer protocol with the following
⁷⁵⁶ final drug concentration: Oligomycin, 2.5 μ M; FCCP, 1 μ M; Rotenone/Antimycin, 0.5 μ M.

⁷⁵⁷ **MAP2 and NeuN staining of iNs.** iNs were plated on coverslips with coating. Cells were
⁷⁵⁸ fixed in 4% formaldehyde for 10min at room temperature followed by PBS wash once. Cells
⁷⁵⁹ were next permeabilized and blocked in PBS containing 0.2% TritonX-100 and 10% bovine
⁷⁶⁰ serum albumin for 1 hour at room temperature, then incubated with primary antibody (MAP2
⁷⁶¹ 1:1000; NeuN 1:1000; diluted in blocking solution) at 4 °C overnight. Primary antibody
⁷⁶² was visualized using the appropriate secondary antibody conjugated to Alexa Fluor 594,
⁷⁶³ or Alexa Fluor 647 (1:500, Thermo Fisher Scientific). Nuclei were visualized with Hoechst
⁷⁶⁴ 33342 (1:1000, Thermo Fisher Scientific). Coverslips were then mounted on the glass slides
⁷⁶⁵ with fluoromount g. Confocal images were acquired as single optical sections (single-plane
⁷⁶⁶ imaging) on a Zeiss LSM900 microscope.

⁷⁶⁷ **RNA Extraction, Library Preparation, and Sequencing.** Total RNA was extracted
⁷⁶⁸ from iNs using the RNeasy Mini Kit (Qiagen), and RNA quality was assessed using a 5300
⁷⁶⁹ Fragment Analyzer (Agilent). Only samples with an RNA Quality Number (RQN) greater
⁷⁷⁰ than 9.5 were selected for library preparation. Full-length cDNA was synthesized using the
⁷⁷¹ SMART-seq v4 kit (Takara Bio), and sequencing-ready libraries were subsequently prepared
⁷⁷² using the Nextera XT DNA Library Preparation Kit (Illumina). Libraries were sequenced
⁷⁷³ as 75 bp + 75 bp paired-end reads with dual 8-nucleotide indexes on an Element AVITI
⁷⁷⁴ sequencing platform (Element Biosciences) at the MIT BioMicro Center.

⁷⁷⁵ **LC-MS Experiments on iNs**

⁷⁷⁶ **Biphasic Extraction.** iPSC-derived neurons were washed once with cold PBS (Fisher;
⁷⁷⁷ Cat#MT21040CM) and lifted off plate with a cell scraper in 1 mL cold PBS. Cells were

778 centrifuged at 2000 $\times g$ for 5 min. PBS was removed, and cells were resuspended in 2 mL
779 cold methanol for biphasic extraction. Chloroform (Sigma 1.02444) (4 mL; cold) was added
780 to each vial, and mixed by vortexing for 1 min. Water (Sigma WX0001) (2 mL; cold) was
781 added to each vial, and mixed by vortexing for 1 min. Vials were placed in 50 mL conical
782 tubes and centrifuged for 10 min at 3000 rcf for phase separation. The lower, chloroform
783 phase was collected (3 mL from each sample) and transferred to new vials. In instances
784 where samples were prepared by the Harvard Center for Mass Spectrometry, cell pellets were
785 provided in 500 μ L of methanol, vortexed, and transferred to 8 mL glass vials. Each sample
786 received an additional 1.5 mL of methanol and 4 mL of chloroform, followed by vortexing and
787 incubation for 10 min in an ultrasound bath. Next, 2 mL of water was added, and samples
788 were again vortexed. Phase separation was achieved by centrifugation at 800 rcf for 10 min
789 at 4°C. The resulting upper aqueous phases were transferred into new glass vials designated
790 for metabolomics analysis, while the lower chloroform phases were transferred separately for
791 lipidomics analysis. At least one blank sample (containing no cells) was prepared alongside
792 each biphasic extraction experiment and processed identically through the LC-MS analysis
793 pipeline.

794 **Cell pellet sample preparation for LC-MS Lipidomics.** Subsequent sample prepara-
795 tion for lipidomics was performed by the Harvard Center for Mass Spectrometry. Samples
796 were dried under nitrogen flow until approximately 1 mL remained, transferred into micro-
797 centrifuge tubes, and completely evaporated to dryness. Dried samples were resuspended
798 in chloroform, with volumes scaled according to biomass (cell count) using a minimum of
799 60 μ L, then split into two equal aliquots for positive and negative ionization mode analyses.
800 For experiments using only positive ionization mode, samples were resuspended in a smaller
801 biomass-scaled volume (minimum 20–25 μ L) without splitting. Following resuspension, sam-
802 ples were centrifuged (maximum speed for 10 min or 18,000 rcf for 20 min at 4°C), and
803 supernatants were transferred into microinserts for LC-MS analysis.

804 **Cell pellet sample preparation for LC-MS Metabolomics.** Subsequent sample
805 preparation for metabolomics was performed by the Harvard Center for Mass Spectrometry.
806 Samples were dried under nitrogen flow until approximately 1 mL remained, transferred into
807 microcentrifuge tubes, and evaporated completely to dryness. Dried samples were resuspended
808 in 50% acetonitrile in water, using volumes scaled according to provided biomass (minimum
809 20 μ L). Following centrifugation at maximum speed for 10 min, a consistent volume (either
810 12 μ L or 15 μ L, depending on the batch) of supernatant from each sample was transferred
811 into microinserts. The remaining supernatants from each batch were pooled separately to

812 create batch-specific quality control (QC) samples.

813 **Media preparation for LC-MS Metabolomics.** Media samples (100 μ L each) were
814 transferred into microcentrifuge tubes containing 1 mL of methanol and incubated at -20°C
815 for 2 hours. Following incubation, samples were centrifuged at 18,000 rcf for 20 min at -9°C,
816 and supernatants were transferred into new tubes and evaporated to dryness under nitrogen
817 flow. The dried samples were resuspended in 50 μ L of 30% acetonitrile in water containing
818 2 mM medronic acid, centrifuged again at 18,000 rcf for 20 min at 4°C, and the resulting
819 supernatants were transferred into glass microinserts for LC-MS analysis.

820 **LC-MS Lipidomics.** LC-MS lipidomics analyses were conducted at the Harvard Center
821 for Mass Spectrometry using a procedure adapted from [116]. Samples were analyzed using
822 an Orbitrap Exactive Plus mass spectrometer (Thermo Scientific) coupled to an Ultimate
823 3000 LC system (Thermo Scientific). Analyses were performed in both positive and negative
824 ionization modes, in top 5 automatic data-dependent MS/MS mode. Chromatographic
825 separation was performed on a Biobond C4 column (4.6 \times 50 mm, 5 μ m particle size; Dikma
826 Technologies). The flow rate began at 100 μ L min $^{-1}$ with 0% mobile phase B (MB) for the
827 initial 5 minutes, followed by an increase to 400 μ L min $^{-1}$ over the next 50 minutes with a
828 linear gradient of MB from 20% to 100%. The column was subsequently washed at 500 μ L
829 min $^{-1}$ for 8 minutes with 100% MB, then re-equilibrated for 7 minutes at 500 μ L min $^{-1}$ using
830 0% MB. For positive ion mode, mobile phases consisted of buffer A (MA: 5 mM ammonium
831 formate, 0.1% formic acid, and 5% methanol in water) and buffer B (MB: 5 mM ammonium
832 formate, 0.1% formic acid, 5% water, and 35% methanol in isopropanol). For negative ion
833 mode, buffer A (MA) contained 0.03% ammonium hydroxide and 5% methanol in water,
834 and buffer B (MB) contained 0.03% ammonium hydroxide, 5% water, and 35% methanol in
835 isopropanol. Lipids were identified, and their signals integrated using Lipidsearch software
836 (version 4.2.27, Mitsui Knowledge Industry, University of Tokyo). Integration quality and
837 peak selections were manually curated prior to data export.

838 **LC-MS Metabolomics.** LC-MS metabolomics analyses were performed at the Harvard
839 Center for Mass Spectrometry using a Vanquish LC system coupled with an ID-X mass
840 spectrometer (Thermo Fisher Scientific). Samples (5 μ L injection) were analyzed on a
841 ZIC-pHILIC peek-coated column (150 mm \times 2.1 mm, 5 μ m particle size; Sigma Aldrich)
842 held at 40°C. Mobile phases comprised buffer A (20 mM ammonium carbonate and 0.1%
843 ammonium hydroxide in water) and buffer B (97% acetonitrile in water). The gradient
844 initiated at 93% B, decreasing linearly to 40% B over 19 minutes, further decreasing to 0%

845 B over the subsequent 9 minutes, held at 0% B for 5 minutes, returned to 93% B within 3
846 minutes, and finally re-equilibrated at 93% B for 9 minutes. The flow rate was held constant
847 at 0.15 mL min^{-1} , except for an initial 30-second ramp from 0.05 to 0.15 mL min^{-1} . Mass
848 spectrometry data were acquired in polarity-switching mode at 120,000 resolution, with an
849 AGC target of 1×10^5 , covering an m/z range from 65 to 1000. MS1 acquisition employed
850 polarity switching for all samples. MS2 and MS3 analyses were performed on pooled samples
851 using the AcquireX DeepScan method, with five reinjections each in positive and negative
852 ion modes separately. A mixture containing standards of targeted metabolites was prepared
853 and analyzed immediately following the sample runs for targeted metabolite analysis.

854 **Experimental Methods on Dorsal Cortical Organoids**

855 **Cortical organoid generation** Dorsal cortical organoid were generated as previously
856 described [117]. In brief, iPSC were cultured until 80-90% confluence, before dissociation
857 and preparing a single cell suspension at 1×10^5 cells/mL in mTesr supplemented with 10
858 M Rock inhibitor. cortical organoids were then generated by distributing in 100uL / well
859 in PrimeSurface® 96 Slit-well Plates (S-Bio, MS9096SZ). After 48-72 hours, differentiation
860 was induced on days 0 - 5 via daily media change in Neural Induction Media comprised
861 of DMEMf/12 (Life Technologies, cat. no. 11330-032), KnockOut serum replacement
862 (Life Technologies, 10828-028), GlutaMAX, 2-Mercaptoethanol, Penicillin-Streptomycin, and
863 SMAD inhibitors SB-431542 and dorsomorphin. From days 6-16, media was switched to Neural
864 Differentiation medium composed of Neurobasal A medium, B27 supplement, GlutaMAX,
865 Penicillin-streptomycin, Human recombinant EGF (20 ng/ml), Human recombinant FGF2
866 (20 ng/ml). Daily media change was performed until day 16, followed by every other day
867 until day 25. From day 25 onwards, EGF and FGF was removed and replaced with 20ng/mL
868 Human recombinant brain-derived neurotrophic factor (BDNF; 450-02) and 20 ng/mL Human
869 recombinant neurotrophin 3 (NT3; PeproTech, cat. no. 450-03). After day 45, media was
870 changed two times per week.

871 **A Enzyme linked immunosorbent assays on cortical organoids.** Culture media was
872 collected from cortical organoids at days 176-182, following 3-4 week treatments with $500 \mu\text{M}$
873 or 1 mM CDP-choline. Samples were kept on ice and immediately analyzed using ELISA to
874 quantify levels of A β 40 and A β 42. ELISAs were performed according to the manufacturer's
875 protocols for A β 40 (ThermoFisher Scientific, KHB3481) and A β 42 (ThermoFisher Scientific,
876 KHB3441). For the A β 42 assay, 50 μL of undiluted media was used, whereas media samples
877 were diluted (1:6.67 or 1:10) for the A β 40 assay. The cortical organoid age (5-6 months) was
878 selected based on empirical evidence showing the emergence of a robust amyloid phenotype

879 at this developmental stage. CDP-choline concentrations were increased from 100 μ M to 500
880 μ M and 1 mM to compensate for reduced perfusion in cortical organoids compared to 2D iN
881 cultures.

882 **Electrophysiological recordings on cortical organoids** To produce 2D cultures from
883 cortical organoids, day 150 cortical organoids were washed in PBS, before transferring to
884 1.5 mL eppendorf tubes containing Accutase (Stem Cell Technologies, 07920) and placing
885 in a 37C water bath for 40 minutes, with gentle agitation using a P1000 pipette every 5-10
886 minutes. Dissociated organoids were then plated on #1 glass coverslips (Fisher Scientific,
887 50-194-4702) with PDL, laminin, and matrigel coating as previously described. 2D cultures
888 were maintained with or without 100 μ M CDP-choline treatment for two weeks before
889 electrophysiological recordings. Electrophysiological recordings were performed as described
890 for the iNs. This treatment duration and concentration were selected to align with conditions
891 in 2D iNs experiments. The cortical organoid age was chosen based on empirical observations
892 indicating the emergence of a robust amyloid phenotype at the developmental stage of 5-6
893 months.

894 Outliers in spontaneous action potentials were detected using the interquartile range (IQR)
895 method. Specifically, data points falling below $Q1 - 2 \times IQR$ or above $Q3 + 2 \times IQR$ were
896 identified as outliers. This method resulted in the removal of two data points exhibiting
897 unusually high spontaneous action potentials: one in condition p.Tyr622* (value = 9.38)
898 and one in condition p.Tyr622*+Choline (value = 6.15). Additionally, cells recording zero
899 spontaneous potentials were excluded, as these were presumed to represent glial cells rather
900 than neuronal cells.

901 **Immunostaining of cortical organoids.** 20 μ m cortical organoid sections were fixed in
902 4% formaldehyde for 10min at room temperature, and cortical organoids were then transferred
903 to 30% sucrose/PBS for dehydration at 4C for 2 to 3 days. cortical organoids were next
904 embedded in optimal cutting temperature compound (OCT compound) and sliced as 20-mm
905 sections using a Cryostat microtome (Leica). For immunostaining, sections were washed with
906 PBS once, followed by permeabilized and blocked in PBS containing 0.2% TritonX-100 and
907 10% bovine serum albumin for 1 hour at room temperature, then incubated with primary
908 antibody (MAP2 1:1000; NeuN 1:1000, diluted in blocking solution) at 4 °C overnight.
909 Primary antibody was visualized using the appropriate secondary antibody conjugated to
910 Alexa Fluor 488, or Alexa Fluor 594 (1:500, Thermo Fisher Scientific). Nuclei were visualized
911 with Hoechst 33342 (1:1000, Thermo Fisher Scientific). All images were captured using a
912 Zeiss LSM 900 confocal microscope and the ZEN software.

913 **Image Processing**

914 **Quantification of fixed z-stack imaging.** Image data were acquired at 8 or 16 bits,
915 with voxel sizes of 1 μm x 0.62 μm x 0.62 μm . Image files extracted from the confocal
916 Zeiss microscope (.czi format) were loaded into Python using the ‘aicsimageio’ package and
917 converted to floating-point format in the range [0, 1]. Confocal image acquisition settings
918 were kept consistent within each imaging batch.

919 A pre-trained model (“cyto2” from Cellpose [118]) was applied to segment NeuN+ cell bodies
920 per image. For images sampled at 0.62 μm along the xy-plane, segmentation on the NeuN
921 channel in 3D produced the best results. For images sampled at 0.31 μm along the xy-plane,
922 segmentation on the NeuN and Hoechst channels in 2D (xy), with subsequent stitching along
923 the z-axis, produced the best results. Specific segmentation settings were determined for each
924 imaging experiment. Segmentation quality was assessed manually, blinded to condition, and
925 images with low-quality segmentations were discarded.

926 The model outputs per-voxel probabilities representing the Bernoulli probability that a given
927 voxel lies within a cell (any cell) and per-voxel masks—recovered from flow vectors and
928 from the pixel probabilities output by the model—representing regions of interest (cells).
929 We leveraged these per-voxel probabilities to compute the expected fluorescence intensity
930 $E(I_t)$ for our target channel t in each cell c . This is calculated as $E(I_t) = a \cdot b$, where
931 a is a 1-dimensional vector containing the measured intensities for channel t across all n
932 voxels annotated as part of the region of interest for cell c , and b is a 1-dimensional vector
933 of the same length n . Each element b_i in b represents the normalized probability that the
934 corresponding voxel i belongs to cell c , calculated as:

$$935 b_i = \frac{\Pr(v_i \in c)}{\sum_{j=0}^{n-1} \Pr(v_j \in c)}$$

936 This normalization ensures that the probabilities sum to 1, providing a weighted contribution
937 of each voxel to the total expected fluorescence intensity for the cell.

938 A linear mixed-effects model was fit (using ‘mixedlm()’ from the ‘statsmodels’ package) to
939 cell-level average fluorescence intensities, with treatment or genotype as a fixed effect and
940 well-of-origin as a random effect; formalized as follows:

$$941 Y_{ij} = \beta_0 + \beta_1 X_{ij} + u_j + \epsilon_{ij}$$

942 where: - Y_{ij} is the observed fluorescence intensity for cell i in well j , - β_0 is the intercept, - β_1
943 is the coefficient for the fixed effect (treatment or genotype), - X_{ij} is the fixed effect predictor
944 (treatment or genotype) for cell i in well j , - u_j is the random effect for well j , assumed to be
945 normally distributed with mean 0 and variance σ_u^2 , - ϵ_{ij} is the residual error for cell i in well

946 j , assumed to be normally distributed with mean 0 and variance σ^2 .

947 Where indicated, measurements were combined over multiple differentiation batches (inde-
948 pendent staining and imaging experiments). To this end, an equal number of cells from each
949 experimental condition were sampled uniformly per batch, fluorescent values were z-scaled
950 within that batch, and then combined. Indicator vectors for well-of-origin and batch-of-origin
951 were included in the model. Before applying this linear transformation, per-cell per-image
952 clipping was determined to be low (< 0.1%) and the response function of the confocal
953 microscope was assumed to be linear.

954 For each condition, representative images were chosen from a single batch as the images
955 closest to the mean fluorescence intensity for each condition. Voxels not belonging to a cell
956 (i.e., not used in quantification) were masked prior to mean-projection for visualization.

957 **Quantification of live single-plane imaging** Single-plane live imaging data were bi-
958 narized using a threshold set at the 75th intensity percentile for each channel of interest
959 (TMRM or CellROX), and mean fluorescence intensities within these masked regions were
960 calculated following previously established methodology ([119]). The standardized intensity
961 threshold (75th percentile) was empirically selected to reliably identify high-fluorescence areas
962 across experimental conditions.

963 **Quantification of live single-plane imaging with FCCP** For time-course experiments
964 involving FCCP treatment, images acquired before and after treatment were aligned using
965 Fourier-based image registration. Spatial shifts between time points were estimated by
966 phase cross-correlation and corrected using Fourier transformations. Alignment accuracy was
967 manually verified by visual inspection. A binary mask defining regions of high fluorescence
968 intensity was generated from the 75th percentile threshold of the initial (baseline) TMRM
969 image. This baseline-derived mask was consistently applied across all subsequent time points
970 to quantify mean fluorescence intensities within these regions.

971 **Oxygen Consumption Rate Data Analysis**

972 The oxygen consumption rate (OCR) of cells was determined over time using a Seahorse
973 XF Analyzer. Prior to analysis, OCR curves were visually inspected in a blinded manner
974 to exclude wells that did not respond to drug injections. To calculate per-well total oxygen
975 consumption for a given experimental period (e.g., under basal conditions prior to injections
976 of uncouplers), integrals between specific experimental time points were computed from the
977 OCR curve. The following measurements were made:

1. Basal respiration was computed as the total oxygen consumption prior to oligomycin injection.
2. Proton leak was computed as the total oxygen consumed after oligomycin injection and prior to FCCP injection.
3. Maximal respiration was computed as the total oxygen consumption after FCCP and prior to Rotenone + Antimycin injection.
4. Relative uncoupling was computed as the fraction of basal respiration attributed to proton leak.
5. Spare respiratory capacity was determined as the ratio of maximal respiration to basal respiration.

LC-MS Data Analysis

LC-MS Lipidomics Data Analysis. Lipids were identified, and their signals integrated using the Lipidsearch © software (version 4.2.27, Mitsui Knowledge Industry, University of Tokyo). Integrations and peak quality were curated manually. Peak areas were first background-corrected by subtracting three times the median peak area measured in blank samples; negative values resulting from this correction were set to zero. Statistical comparisons between different cell lines were performed using Welch's t-test (`scipy.stats.ttest_ind, equal_var=False`). For comparisons involving treatment conditions within the same cell line, Student's t-test (`scipy.stats.ttest_ind, equal_var=True`) was used, assuming equal variance due to identical genetic backgrounds.

LC-MS Metabolomics Data Analysis. Data were analyzed using Compound Discoverer 3.2 (Thermo Fisher Scientific). Metabolite identification was based either on MS2/MS3 spectral matching against a local mzVault library and corresponding retention times from pure standards (Level 1), or spectral matching using mzCloud (Level 2). Each metabolite identification was manually inspected. Peak areas were first background-corrected by subtracting three times the median peak area measured in blank samples; negative values resulting from this correction were set to zero. Median-centered peak areas were scaled (`StandardScaler()` from scikit-learn) prior to principal component analysis (PCA). The Harvard Center for Mass Spectrometry identified three samples with notably low overall metabolite intensities, which were subsequently excluded from downstream analyses.

1008 **Targeted LC-MS Metabolite Analysis in Media Samples.** Peak areas from targeted
1009 metabolite analysis of media samples were compared for CDP, CDP-choline, and choline. To
1010 ensure accurate detection, solvent blanks were analyzed: CDP and CDP-choline were not
1011 detected in these blanks, while choline was detected at levels several orders of magnitude
1012 lower than in media samples.

1013 **Bulk mRNA Sequencing of iNs**

1014 **Bulk mRNA Sequencing Data Processing.** Sequencing data were processed using the
1015 BMC/BCC pipeline version 1.8 (updated 06/06/2023). Further details of the pipeline are
1016 available at: https://openwetware.org/wiki/BioMicroCenter:Software#BMC-BCC_Pipe
1017 line by the MIT BioMicro Center. Fastq files were subsequently processed in-house using
1018 STAR and featureCounts. Human reference genome (GRCh38.p14, GENCODE release 47)
1019 and annotation files were downloaded from GENCODE and indexed using STAR (version
1020 recommended parameters). Sequencing reads were trimmed using Trim Galore with Nextera-
1021 specific settings and a stringency of 3, requiring a minimum overlap of 3 bases with adapter
1022 sequences for trimming. Trimmed reads were then mapped to the indexed human genome
1023 using STAR, with paired-end reads processed concurrently. Gene-level counts were generated
1024 using featureCounts with settings optimized for paired-end data: counting only read pairs
1025 with both ends aligned (-B), excluding pairs mapping to different chromosomes or strands
1026 (-C), and counting fragments rather than individual reads (-p). Counts were summarized at
1027 the exon level, and grouped by gene identifier.

1028 **Differential gene expression analysis.** Differential gene expression analysis was per-
1029 formed using edgeR and limma-voom. Counts were filtered to retain protein-coding genes
1030 expressed at a minimum of 1 count-per-million (CPM) in at least one sample. Normalization
1031 factors were calculated, and linear modeling was conducted using limma's voom method,
1032 followed by empirical Bayes moderation (eBayes). Statistical comparisons were performed
1033 using contrasts tailored to experimental conditions (treatment and genotype) within batches,
1034 and results were summarized as log-fold changes with associated p-values.

1035 **Gene set enrichment analysis.** Gene set enrichment analysis was conducted using Fast
1036 Gene Set Enrichment Analysis (FGSEA). Differentially expressed genes were ranked by a
1037 score calculated as the sign of log-fold change multiplied by the negative log-transformed
1038 p-value. Pre-defined gene sets were evaluated with FGSEA using 10,000 permutations, and
1039 significant pathways were identified based on adjusted p-values < 0.05. Leading-edge genes
1040 from these significant pathways were partitioned along with their associated pathways as

1041 described in "Gene-pathway clustering using Kernighan-Lin heuristic."

1042 **Gene-Pathway K/L Cluster Similarity Analysis.** Jaccard indices were computed to
1043 assess similarity between gene-pathway clusters. Empirical p-values for the overlaps were
1044 obtained by comparing observed overlaps against 1000 random permutations, and p-values
1045 were adjusted using the Benjamini-Hochberg method to control the false discovery rate.

1046 **Single-cell Transcriptomic Data Processing**

Variant calling and ROSMAP subject selection. A total of 36 individuals were selected from the ROSMAP cohort, a longitudinal cohort study of aging and dementia in elderly nuns, priests, and brothers. Processed whole genome sequencing (WGS) variant call files for all ROSMAP samples, where available ($N = 1249$ sequencing samples), were downloaded from Synapse (syn11724057). Variant call data were downloaded for chromosomes harboring SORL1, TREM2, ABCA7, ATP8B4, ABCA1, and ADAM10 (see Github Repository). When more than one WGS sample existed for a given subject, the sample with the higher Genomic Quality Score was chosen. Only samples that did not have sex mismatches and were consistent with previous array-based genotype data were considered (see syn12178037). Only variants that passed quality control ('FILTER_{PASS}') were reconsidered.

1047 Potential PTC (protein-truncating) variants in each of the aforementioned genes were flagged
1048 based on the following criteria: the variant had to be either a splice, missense, frameshift,
1049 nonsense, or premature start variant and be annotated as 'LOF' (loss of function). For
1050 ABCA7, this filtering captured known ABCA7 LoF risk variants from the literature, except
1051 for c.5570+5G>C, which was manually added to the filtered variants. Also see syn10901595
1052 (<https://www.synapse.org/#!Synapse:syn10901595>) for information on WGS library prepara-
1053 tion, quality control, variant annotations, and impact predictions. Annotated ABCA7 PTC
1054 variants are shown in Data ??.

1055 The WGS data was used to identify 12 subjects who did not carry a known PTC variant in one
1056 of the aforementioned genes, other than in ABCA7, and for whom fresh-frozen postmortem
1057 tissue was available for request from Rush University (termed 'LoF' samples). We also
1058 selected 24 individuals who do not carry a single ABCA7 PTC mutation or PTC variants in
1059 one of the aforementioned genes (termed 'control' samples). Control samples were matched
1060 on age, sex, and pathology.

1061 **Read Counting Alignment.** Library demultiplexing was performed using the BMC/BCC
1062 pipelines BioMicroCenter Software. Fast-q reads were aligned to the human genome GRCh38

1063 and counted using the ‘cellranger count()’ function from Cell Ranger version 6.1.2 (10x
1064 Genomics). Introns were included in counting to allow for the detection of unspliced transcripts,
1065 and the expected number of cells was set to 5000. Otherwise, Cell Ranger (v.6.1.2) default
1066 parameters were used. Counts across individual samples were then aggregated using a custom
1067 aggregation script (see GitHub Repository), resulting in a total of 150,456 cells.

1068 **Sample Swap Analysis.** Sample swap analysis was performed using a previously estab-
1069 lished pipeline (MVV; QTLtools_1.1) [120], which compares allelic concordance between
1070 genomic and transcriptomic sequencing data. As input, we used the BAM files generated in
1071 the cellranger counting step and the chromosome 19 (the chromosome harboring ABCA7)
1072 variant call files (VCF). When comparing the concordance of BAM and VCF data for ho-
1073 mozygous and heterozygous sites, the expected WGS sample appeared as a clear outlier
1074 (more consistent along both dimensions than any of the other 1249 WGS ROSMAP samples)
1075 for all single cell samples (Figure ??).

1076 **Cell filtering metrics.** Prior to cell type annotation, we performed a series of quality
1077 control steps on the aggregated counts matrix. First, we filtered cells based on N_g , the
1078 number of genes for each cell where counts > 0, and kept cells for which $500 < N_g < 10000$.
1079 Next, we removed all cells with a high fraction of counts from mitochondrial-encoded genes.
1080 Mitochondrial fraction (M_f) is a commonly used per-cell metric to measure compromised
1081 nuclear integrity, with high fractions indicating low-quality nuclei, where C_{mt} is the total
1082 counts of mitochondrial-encoded genes for a cell, C_t is the total count of all genes for the
1083 same cell, and $M_f = \frac{C_{mt}}{C_t}$.

1084 We fit a Gaussian mixture model (GMM) using sklearn’s GaussianMixture implementation to
1085 $M'_f = \log_{10}(M_f + \epsilon)$, where ϵ is a small value added to M_f to avoid taking the logarithm of zero.
1086 A GMM models the data as independently sampled from a mixture of k Gaussian probability
1087 densities parameterized by a mean μ_k , a variance σ_k , and a mixture weight π_k indicating
1088 the proportion of the data derived from each component. The following log-likelihood
1089 function was maximized: $\ln[L(\theta|M'_f)] = \sum_{i=0}^n \ln \left(\sum_{j=0}^k \pi_j N(M'_{fi}|\mu_j, \sigma_j) \right)$ The model with
1090 $k = 5$ components had the lowest Bayesian information criterion (BIC) score (GridSearchCV
1091 from sklearn.preprocessing), where: $BIC = -2 \ln(L) + k \ln(n)$ where L is the maximized
1092 log-likelihood of the model, and n is the number of observations (cells). Finally, each cell i is
1093 assigned a component in k according to: $\text{argmax}_k [\pi_k N(M'_{fi}|\mu_k, \sigma_k)]$ Cells assigned to the
1094 component k with the highest mean M'_f scores were presumed to constitute a population
1095 of low-quality cells and were removed from further analysis. This initial filtering removed
1096 approximately 20,000 cells.

1097 Considering all remaining cells in marker-gene expression space, where marker genes include
1098 only known cell type-specific genes for the major human PFC cell types, including astrocytes
1099 (159 markers), excitatory neurons (113 markers), inhibitory neurons (83 markers), microglia
1100 (97 markers), oligodendrocytes (179 markers), OPCs (143 markers), and vascular cells (124
1101 markers) (Reference 1; Table ??), normalized to total library size $NC_m = \frac{C_m}{C_t}$, where NC_m
1102 and C_m are respectively the normalized and unnormalized count values for a given marker
1103 gene m and C_t is the total counts of all genes for the same cell. Next, we performed a
1104 memory-efficient implementation of singular value decomposition (IncrementalPCA from
1105 sklearn.decomposition) to transform cells from the marker-gene space (mean-centered and
1106 unit-variance) into a lower dimensional space (top 50 principal components sorted by variance).
1107 Visually, the cells formed a number of Gaussian-like clusters when projected onto the first
1108 two principal components. Under the assumption that each Gaussian cluster represented a
1109 different cell type in the brain, we again fit a GMM, as described above, except this time
1110 parameterized by a covariance matrix Σ_k instead of variance σ_k , to the projected data. The
1111 model with $k = 10$ and full covariance had the lowest BIC score. Each resulting cell cluster
1112 was enriched for a subset of major cell type markers in the brain, indicating clusters of
1113 astrocytes, microglia, OPCs, oligodendrocytes, excitatory neurons, inhibitory neurons, and a
1114 heterogeneous cluster of vascular cells.

1115 To remove cells that were not well-explained by the GMM and likely represent low-quality
1116 cells, we next computed the per-cell log-probability given the model $L_i = \ln[P(x_i|\theta)]$, using
1117 Sklearn's GaussianMixture 'score_samples' function, and removed cells with $L_i < -100$. We
1118 also removed two Gaussian clusters whose probability distributions constituted clear outliers
1119 compared to remaining clusters. The excluded cells had lower C_t and higher M_f compared
1120 to those that passed the log-likelihood filter, suggesting that the removed cells were indeed
1121 of low quality. As expected, when examining the data visually projected onto the first two
1122 principal components, this filtering removed many of the cells that were not visibly associated
1123 with a main Gaussian cluster. Together, this filtering removed an additional approximately
1124 12,000 cells, leaving a total of 118,668 cells.

1125 **Gene filtering metrics.** For the remaining downstream analysis we only considered genes
1126 that were both nuclear-encoded and protein-coding, which constituted a total of 19384 genes,
1127 based on annotation of ensembl GRCh38p12.

1128 **Cell type annotations.** To remove variance explained by sequencing batch and individual-
1129 of-origin, we first applied the Python implementation of the Harmony algorithm [121] with
1130 individual-of-origin as an indicator vector to the low-dimensional embedding of cells (first 50

1131 principal components) remaining after the initial rounds of quality control described above.
1132 Next, we computed a neighborhood graph on the Harmony-corrected values in the PC embed-
1133 ding space, as implemented in the Scanpy Python package [122], using default parameters.
1134 Finally, we applied the Leiden graph-clustering algorithm to cluster this neighborhood graph
1135 of cells, using the Scanpy implementation of the Leiden algorithm [123].

1136 We used the Scanpy 'rank_genes_groups' function to compute top marker genes per Leiden
1137 cluster. Briefly, we assigned a major cell type label c to each Leiden cluster, where $c \in$
1138 {'Ex', 'In', 'Ast', 'Mic', 'Oli', 'Opc', 'Vascular'}, by computing the average cell-type-specific
1139 marker gene enrichment per Leiden cluster. Specifically, this is a vector of cell type signatures
1140 S_c for each Leiden cluster, where $S_c = \frac{1}{n} \sum_{i=0}^n \log_2 \left(\frac{I_i^{\text{In}}}{I_i^{\text{Out}}} \right)$ where n is the total number of
1141 marker genes assigned to a cell type in c and I_i^{In} and I_i^{Out} indicate average gene expression
1142 values for a gene i for cells inside or outside a specific Leiden cluster, respectively. Then
1143 each Leiden cluster is assigned a label c by $\text{argmax}_c(S_c)$. Finally, we sub-clustered cells from
1144 each major cell type using the Leiden clustering algorithm and examined distributions of
1145 mitochondrial fractions M_f and total counts C_t among subclusters s of the same cell type.
1146 Clusters were removed if $M_{f_s} > (2 \cdot \text{std}(M_f) + \overline{M_f})$ or if $|C_{t_s}| > (2 \cdot \text{std}(C_t) + \overline{C_t})$, where M_{f_s}
1147 and C_{t_s} are respectively the mean M_f and C_t for all cells in a given Leiden cluster s and $\overline{M_f}$
1148 and $\overline{C_t}$ are respectively the means of those values across all Leiden clusters, considering only
1149 clusters with the same cell type annotation c , because variance in M_f and C_t across major
1150 cell types can be biologically explained. Manual inspection of the removed clusters revealed
1151 that they tended to have fewer cells and low individual-level representations, and were not
1152 well-connected in the graph.

1153 **Individual-level filtering.** After all rounds of quality control as described above, we noted
1154 a subset of individuals ($N = 6$) with very few cells (< 500). These subjects were removed from
1155 further analysis, resulting in 24 control individuals and 12 ABCA7 LoF individuals. None of
1156 these individuals carried ABCA7 PTC variants, and removing them did not substantially
1157 alter the distribution of clinical variables across genotypes.

1158 **Differential gene expression.** Summed (pseudo-bulked) gene expression values were
1159 computed by matrix multiplication XI , where X is the gene x cell counts matrix and I is a
1160 cell x individual binary matrix indicating the individual-of-origin for each cell, resulting in 36
1161 gene expression vectors for each of the six major cell types. For each cell type, only genes
1162 with a nonzero detection rate > 0.10 were considered for differential expression. Summed
1163 counts were normalized using the edgeR TMM method. The residual mean-variance trend
1164 not explained by the multivariate linear model (formalized below) was removed using Limma-

1165 Voom. Unknown sources of variance were captured in the model using surrogate variable
1166 analysis (SVA). Limma's lmFit, eBayes, and topTable functions were then used to estimate
1167 differential gene expression statistics, as reported in Data ???. The following model was fit for
1168 each cell type: $G_i = \beta_0 \times \text{ABCA7LoF} + \beta_1 \times \text{msex} + \beta_2 \times \text{nft} + \beta_3 \times \text{amyloid} + \beta_4 \times \text{age_death} +$
1169 $\beta_5 \times \text{PMI} + \beta_6 \times \text{batch} + \beta_7 \times \text{APOE4} + \beta_8 \times \text{SV0}$ G_i refers to a vector of expression profiles
1170 of size 1×36 for a gene i in a given cell type. ABCA7LoF is a binary variable, encoding
1171 the presence of an ABCA7 variant predicted to cause loss of function (see Data ???). See
1172 Supplementary Text for descriptions of the remaining variables included in the model. SV0
1173 refers to the first surrogate variable estimated from the data. The exact number of surrogate
1174 variables per cell type to include as additive terms in the model was estimated using the
1175 num.sv() function in R.

1176 **Gene-pathway projections.** For each cell type, we computed a set of gene-wise scores
1177 quantifying the direction and statistical significance of gene expression changes (computed
1178 as part of the differential gene expression analysis) associated with ABCA7 LoF: $S =$
1179 $\text{sign}(\log_2 \text{FC}) \times -\log_{10}(\text{p-value})$ where $\log_2 \text{FC} > 0$ indicates up-regulation in ABCA7 LoF
1180 vs control. Top differentially expressed genes per cell type ($|S| > 1.3$) were projected from
1181 6-dimensional score space, where each dimension captures ABCA7 LoF perturbation scores
1182 in one of the major cell types (Ex, In, Ast, Mic, Oli, OPC), into two dimensions, using the
1183 UMAP algorithm (using the 'umap' Python package). Gene scores that were not detected in
1184 >10% of cells in a given cell type were set to 0.

1185 We performed a grid search for Gaussian mixture parameters (parameter 1: number of
1186 components; parameter 2: covariance type) on the embedded cells (using the Python 'sklearn'
1187 package) to assign genes to clusters in the 2D space. We proceeded with the model with the
1188 lowest BIC score, which had 15 components and a tied covariance matrix.

1189 Each cluster was assigned representative pathway names by testing genes in that cluster
1190 for enrichment with Gene Ontology Biological Process pathways (Table ??) against the
1191 background of all genes in the embedding space, by hypergeometric enrichment (using the
1192 Python package 'gseapy'). Pathways with an enrichment p-value < 0.01 were considered for
1193 cluster annotation.

1194 Per-cell-type perturbation scores (S_c) for each cluster were computed as the average gene
1195 score S (for a given cell type) for all genes in that cluster. The statistical significance of
1196 each cell type-specific cluster score was assessed by permuting cluster assignments (100,000
1197 permutations).

1198 **Gene-set enrichment.** Genes were rank-ordered based on their scores S (see description
1199 in Gene-Pathway Projections). An R implementation of gene set enrichment analysis (GSEA)
1200 [124] (fast gene set enrichment analysis, fGSEA) was run with 10,000 permutations to estimate
1201 the statistical overrepresentation of gene sets in the WikiPathways databases (Table ??)
1202 within high-scoring ($|S|$), differentially expressed genes. Gene sets with a minimum size of 5
1203 and a maximum size of 1000 were considered.

1204 **Gene-pathway clustering using Kernighan-Lin heuristic.** To reduce the solution's
1205 computational search space, we reformulated the gene-pathway association problem as a
1206 bipartite graph G constructed from all the genes in the Leading Edge subset (LE) and their
1207 associated pathways. LE was defined as the set of 268 genes driving the enrichment signal
1208 for pathways that passed a significance threshold of $p < 0.05$ (fGSEA) in Con vs. ABCA7
1209 LoF excitatory neurons. G was constructed from an $n \times m$ unweighted adjacency matrix,
1210 where n represented the number of LE genes and m represented the number of pathways
1211 associated with four or more LE genes, as specified in the WikiPathways database.

1212 We chose to group gene-pathways into clusters of approximately equal size, making this a
1213 graph partitioning problem. We found that removing this constraint made the grouping
1214 results highly susceptible to outliers (Supplementary Text; Figure ??C). Of the three graph
1215 partitioning algorithms tried, METIS and the Kernighan-Lin (K/L) algorithms had the lowest
1216 loss (Supplementary Text; Figure ??B). Both METIS and K/L achieved very comparable
1217 losses (within 1.8% of each other, after 5.0×10^4 random initiations) and produced almost
1218 identical solutions (Rand index=0.98, after 5.0×10^4 random initiations) (Supplementary
1219 Text; Figure ??B, D-F). We proceeded with the K/L algorithm for gene-pathway groupings
1220 as we found this algorithm to perform consistently better than METIS across a wider range
1221 of graph sizes (not shown).

1222 The K/L algorithm was implemented in Python (see GitHub Repository) based on its original
1223 paper [125] and run with parameters set as $C = 0$, $KL_modified = True$, $random_labels =$
1224 $True$, $unweighted = True$, and $K = 50$ to partition G into 8 groups. We performed 5.0×10^4
1225 random initiations on G and report the partitioning with the lowest loss among all initiations.

1226 Gene-pathway graph layouts were computed using the ‘networkx’ Python package with the
1227 spring layout algorithm, using 10,000 iterations. Layouts were visualized using the ‘matplotlib’
1228 ‘pyplot’ package in Python.

1229 Representative pathways for each cluster were inferred from the graph by averaging the
1230 ABCA7 LoF perturbation scores S for all genes in the cluster of interest sharing an edge with

1231 the pathway in question. Scores for pathways with intra-cluster degrees ≥ 5 were reported in
1232 the figures. Manually picked subsets of genes with the largest scores ($|S| > 1$) were reported in
1233 the figures. All gene statistics are reported in Data ??, and cluster assignments are reported
1234 in Data ??.

1235 **Excitatory neuronal layer annotation.** Excitatory neurons were annotated by cortical
1236 layer using previously published marker gene sets [126] (Table ??). The normalized gene
1237 expression matrix (post-quality control described above) for excitatory neurons was filtered
1238 to include only layer-specific marker genes and cells expressing at least 15% of these genes.
1239 Dimensionality was reduced using iterative principal component analysis (iPCA), and batch
1240 effects from individual subjects were corrected using Harmony. A neighborhood graph was
1241 constructed based on these corrected components, followed by Leiden clustering to identify
1242 neuronal clusters. Clusters were annotated by calculating the average log-fold change of
1243 layer-specific marker genes. Clusters with significant enrichment (average log-fold change
1244 > 0.1) were labeled by cortical layer, while ambiguous clusters were removed from further
1245 analysis. Layer 5 and 6 annotations were combined into a single 'L5/6' category. These
1246 annotations were confirmed using marker genes from an independent study [127] (Table ??).
1247 Per-layer differentially expressed genes were computed as described in the section "Differential
1248 Gene Expression," followed by gene set enrichment analysis of ABCA7 LoF-associated K/L
1249 clusters in excitatory neurons as described in the section "Gene Set Enrichment."

1250 **ABCA7 p.Ala1527Gly variant calling and gene-pathway clustering comparisons.**
1251 We followed the same steps indicated in the section "Variant Calling and ROSEMAP Subject
1252 Selection" to identify subjects who carried the p.Ala1527Gly variant and had snRNAseq
1253 performed on the PFC as part of a previous study. Differentially expressed genes were
1254 computed as described in the section "Differential Gene Expression," followed by gene set
1255 enrichment analysis of ABCA7 LoF-associated K/L clusters in excitatory neurons as described
1256 in the section "Gene Set Enrichment."

1257 **Molecular Dynamics Simulations**

1258 The initial structure of ABCA7 was obtained from the Protein Data Bank (PDB) in unbound-
1259 open and bound-closed conformations, PDB IDs 8EE6 and 8EOP, respectively. These
1260 experimentally solved structures harbor the G1527 variant. The A1527 structure was
1261 generated by mutating the glycine residue to alanine using pymol software.

1262 The ABCA7 domain between residues 1517 and 1756 was embedded in a dipalmitoylphos-
1263 phatidylcholine (DPPC) membrane using the CHARMM-GUI web server and oriented

according to the Orientations of Proteins in Membranes (OPM) database. Four different simulations were performed using GROMACS 2022.3, as reported in Table ???. The CHARMM36M force field was used for all simulations.

The protein-membrane system was solvated in a cubic box with a minimum distance of 1.0 nm between the protein and the box edge, using the TIP3P water model. Energy minimization was performed using the steepest descent algorithm with a maximum force threshold of 1000 kJ/mol/nm to relieve any steric clashes or bad contacts. The system was equilibrated in six phases, each 125 ps long, to equilibrate volume (NVT) and pressure (NPT). The production run, 300 ns long, was performed in the NPT ensemble at 323 K using a v-rescale thermostat and 1 bar using the Parrinello-Rahman barostat. A 2 fs time step with h-bonds constraints was used with periodic boundary conditions applied in all directions. Long-range electrostatics were handled using the Particle Mesh Ewald (PME) method with a cutoff of 1.0 nm for non-bonded interactions.

RMSD was calculated to monitor the conformational stability of a given structure over the course of the simulation by comparing the position of C_α at time t under simulation to its reference position (in 8EOP or 8EE6). The ϕ and ψ dihedral angles were calculated using the *gmx rama* tool, followed by post-processing. Secondary structure analysis was performed using *gmx dssp -hmode dssp*, with subsequent post-processing using custom Python scripts.

Principal Component Analysis (PCA) was conducted to identify the major conformational changes during the simulation. The analysis involved the following steps:

1. A covariance matrix of the C_α atom positional fluctuations was constructed using the ‘*gmx covar*’ tool.
2. The covariance matrix was diagonalized to obtain the eigenvalues and eigenvectors, representing the principal components (PCs).
3. The trajectory was projected onto the first two principal components (PC1 and PC2) using the ‘*gmx ana eig*’ tool to visualize the dominant motions.
4. A kernel density estimate (KDE) plot implemented in seaborn python3 was used to visualize the first two eigenvectors for each simulation, corresponding to 45%, 40%, 40% and 33% of variance in 8EOP-G1527, 8EE6-A1527, 8EE6-G1527 and 8EOP-A1527 respectively.

Visualization of the trajectories was carried out using VMD software.

1295 **Supplementary Text**

1296 **Description of variables according to the Rush Alzheimer's Disease Center Code-**
1297 **book.**

- 1298 1. **age_death.** Age at death
- 1299 2. **amyloid.** Overall amyloid level - Mean of 8 brain regions. Amyloid beta protein identi-
1300 fied by molecularly-specific immunohistochemistry and quantified by image analysis.
1301 Value is percent area of cortex occupied by amyloid beta. Mean of amyloid beta score
1302 in 8 regions (4 or more regions are needed to calculate). The 8 regions are hippocampus,
1303 entorhinal cortex, midfrontal cortex, inferior temporal gyrus, angular gyrus, calcarine
1304 cortex, anterior cingulate cortex, superior frontal cortex.
- 1305 3. **braaksc.** Braak stage. Semi quantitative measure of neurofibrillary tangles. Braak
1306 Stage is a semi quantitative measure of severity of neurofibrillary tangle (NFT) pathology.
1307 Bielschowsky silver stain was used to visualize NFTs in the frontal, temporal, parietal,
1308 entorhinal cortex, and the hippocampus. Braak stages were based upon the distribution
1309 and severity of NFT pathology: Braak stages I and II indicate NFTs confined mainly
1310 to the entorhinal region of the brain; Braak stages III and IV indicate involvement of
1311 limbic regions such as the hippocampus; Braak stages V and VI indicate moderate to
1312 severe neocortical involvement.
- 1313 4. **ceradsc.** CERAD score. Semiquantitative measure of neuritic plaques. CERAD score is
1314 a semiquantitative measure of neuritic plaques. A neuropathologic diagnosis was made
1315 of no AD (value 4), possible AD (value 3), probable AD (value 2), or definite AD (value
1316 1) based on semiquantitative estimates of neuritic plaque density as recommended by
1317 the Consortium to Establish a Registry for Alzheimer's Disease (CERAD), modified
1318 to be implemented without adjustment for age and clinical diagnosis. A CERAD
1319 neuropathologic diagnosis of AD required moderate (probable AD) or frequent neuritic
1320 plaques (definite AD) in one or more neocortical regions. Diagnosis includes algorithm
1321 and neuropathologist's opinion, blinded to age and all clinical data. Value 1: definite
1322 AD, Value 2: probable AD, Value 3: possible AD, Value 4: no AD.
- 1323 5. **cogdx.** Final consensus cognitive diagnosis. Clinical consensus diagnosis of cognitive
1324 status at time of death. At the time of death, all available clinical data were reviewed
1325 by a neurologist with expertise in dementia, and a summary diagnostic opinion was
1326 rendered regarding the most likely clinical diagnosis at the time of death. Summary
1327 diagnoses were made blinded to all postmortem data. Case conferences including one

1328 or more neurologists and a neuropsychologist were used for consensus on selected cases.
1329 Value 1: NCI, No cognitive impairment (No impaired domains), Value 2: MCI, Mild
1330 cognitive impairment (One impaired domain) and NO other cause of CI, Value 3: MCI,
1331 Mild cognitive impairment (One impaired domain) AND another cause of CI, Value
1332 4: AD, Alzheimer's disease and NO other cause of CI (NINCDS PROB AD), Value
1333 5: AD, Alzheimer's disease AND another cause of CI (NINCDS POSS AD), Value 6:
1334 Other dementia. Other primary cause of dementia

- 1335 6. **msex.** Sex. Self-reported sex, with "1" indicating male sex. 1 = Male 0 = Female
- 1336 7. **nft.** Neurofibrillary tangle burden. Neurofibrillary tangle summary based on 5 regions.
1337 Neurofibrillary tangle burden is determined by microscopic examination of silver-stained
1338 slides from 5 regions: midfrontal cortex, midtemporal cortex, inferior parietal cortex,
1339 entorhinal cortex, and hippocampus. The count of each region is scaled by dividing
1340 by the corresponding standard deviation. The 5 scaled regional measures are then
1341 averaged to obtain a summary measure for neurofibrillary tangle burden.
- 1342 8. **pmi.** postmortem interval. Time interval in hours from time of death to autopsy.
1343 postmortem interval (PMI) refers to the interval between death and tissue preservation
1344 in hours.

1345 **Choosing a partitioning heuristic for gene-pathway grouping**

1346 **Methods.** The heatmap in Figure ??A highlights how frequently pathways within a pathway
1347 database, such as WikiPathways, share gene members. On average, every pathway shown
1348 in Figure ??A shares at least one gene with approximately 40% of the other pathways,
1349 highlighting that there is redundancy in this matrix that could be summarized in simpler
1350 terms.

1351 To summarize redundant gene-pathway information into a limited number of non-redundant
1352 gene-pathway groups, we reformulated the gene-pathway association problem as a bipartite
1353 graph G constructed from all the genes in the Leading Edge subset (LE) and their associated
1354 pathways. LE was defined as the set of 268 genes driving the enrichment signal for pathways
1355 that passed a significance threshold of $p < 0.05$ (fGSEA) in Con vs. ABCA7 LoF excitatory
1356 neurons. G was constructed from an $n \times m$ unweighted adjacency matrix, where n represented
1357 the number of LE genes and m the number of pathways associated with four or more LE
1358 genes, as specified in the WikiPathways database.

1359 Graph partitioning involves segmenting the vertices of a graph into equal-sized partitions,
1360 optimizing for the minimal number of interconnecting edges (i.e., “total cut size”). We
1361 tested three prominent graph partitioning techniques, as outlined by Elsner (1997) [128], to
1362 approximate optimal partitioning. These methods include:

1363 1. **Recursive Spectral Bisection:** Implemented in Python using the numpy linear
1364 algebra package, this method was executed for $\log_2(N)$ iterations, yielding $N = 8$
1365 partitions. A detailed description of the algorithm can be found in Elsner (1997) [128].

1366 2. **Multilevel Graph Partitioning:** Leveraging the METIS software package [129] in
1367 Python using the following parameters: ‘nparts=8’, ‘tpwgts=None’, ‘ubvec=None’,
1368 ‘recursive=False’.

1369 3. **Kernighan-Lin (K/L) Algorithm:** Based on its original paper [125], this algorithm
1370 was implemented in Python and run with parameters set as $C = 0$, ‘KL_modified=True’,
1371 ‘random_labels=True’, ‘unweighted=True’, and $K = 50$.

1372 Additionally, the Spectral Clustering algorithm, a commonly used clustering method, was
1373 applied using the ‘SpectralClustering()’ function from the ‘sklearn’ Python package with
1374 default parameters, apart from ‘n_clusters=8’ and ‘assign_labels=’kmeans’’. We stipulated
1375 eight clusters for each algorithm, as qualitatively, this resolution seemed to strike a good
1376 balance to summarize main biological effects.

1377 For benchmarking purposes, the three graph partitioning techniques and the spectral clustering

algorithm were evaluated by segmenting graph G into eight gene-pathway clusters using the respective algorithms. Spectral clustering was run over 1,000 initiations, while K/L and METIS were run over 50,000 iterations because their solutions were slightly more variable across runs. The deterministic bisection method was run only once. A randomized graph partitioning benchmark was also computed by permuting the eight cluster labels of approximately equivalent size for 1,000 initiations. Average losses were computed per algorithm on all initiations. The benchmarking process and source code are available at: GitHub Repository.

Results. Spectral clustering performed significantly better than all other algorithms based on the loss (Figure ??B). This was expected, as spectral clustering does not place a constraint on cluster size. Spectral clustering results were characterized by a single large cluster and many small clusters (Figure ??C), indicating that this clustering algorithm was highly susceptible to outliers and suggesting that graph partitioning, which imposes the constraint of equal partitioning, was a better approach to the problem of grouping genes and pathways into biologically informative groups. Indeed, all three graph partitioning algorithms divided the graph into more uniformly-sized groups (Figure ??C). Among the partitioning algorithms, K/L and METIS produced the most uniformly sized groups (Figure ??C) and also had significantly lower losses compared to the spectral bisection algorithm (Figure ??B). K/L and METIS solutions were very similar, with their respective best solutions (lowest loss) having an average Jaccard similarity index of 0.91 on the diagonal (Figure ??D,E). K/L and METIS solutions were also consistent across pairwise random initiations, both when comparing within K/L or METIS solutions (Rand Index=0.87 and 0.91, respectively) and when comparing all pairwise K/L and METIS solutions (Rand Index=0.88) (Figure ??F). Overall, these results indicate the importance of non-redundant gene-pathway groupings to interpret biological effects. They also indicate that for some gene-pathway graphs, such as the one in this study, graph partitioning is a better approach than clustering.

1404 **Molecular Dynamics Simulations Results**

1405 **RMSD analysis of Ala1527 vs Gly1527 in open and closed states.** To evaluate
1406 conformational stability, we conducted root mean square deviation (RMSD) analyses on
1407 ABCA7 under different states and mutations (Figure ??G,H; Figure ??A,B; Table ??).
1408 RMSD values for the C_α atoms were calculated over the course of a 300 ns simulation
1409 period, comparing closed and open conformations, each harboring either the G1527 or A1527
1410 mutation.

1411 For the open ABCA7 conformation, both the G1527 and A1527 mutants exhibited relatively
1412 minor RMSD fluctuations (Figure ??A-D), with RMSD values for the A1527 mutant signifi-
1413 cantly lower compared to those of the G1527 mutant (Figure ??E). Overall, both mutants
1414 showed narrow RMSD distributions in the open state (Figure ??C, D), indicating generally
1415 stable conformational behavior.

1416 Differences in RMSD distributions between the two variants became more pronounced in
1417 the closed state: The RMSD profile of the closed conformation with the G1527 mutation
1418 exhibited substantial fluctuations throughout the simulation (Figure ??I), suggesting that
1419 the G1527 mutation significantly increases local structural flexibility. In contrast, the
1420 closed conformation harboring the A1527 mutation showed only minor RMSD fluctuations
1421 (Figure ??I), suggesting that the A1527 mutation confers greater structural stability and
1422 reduced flexibility in the closed ABCA7 conformation. Principal component analysis (PCA)
1423 further highlighted these differences visually; For the closed conformation, PCA projections
1424 of G1527 conformations over time were broad, indicating significant exploration of the
1425 conformational space (Figure ??J). Conversely, the PCA plot for the closed A1527 mutant
1426 displayed a tightly clustered distribution (Figure ??J), indicating limited conformational
1427 sampling over time and suggesting decreased conformational flexibility induced by the A1527
1428 mutation.

1429 **Dihedral angle analysis of Ala1527 vs Gly1527 in open and closed states.** To
1430 further explore the local structural variations induced by a p.Ala1527Gly mutation, we
1431 analyzed backbone dihedral angles (phi/psi; ϕ/ψ) for residues 1517-1537. In the open
1432 conformation, Gly1527 consistently occupied the α -helical region of the Ramachandran plot
1433 throughout the simulation. In contrast, Ala1527 showed two distinct populations within the
1434 α -helical region (Figure ??A), suggesting subtle local conformational differences, yet overall
1435 preservation of the α -helical structure. These findings align closely with the RMSD analysis,
1436 and suggest similar conformational behaviors between the variants in the open state.

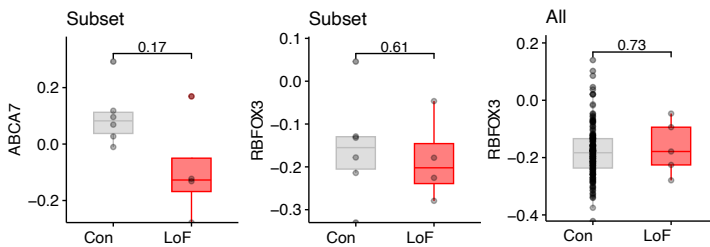
1437 However, significant structural differences emerged in the closed conformation: Ala1527
1438 displayed two preferred conformations—one within the α -helical region and another shifted
1439 toward the β -structure region—while Gly1527 explored a broader range of dihedral angles,
1440 indicative of greater structural flexibility (Figure ??A,B). This observation is in line with the
1441 RMSD analysis, indicating structural differences specifically in the closed state, with Gly1527
1442 exhibiting significantly greater conformational flexibility compared to Ala1527.

1443 **Secondary structure analysis of Ala1527 vs Gly1527 in open and closed states.**
1444 To complement backbone angle analysis, we also evaluated secondary structure stability
1445 throughout the simulation. In the open state, secondary structure content was comparable
1446 between variants, maintaining similar α -helical character (Figure ??C). Upon transitioning
1447 to the closed state, both variants experienced a substantial loss of α -helical content across
1448 residues 1517-1537. This loss, however, was more pronounced in the Gly1527 variant compared
1449 to the Ala1527 variant, as residues 1520-1525 retained partial α -helical structure more robustly
1450 in the Ala1527 variant compared to Gly1527 (Figure ??C).

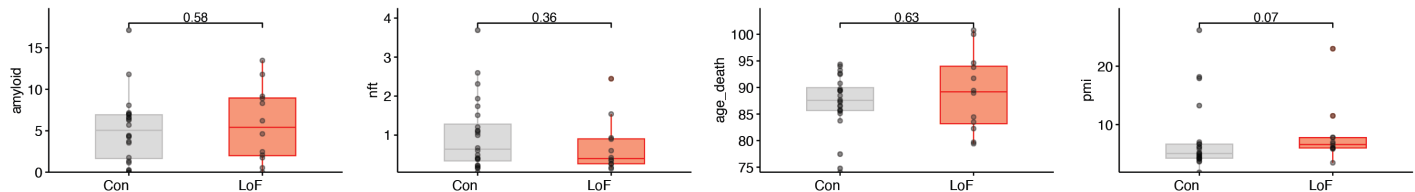
1451 Finally, structural alignment of the closed-state Gly1527 ABCA7 structure (PDB 8EOP) with
1452 the closed-state structures of ABCA1 (PDB 7TBW) and ABCA4 (PDB 7LKZ) revealed that
1453 residues corresponding to Gly1527 in ABCA7 (V1646 in ABCA1; I1671 in ABCA4) adopt
1454 stable α -helical structures (Figure ??E,F). In contrast, the Gly1527 residue in ABCA7 exhibits
1455 significant flexibility and lacks defined α -helical structure. Interestingly, our simulations
1456 indicate that the Ala1527 variant partially restores this local α -helical conformation in ABCA7
1457 (Figure ??C,D). These data suggest that the Gly1527 variant induces local structural changes
1458 that differentiate ABCA7 from its close homologs ABCA1 and ABCA4.

Supplementary Figures

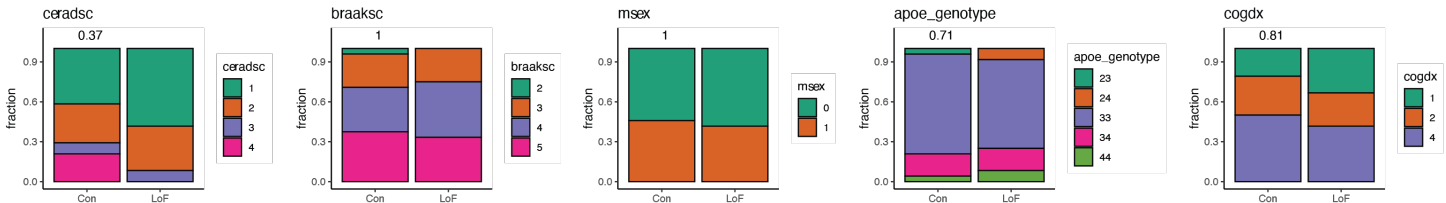
A



B



C



D

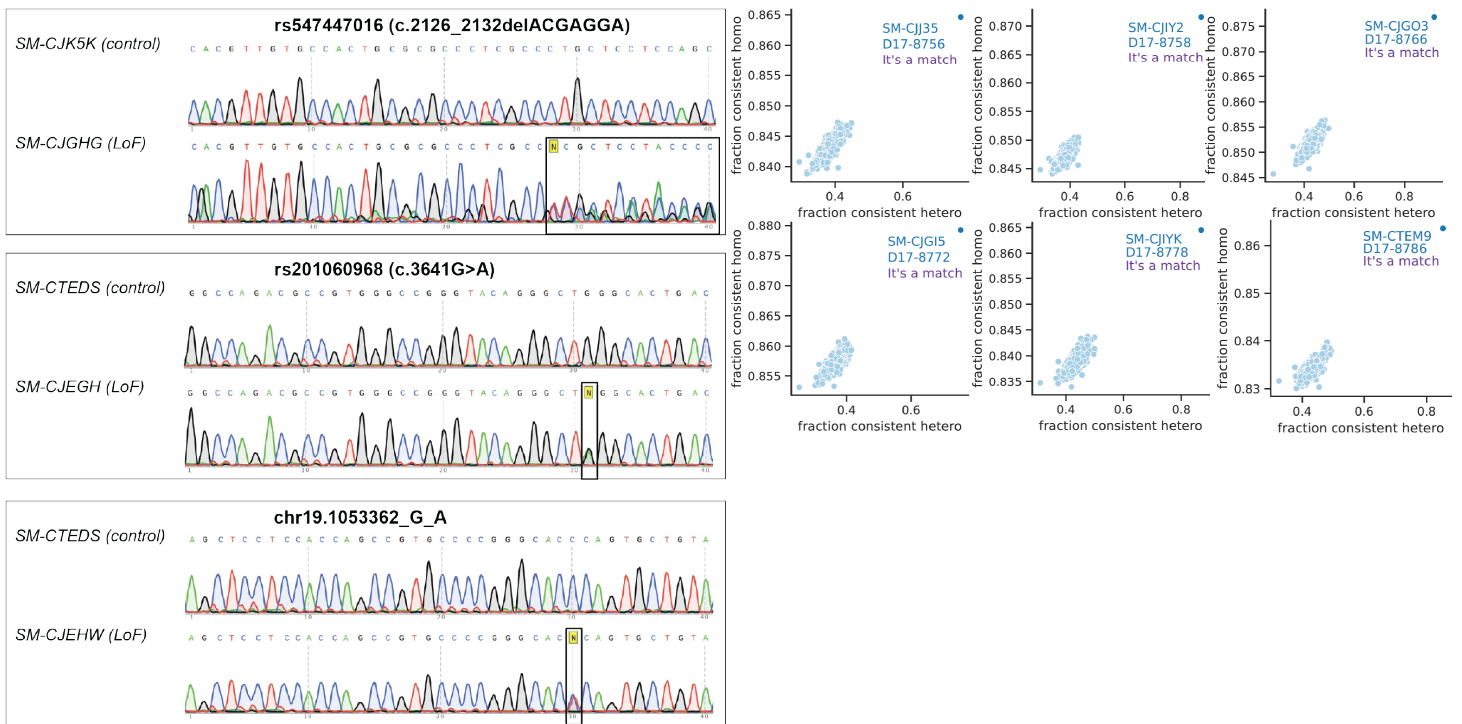
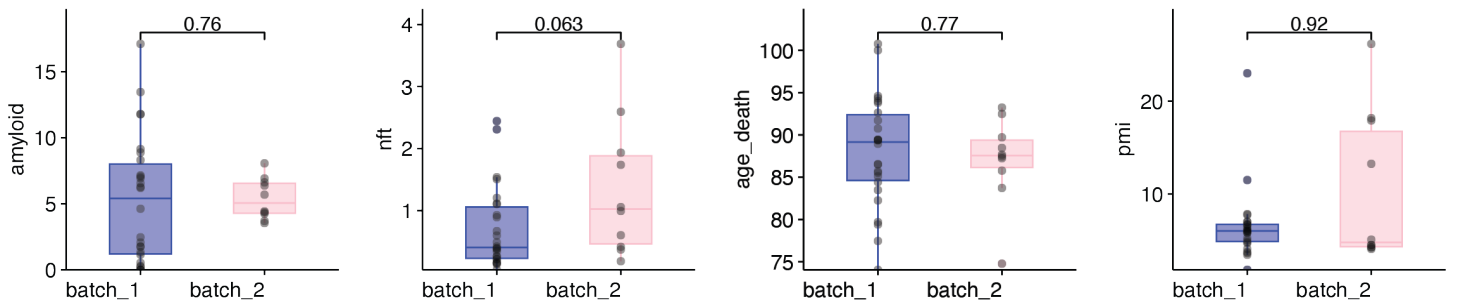


Figure S1: Overview of Human snRNA-Sequencing Cohort.

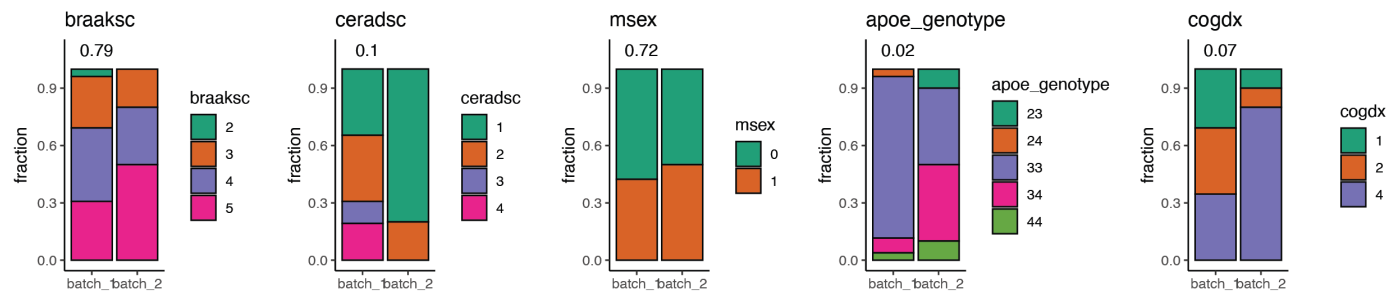
- (A) Protein levels from post-mortem human prefrontal cortex (see Table ?? for external dataset used) showing ABCA7 protein levels (left) and Neun (RBFOX3) levels (middle) for a subset of individuals found to overlap with the snRNA-seq cohort ($N=6$ control and $N=4$ ABCA7 LoF carriers). The right panel shows Neun (RBFOX3) protein levels by genotype in all available control samples ($N=180$) vs. all available ABCA7 LoF carriers with proteomic data ($N=5$).

- (B) Distributions of continuous metadata variables (see Supplementary Text for descriptions) for control individuals (N=24) vs. ABCA7 LoF carriers (N=12). For panels C and D, boxes indicate dataset quartiles per condition, and whiskers extend to the most extreme data points not considered outliers (i.e., within 1.5 times the interquartile range from the first or third quartile).
- (C) Distributions of discrete metadata variables for control individuals (N=24) vs. ABCA7 LoF carriers (N=12). Con=control, LoF=ABCA7 loss-of-function. P-values in panels A and B were computed by two-sided Wilcoxon rank sum test. P-values in panel C were computed by two-sided Fisher's exact test.
- (D) Sanger sequencing of ABCA7 LoF variants in prefrontal cortex genomic DNA samples from 3 ABCA7 LoF carriers and 3 controls from the snRNA-seq cohort. Sequencing confirmed heterozygosity of the indicated variant in LoF samples, with variant location marked by a black box.
- (E) Example plots validating matches between whole genome sequencing (WGS) and snRNA-seq libraries. Each plot shows the concordance of homo- and heterozygous SNP calls between WGS and snRNA-seq data for a single individual. Matches between WGS SNP calls and snRNA-seq BAM inferred SNP calls are indicated by extreme outliers. Expected (i.e., correct) matches are indicated in blue/purple.

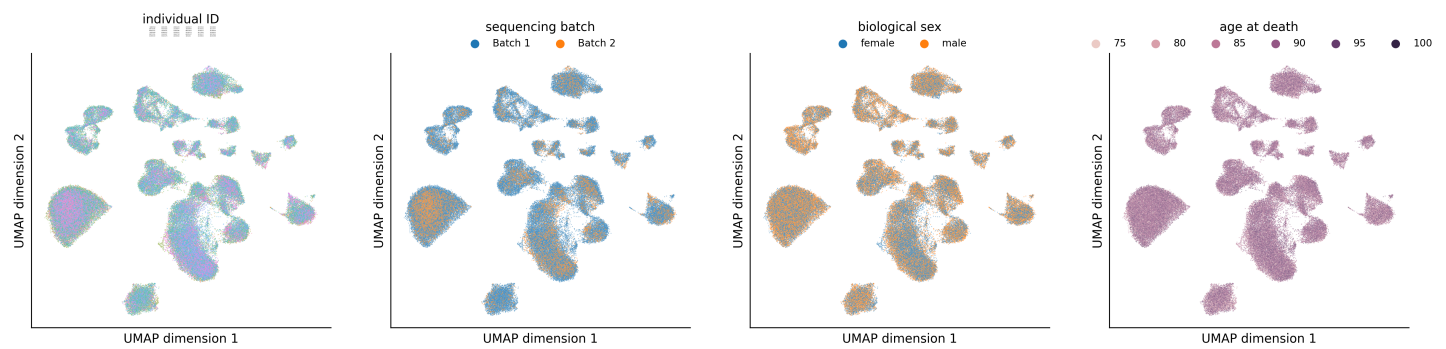
A



B



C



D

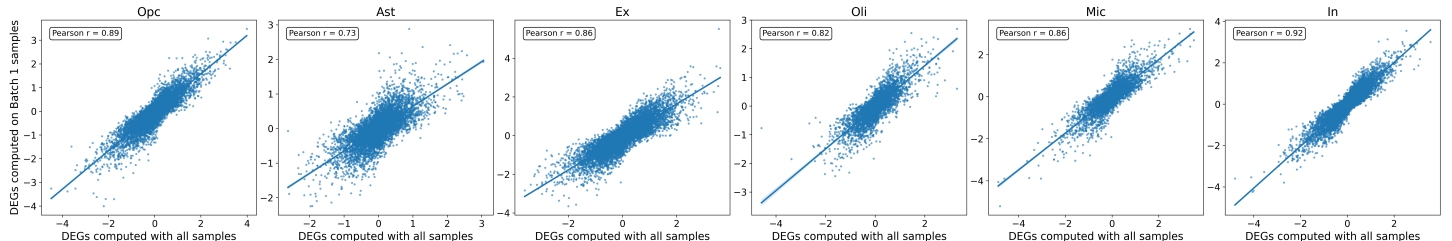


Figure S2: Overview of snRNA-seq Batch Correction and Data Quality.

- (A) Distribution of continuous metadata variables by sequencing batch. P-values in panels were computed by two-sided Wilcoxon rank sum test.
- (B) Distribution of discrete metadata variables by sequencing batch. P-values were computed by two-sided Fisher's exact test.
- (C) 2D UMAP projection of snRNA-seq cells after quality control, colored by selected metadata variables.
- (D) Correlation of gene perturbation scores ($S = -\log_{10}(p) \times \text{sign}(\log_2(\text{fold-change}))$) computed using

all samples versus excluding batch 2 (v2 chemistry), demonstrating that results are robust and not driven by batch-specific effects.

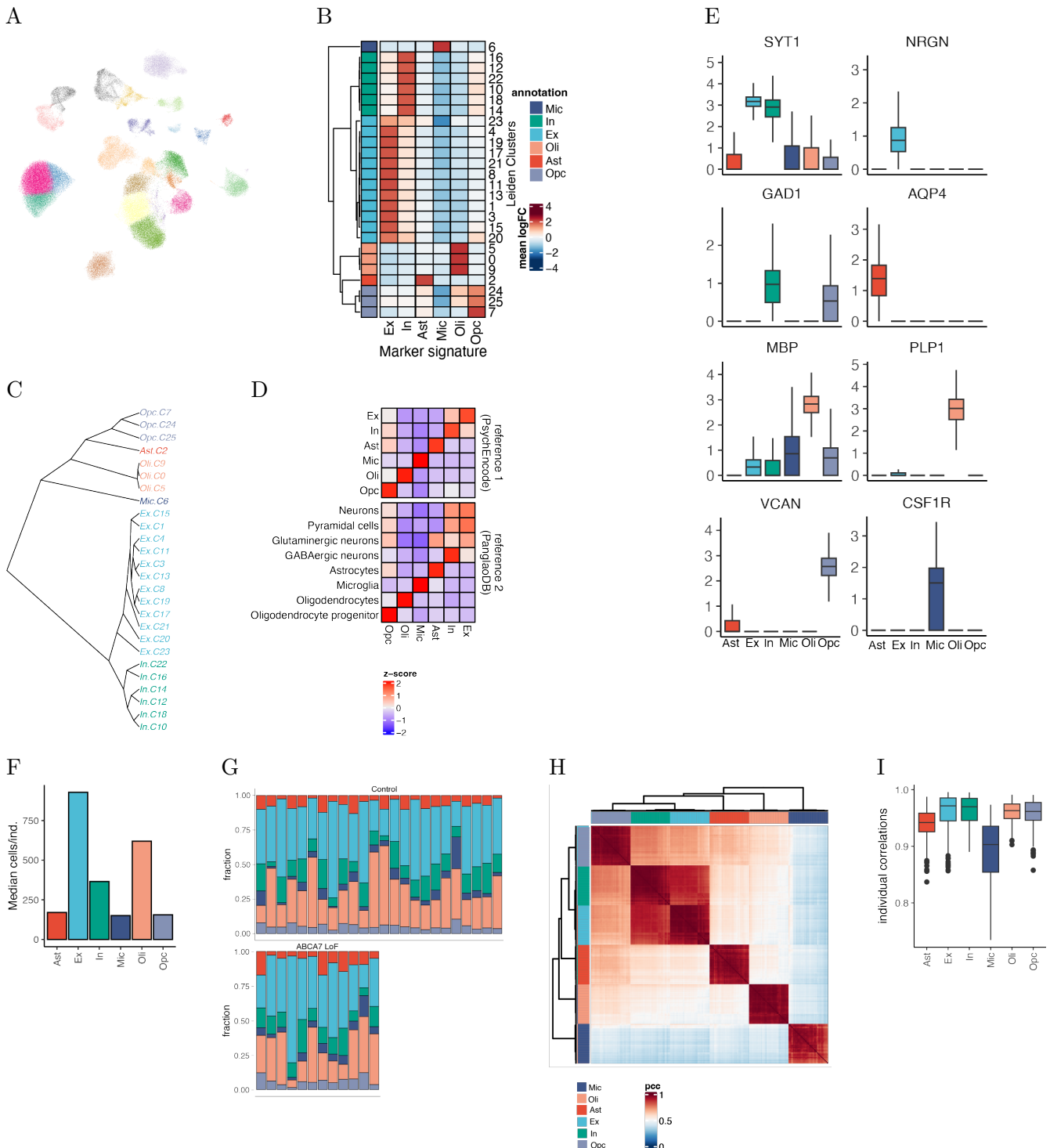


Figure S3: Overview of snRNA-seq Cell Type Annotations.

- (A) Two-dimensional UMAP projections of individual cells from gene expression space, colored by Leiden clusters.
- (B) Average marker gene expression (per-cluster mean log(fold-change)) for all marker genes for the cell type indicated along the x-axis. Log(fold-changes) are computed for the cluster of interest vs. all remaining clusters. Reference 1 (Table ??) marker genes were used.
- (C) Cladogram visualizing subcluster relationships based on pairwise distances between per-cluster gene expression profiles.

- (D) Average marker gene expression profiles (x-axis) per major cell type annotation (y-axis) for two marker gene references (Table ??).
- (E) Per-cell distribution of select marker gene expression by cell type. Y-axis indicates log-counts.
- (F) Median number of cells per cell type per individual.
- (G) Cell type fraction by individual.
- (H) Heatmap of individual-level gene expression correlations by cell type.
- (I) Boxplot of individual-level gene expression correlations by cell type.

A

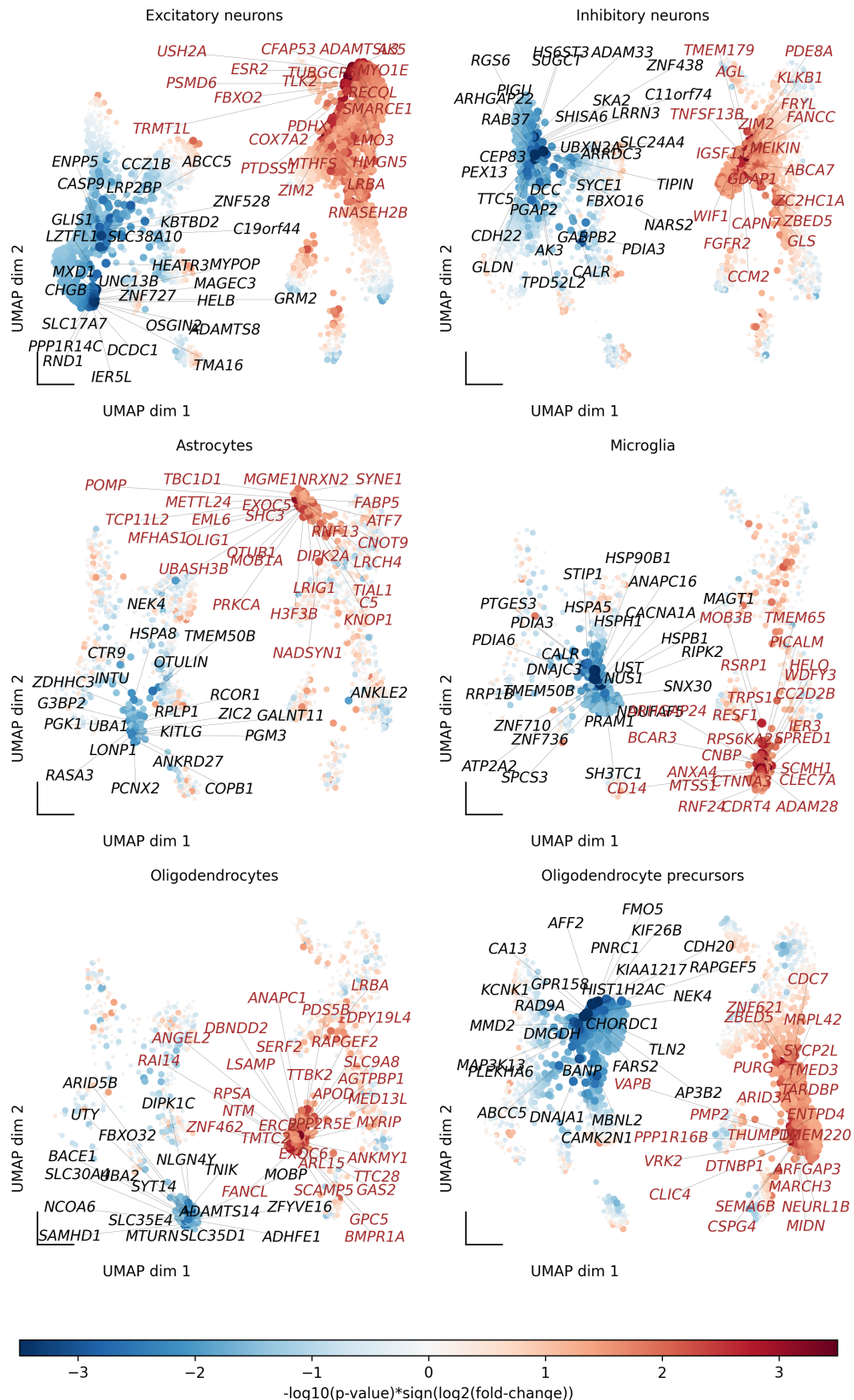
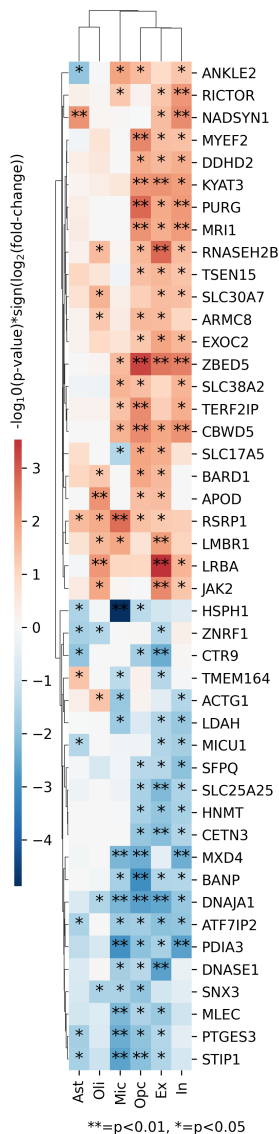


Figure S4: Annotated Projections of Gene Scores.

(A) Enlarged view of the UMAP projection of Figure ??E, showing the top 20 genes by absolute score ($|S|$) for each cell type.

A



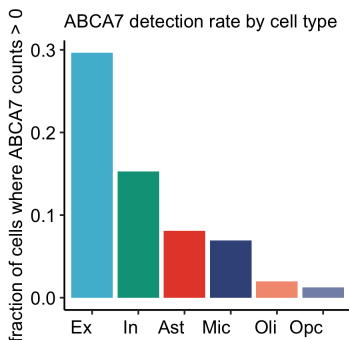
B

Gene	Summary
ANKLE2	ankyrin repeat and LEM domain containing 2
RICTOR	RPTOR independent companion of MTOR complex 2
NADSYN1	NAD synthetase 1
DDHD2	DDHD domain containing 2
KYAT3	kynurenine aminotransferase 3
PURG	purine rich element binding protein G
MRI1	methylthioribose-1-phosphate isomerase 1
RNASEH2B	ribonuclease H2 subunit B
TSEN15	tRNA splicing endonuclease subunit 15
SLC30A7	solute carrier family 30 member 7
ARMC8	armadillo repeat containing 8
EXOC2	exocyst complex component 2
ZBED5	zinc finger BED-type containing 5
SLC38A2	solute carrier family 38 member 2
TERF2IP	TERF2 interacting protein
CBWD5	nan
SLC17A5	solute carrier family 17 member 5
BARD1	BRCA1 associated RING domain 1
APOD	apolipoprotein D
RSRP1	arginine and serine rich protein 1
LMBR1	limb development membrane protein 1
LRBA	LPS responsive beige-like anchor protein
JAK2	Janus kinase 2
HSPH1	heat shock protein family H (Hsp110) member 1
ZNRF1	zinc and ring finger 1
CTR9	CTR9 homolog, Paf1/RNA polymerase II complex component
TMEM164	transmembrane protein 164
ACTG1	actin gamma 1
LDAH	lipid droplet associated hydrolase
MICU1	mitochondrial calcium uptake 1
SFPQ	splicing factor proline and glutamine rich
SLC25A25	solute carrier family 25 member 25
HNMT	histamine N-methyltransferase
CETN3	centrin 3
MXD4	MAX dimerization protein 4
BANP	BTG3 associated nuclear protein
DNAJA1	DnaJ heat shock protein family (Hsp40) member A1
ATF7IP2	activating transcription factor 7 interacting protein 2
PDIA3	protein disulfide isomerase family A member 3
DNASE1	deoxyribonuclease 1
SNX3	sorting nexin 3
MLEC	malectin
PTGES3	prostaglandin E synthase 3
STIP1	stress induced phosphoprotein 1

Figure S5: Shared Differentially Expressed Genes by Cell Type.

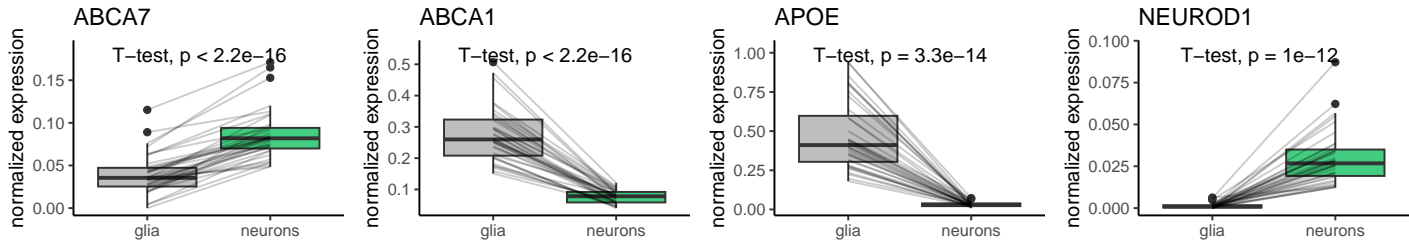
- (A) Heatmap indicating the overlap of differentially expressed genes between cell types (genes, where p-value < 0.05 in at least three cell types).
- (B) Functional annotations of genes in the same order as in the heatmap in A.

A



B

this scRNA-seq dataset



C

Welch et al. Bulk RNA-Seq Expression by FAC-sorting

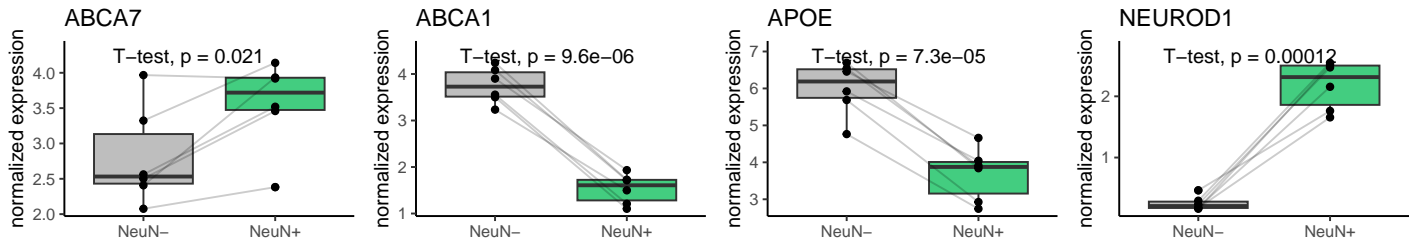
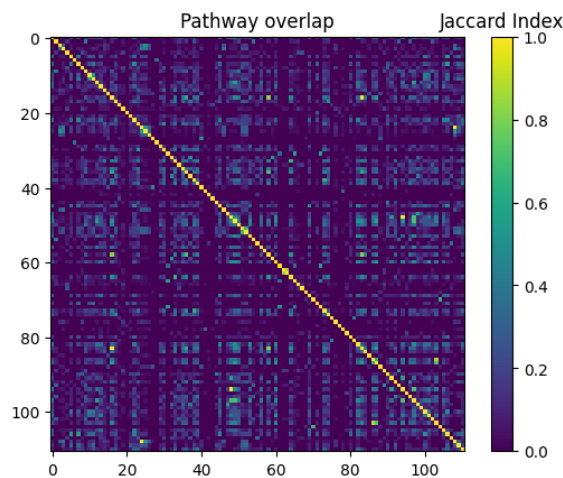


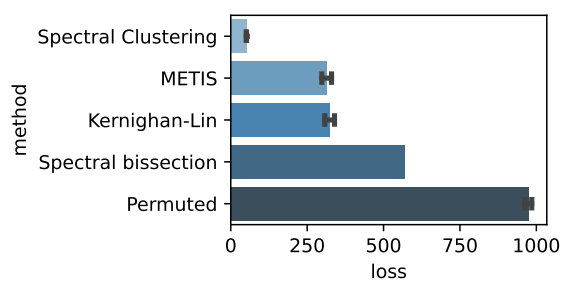
Figure S6: Neuronal Expression of ABCA7 in the Postmortem Human Brain.

- (A) Per cell type ABCA7 detection rate of major cell types in the *postmortem* PFC as quantified by snRNA-seq.
- (B) Normalized expression of indicated gene in glial cells (per-individual mean expression profiles across Oli, Opc, Ast, Mic) vs. neuronal cells (per-individual mean expression profiles across Ex and In) from *postmortem* snRNA-seq data.
- (C) Normalized expression of indicated genes in NeuN- vs. NeuN+ cells ($N=6$ individuals, from [51]; Table ??). All p-values are computed by paired two-sided t-test. Boxes indicate per-condition dataset quartiles, and whiskers extend to the most extreme data points not considered outliers (i.e., within 1.5 times the interquartile range from the first or third quartile).

A

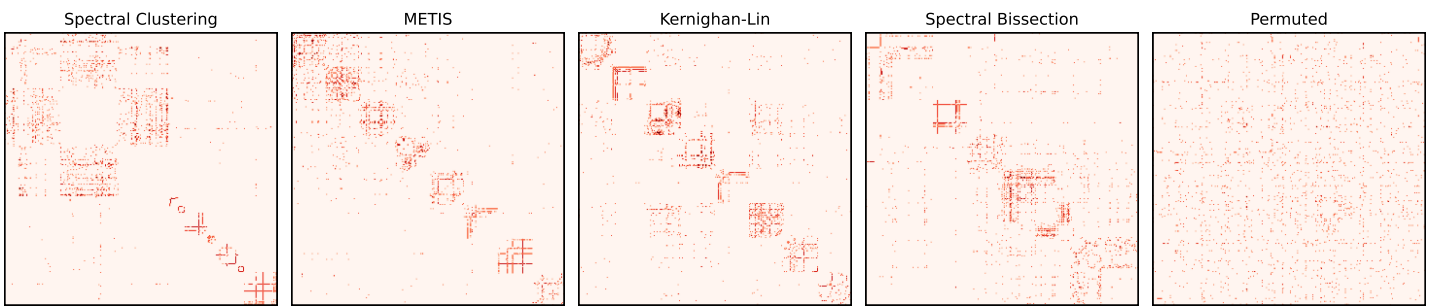


B

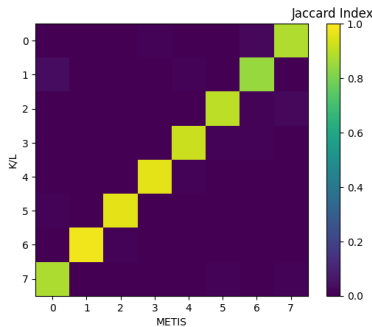


C

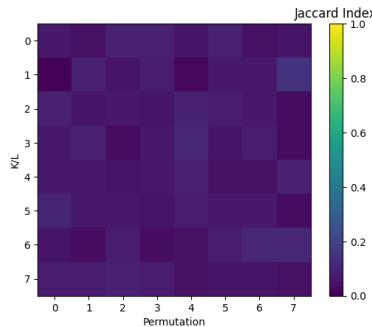
Adjacency matrices ordered by cluster labels



D



E



F

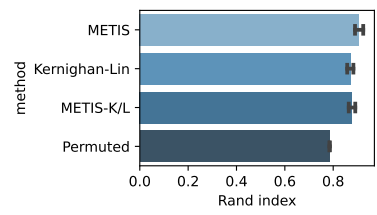


Figure S7: Benchmarking Partitioning and Clustering Algorithms for Gene-Pathway Grouping.

- (A) Jaccard indices quantifying overlap of genes for all 111 pathways in Figure ??B (see Methods; Supplementary Text). Consistency is quantified using the Jaccard Index (JI). $JI = \frac{|A \cap B|}{|A \cup B|}$, where A and B are two sets (i.e., cluster A from initiation #1 and cluster B from initiation #2).
- (B) Average loss (total cut size; see Methods) associated with applying each algorithm (spectral clustering (SC), METIS, Kernighan-Lin (K/L), spectral bisection (SB), or random permutation) on the graph G (with 379 vertices; see Methods) over 1000 initiations (SC, random permutation) or 5×10^5 initiations (METIS, K/L). The SB implementation is deterministic and was run only once. Error bars indicate the standard deviation.
- (C) Unweighted adjacency matrix for G sorted by labels assigned by the indicated algorithm. Red indicates the presence of an edge between two vertices. For each algorithm, labels corresponding to the best

initiation (lowest loss) over 1000 initiations (SC, random permutation) or 5×10^5 initiations (METIS, K/L) are shown.

- (D) Pairwise labeling consistency for the best K/L initiation and the best METIS initiation. Cluster labels corresponding to each are shown on the X- and Y-axes, respectively. Each color entry indicates the fraction of shared vertices per cluster across two initiations.
- (E) Same as (D), but comparing the best K/L initiation against the best random permutation initiation.
- (F) Average Rand index (RI) for all pairwise initiations from (B). “METIS,” “Kernighan-Lin,” and “Permuted” labels on the Y-axis indicate the average RI (consistency across two sets of labels) for all combinations of initiations within the specified algorithm. “METIS-K/L” indicates the average RI for all combinations of initiations across the METIS and Kernighan-Lin algorithms. Error bars indicate standard deviations. ($RI = \frac{\text{number of agreeing vertex pairs}}{\text{number of vertex pairs}}$).

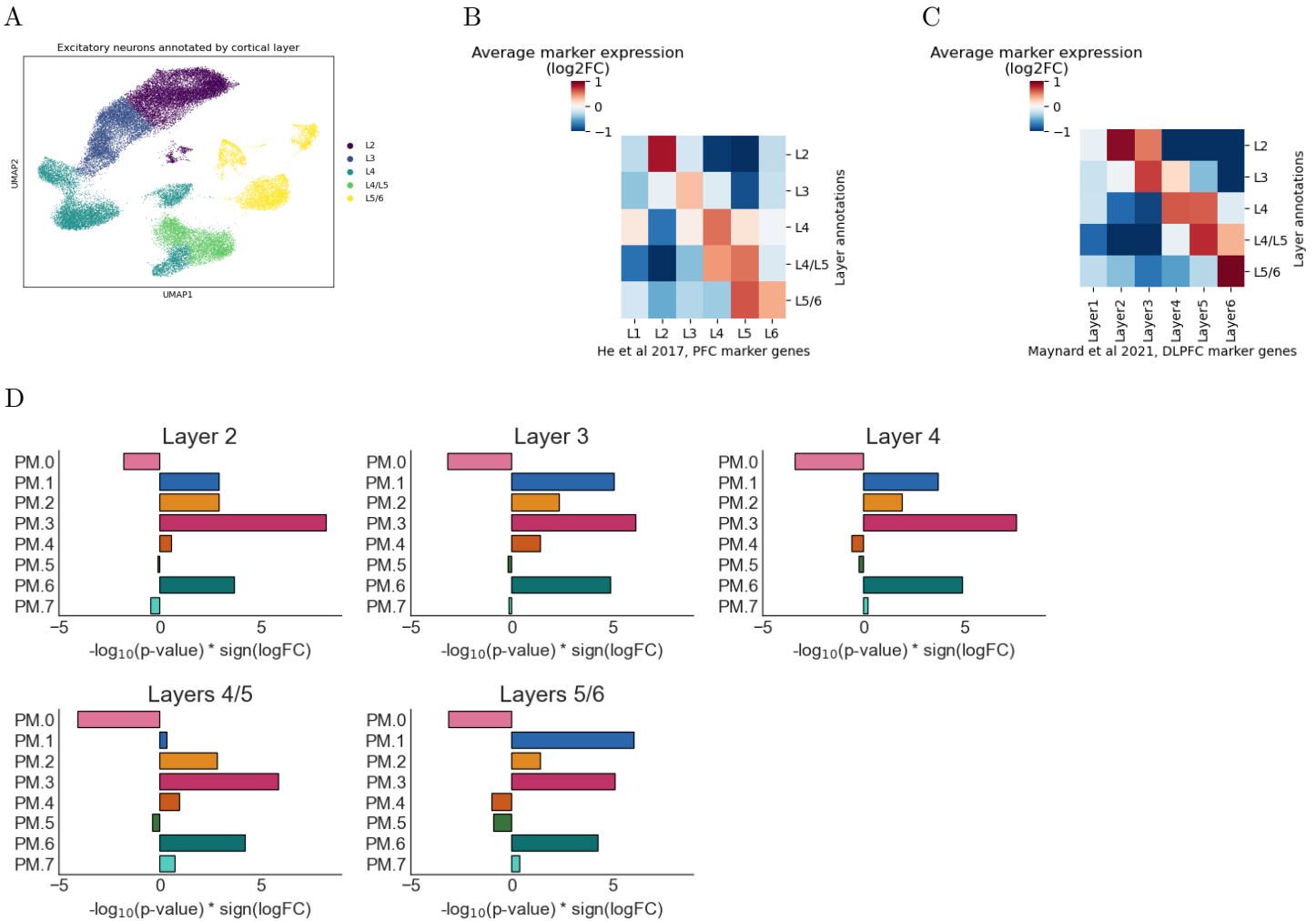


Figure S8: Annotation of Excitatory Neurons from *postmortem* snRNAseq Dataset by Cortical Layer.

- (A) UMAP visualization of excitatory neurons annotated by cortical layers based on Leiden clustering.
 - (B) Heatmap showing enrichment of cortical layer-specific marker genes from [126] across annotated layers. Color indicates average marker gene expression (log₂ fold change) for each layer marker gene set with respect to all other clusters.
 - (C) Heatmap displaying validation of layer annotations using an independent set of cortical layer marker genes from [127]. Color represents average marker gene expression (log₂ fold change) for each layer marker gene set with respect to all other clusters.
 - (D) ABCA7 LoF-associated perturbations of excitatory neuronal PM gene clusters by layer (computed by FGSEA, see Methods).

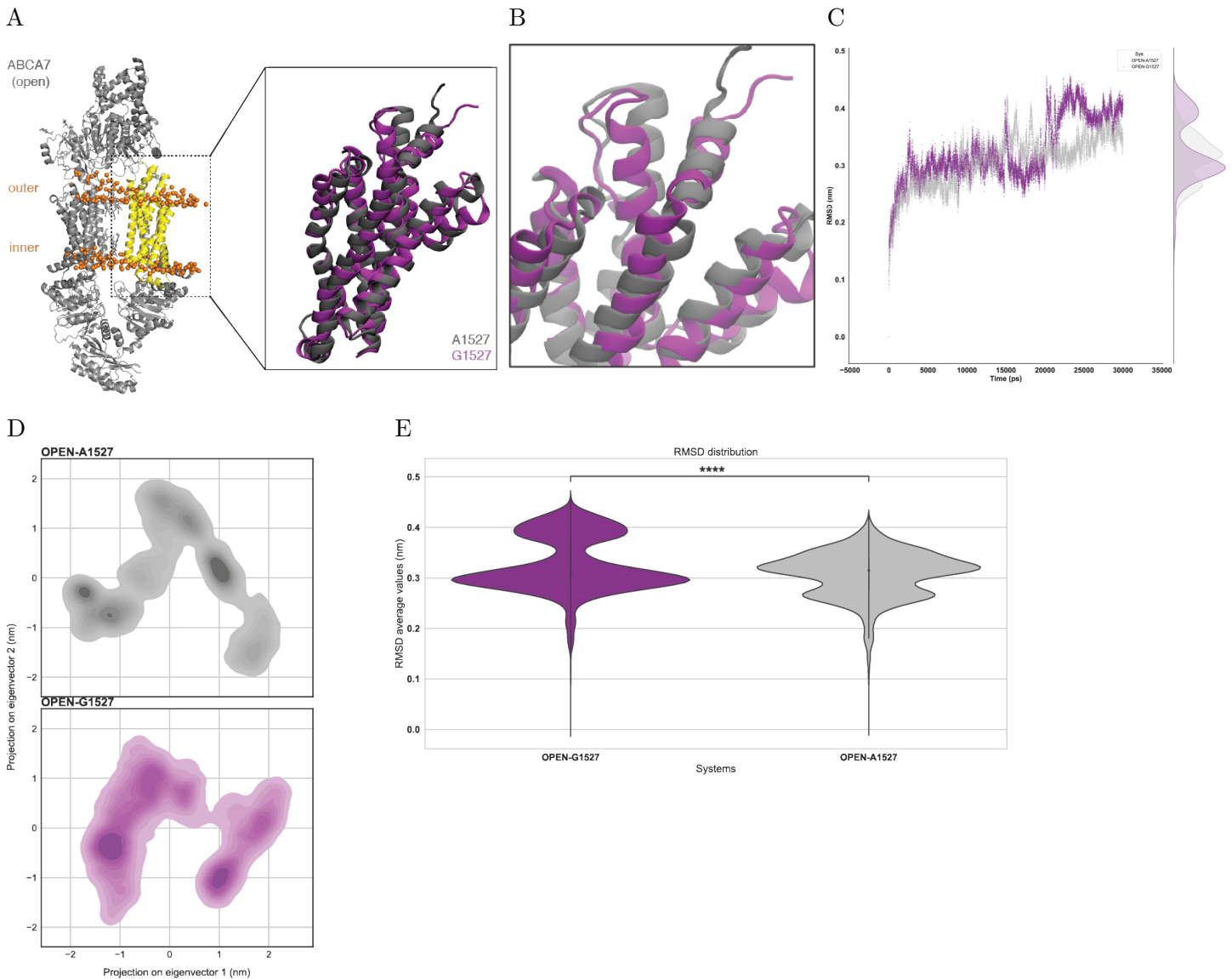
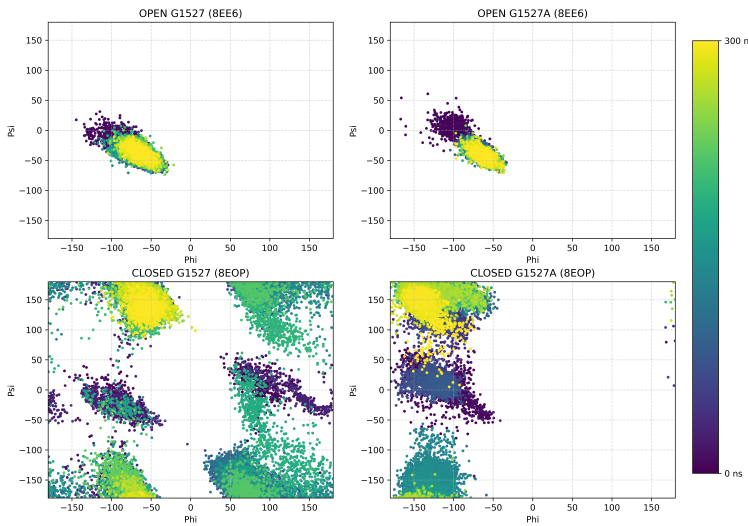


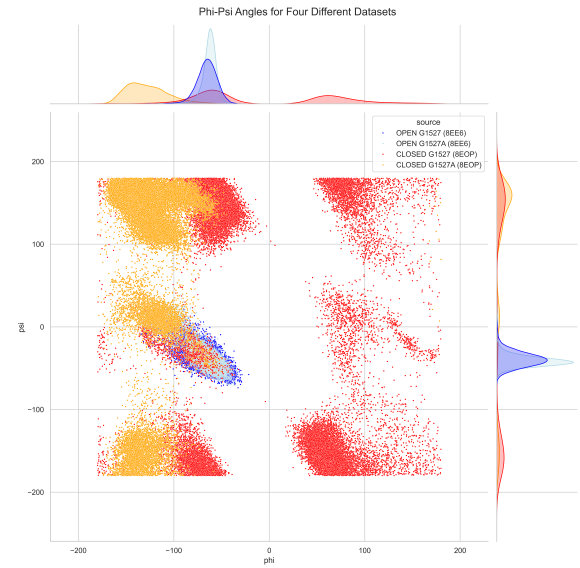
Figure S9: Molecular Dynamics Simulations of ABCA7 Open Conformations with p.Ala1527Gly Substitution.

- (A) Open conformation ABCA7 protein structure. ABCA7 domain between residues 1517 and 1756 used for simulations is shown in yellow. Expanded yellow domain (inset from left), with A1527 variant (light grey) and G1527 variant (purple).
- (B) Expanded inset from A.
- (C) Root mean squared deviations of open conformation domains from B with A1527 (light grey) or G1527 (purple) under simulation. Structural deviations over time were computed with respect to reference open structures from B.
- (D) Projection of C_{α} atom positional fluctuations under simulation onto the first two principal components, for open conformation domain from B with A1527 (top, light grey) or G1527 (bottom, purple).
- (E) Violin plot indicating average C_{α} atom positional fluctuations over time.

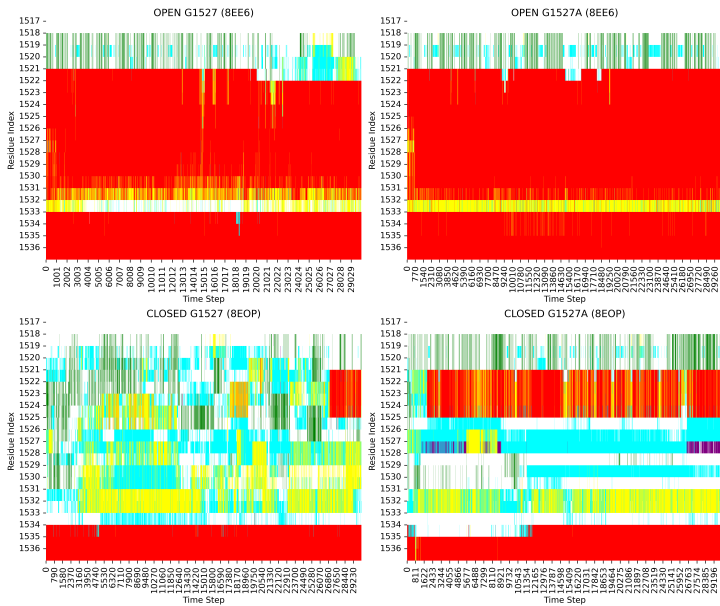
A



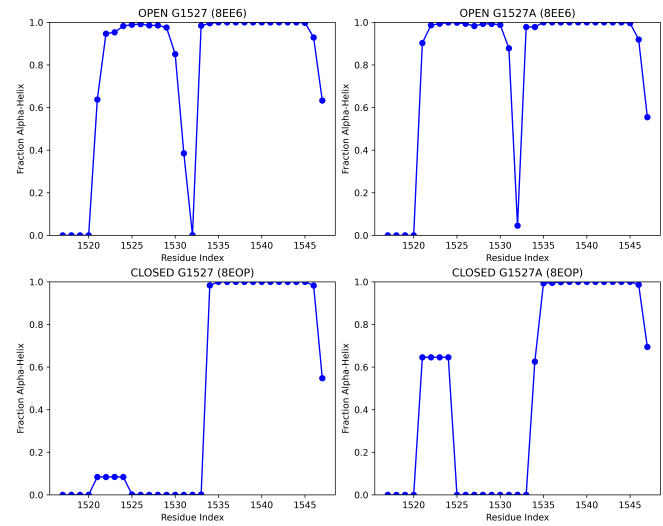
B



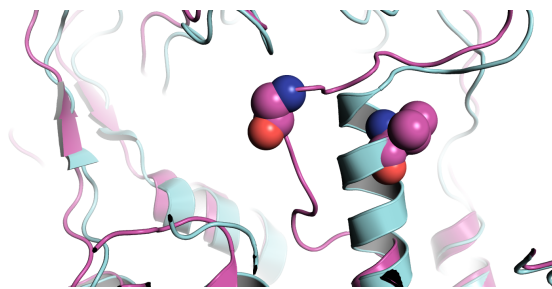
C



D



E



F

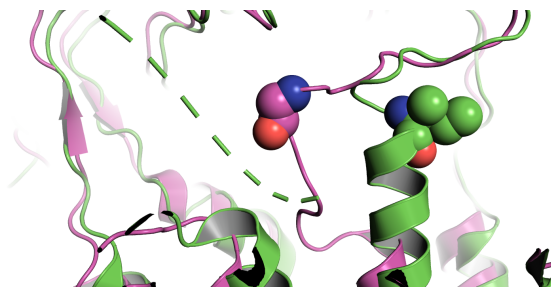
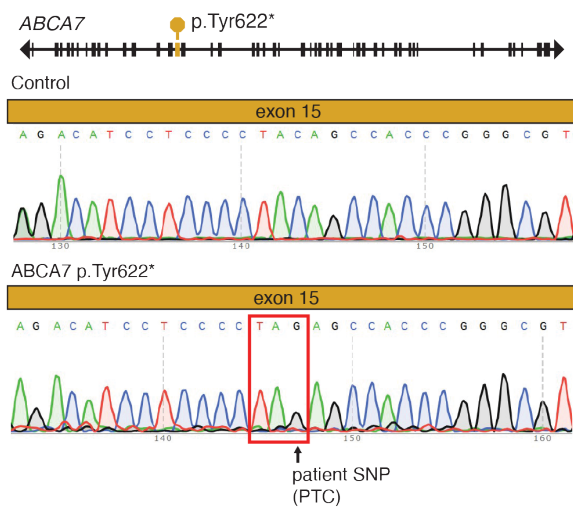


Figure S10: Analysis of Local Conformational Fluctuations and Secondary Structure Variations Induced by the p.Ala1527Gly Substitution in ABCA7 Open and Closed Conformations.

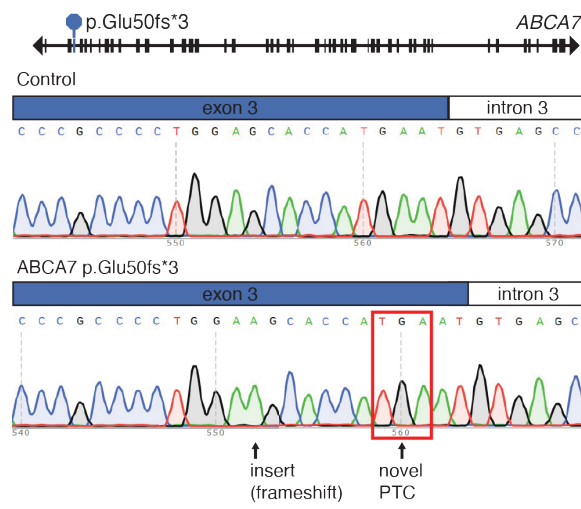
(A) Phi vs. Psi dihedral angle distribution of residue 1527 as a function of simulation time for open and closed conformations.

- (B) Overall Phi vs. Psi dihedral angle distributions for residue 1527, comparing open and closed conformations throughout the entire simulation period.
- (C) Time-resolved secondary structure assignments for residues 1517–1537. Alpha-helical structures are highlighted in red; other colors represent distinct secondary structures.
- (D) Fraction of alpha-helical content observed for residues 1517–1537 during the simulations. A value of 1 indicates uninterrupted preservation of the alpha-helical structure throughout the simulation duration.
- (E) ABCA1 (cyan) closed structure; PDB ID: 7TBW. ABCA7 (purple) closed structure; PDB ID: 8EOP. Positions of Gly1527 in ABCA7 and V1646 in ABCA1 are indicated as spheres.
- (F) ABCA4 (green) closed structure; PDB ID: 7LKZ. ABCA7 (purple) closed structure; PDB ID: 8EOP. Positions of Gly1527 in ABCA7 and I1671 in ABCA4 are indicated as spheres.

A



B



C

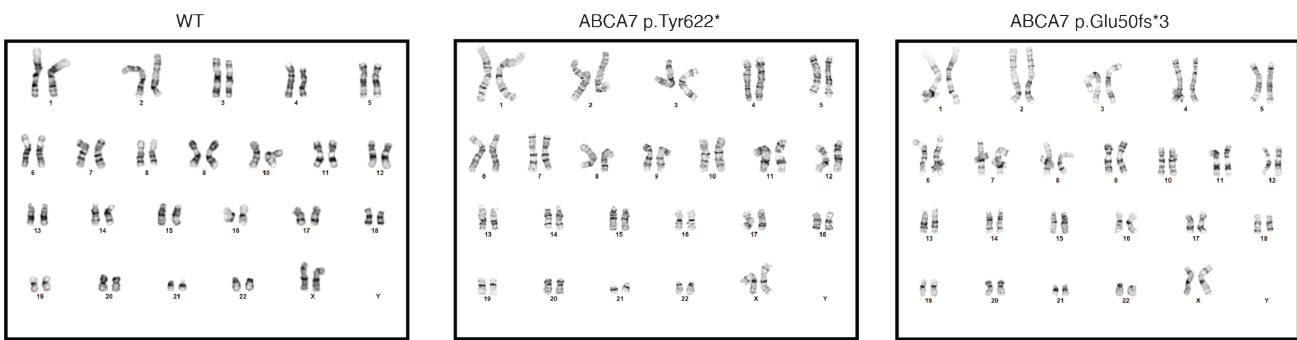
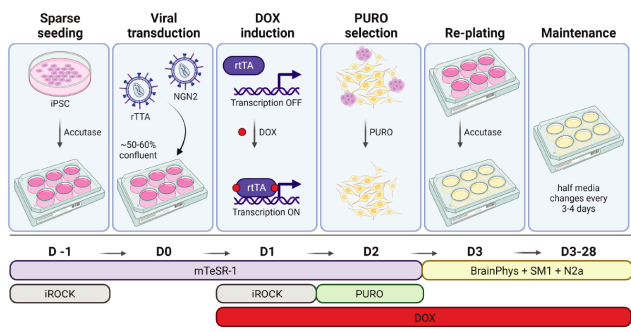


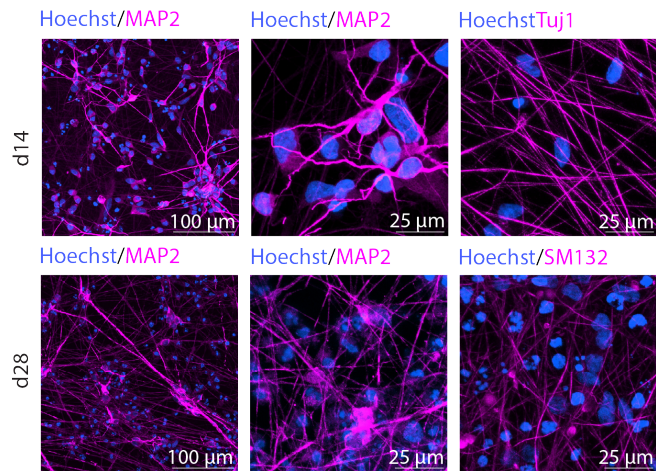
Figure S11: Generation of iPSC-Derived Cells Harboring ABCA7 PTC Variants.

- Sanger sequencing chromatogram confirming single nucleotide insertion in ABCA7 exon 3 of the ABCA7 p.Glu50fs*3 isogenic iPSC line.
- Sanger sequencing chromatogram confirming patient single nucleotide polymorphism in ABCA7 exon 15 of the ABCA7 p.Tyr622* isogenic iPSC line.
- Normal karyotypes were observed for WT, ABCA7 p.Glu50fs*3, and ABCA7 p.Tyr622* isogenic iPSC lines.

A



B



C

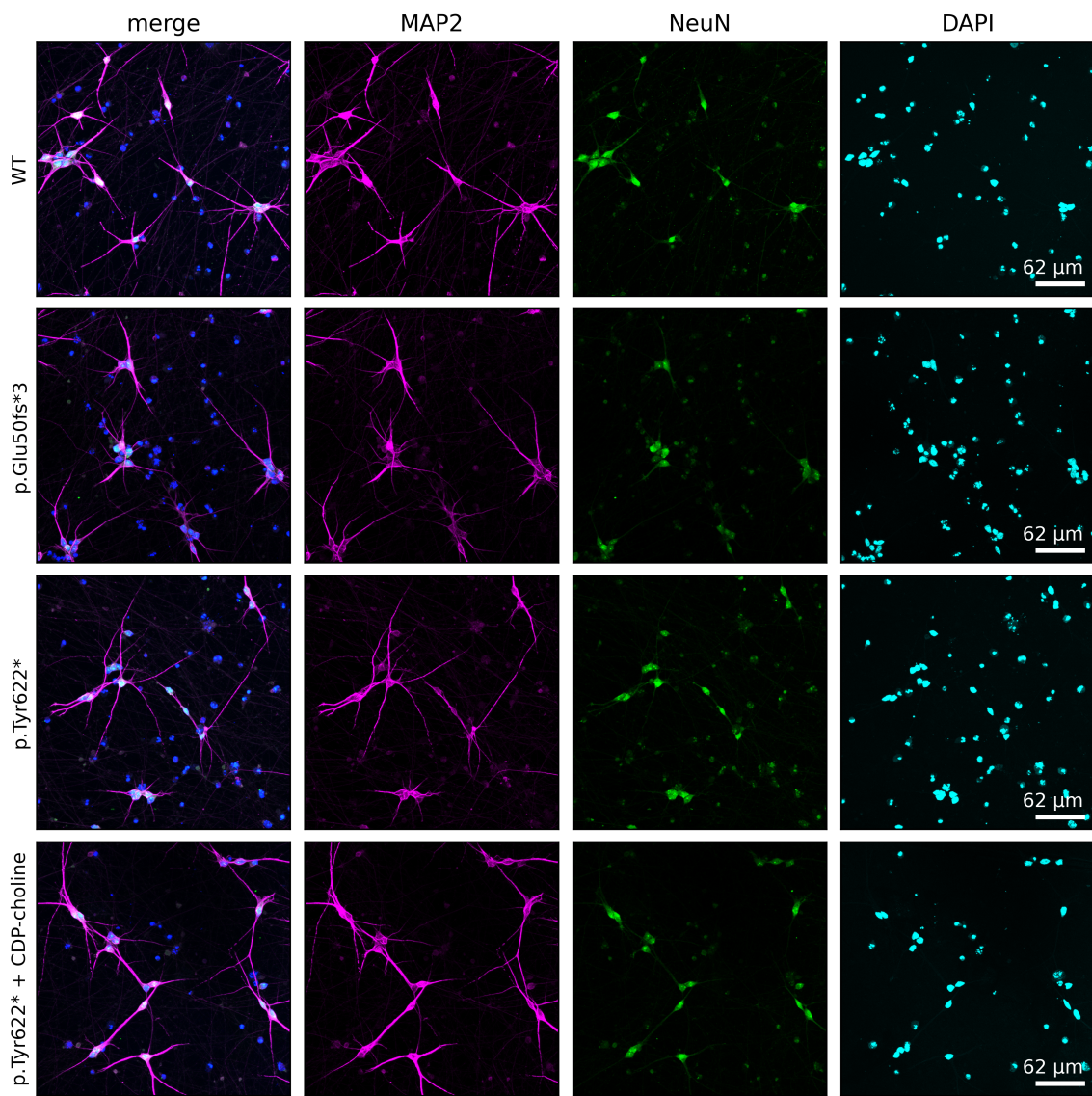


Figure S12: Differentiating iPSC-Derived Neurons Harboring ABCA7 PTC Variants.

(A) iPSCs were plated at low density for NGN2 viral transduction. Expression of NGN2 was driven by doxycycline (DOX) induction with puromycin (PURO) selection, then cells were replated to match

neuronal densities. Neurons were maintained for 4 weeks (DIV 28) before experimentation (Created with BioRender.com).

- (B) Neuronal marker expression in 2 and 4-week matured iNs.
- (C) Neuronal marker expression in iNs matured for 4 weeks for indicated genotypes. CDP-choline treatment was applied for 2 weeks at 100 μ M.

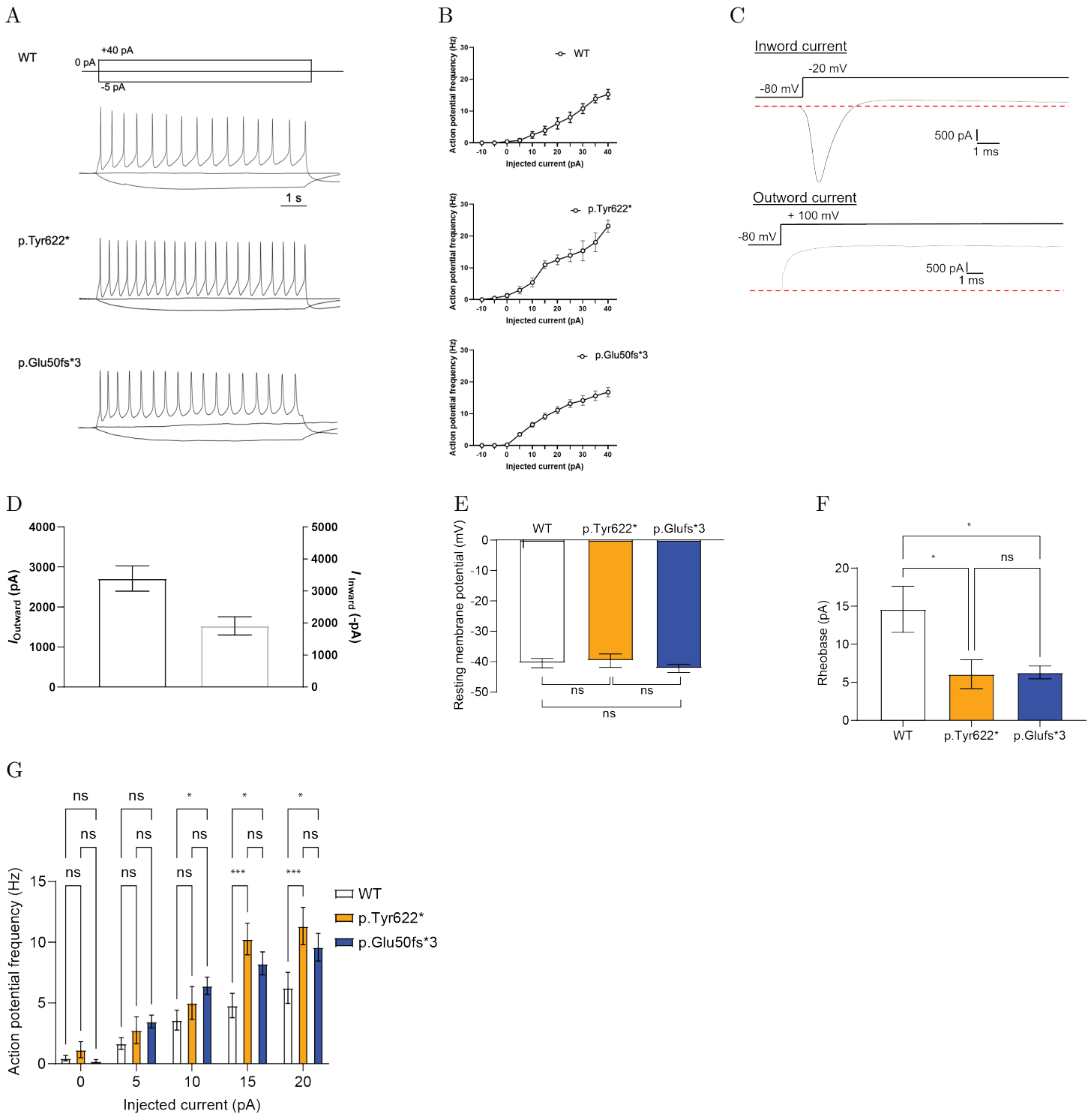
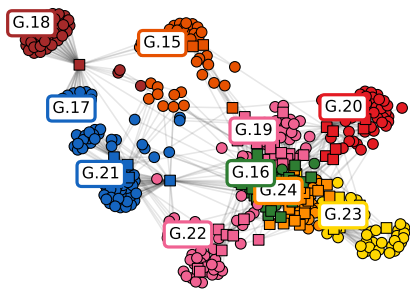


Figure S13: Measuring activity of iPSC-derived neurons harboring ABCA7 PTC variants.

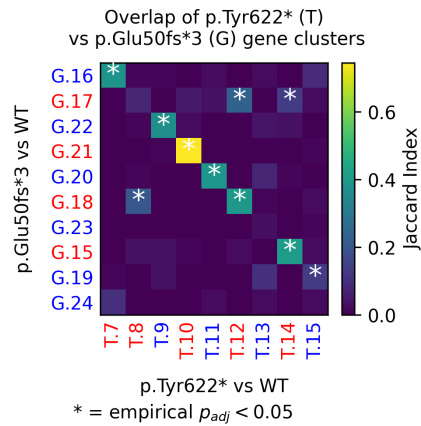
- (A) Representative sweeps show action potentials elicited by 800 ms of current injections in patched 4-week-old iNs.
- (B) Summary of action potential frequency (means \pm SEM) elicited with different amounts of injected current in 4-week-old iNs.
- (C) Representative sweeps of whole-cell current flow of inward (upper panel) and outward (lower panel) current recordings from WT 4-week-old neurons.
- (D) Quantification of (C).

- (E) Resting membrane potential (mV) of 4-week-old WT, ABCA7 p.Tyr622*, and ABCA7 p.Glufs*3 neurons.
- (F) Rheobase (pA) of 4-week-old WT, ABCA7 p.Tyr622*, and ABCA7 p.Glufs*3 neurons.
- (G) Action potential frequency of 4-week-old WT, ABCA7 p.Tyr622*, and ABCA7 p.Glufs*3 neurons with indicated current injections. For panels E-G: WT: $n = 24$; Y622: $n = 13$; G2: $n = 23$. For all panels: $P* < 0.05$, $P ** < 0.001$. Graphs are mean \pm SEM.

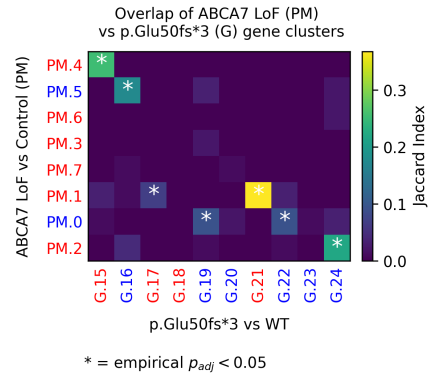
A



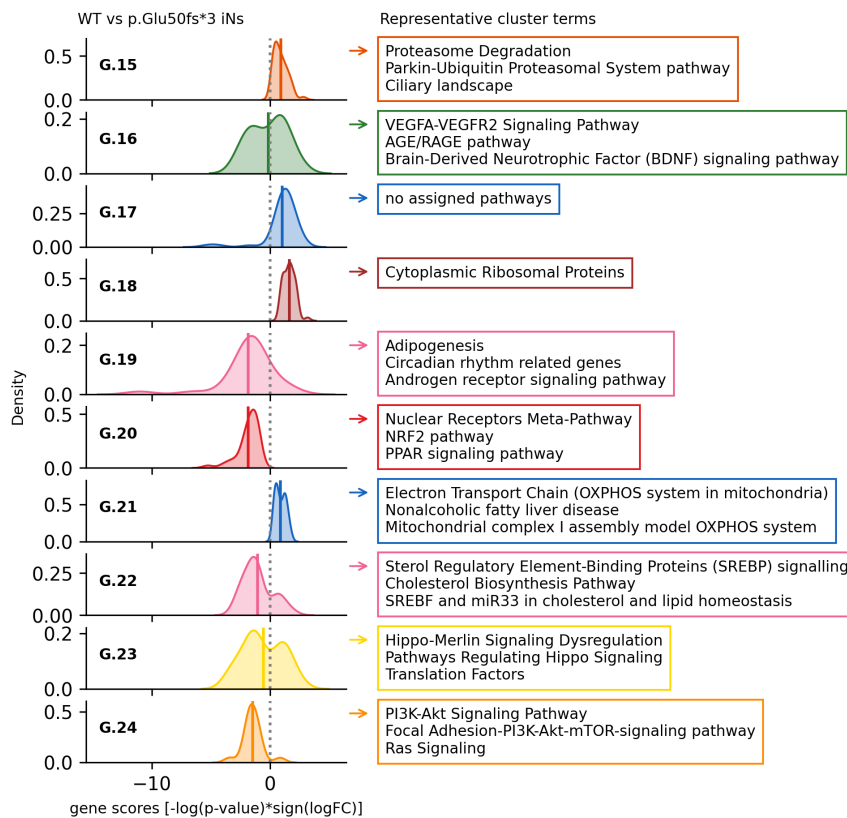
B



C



D



E

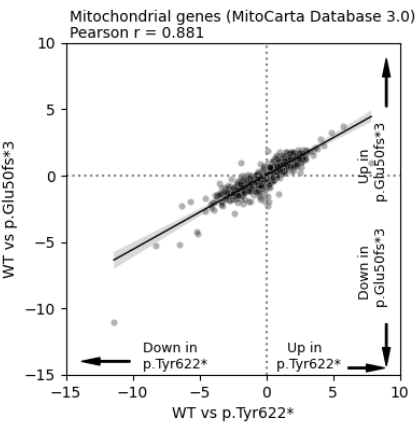
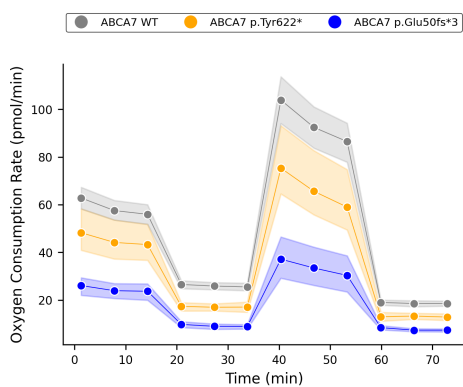


Figure S14: mRNA-seq analysis of p.Glu50fs* vs. WT iNs.

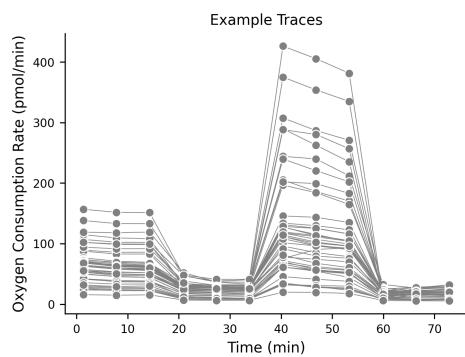
- (A) Kernighan-Lin (K/L) clustering of leading-edge genes from significantly perturbed pathways (Benjamini-Hochberg (BH) FDR-adjusted $p < 0.05$) in p.Glu50fs*3 vs. WT iNs. Colors represent distinct K/L clusters.
- (B) Heatmap of Jaccard index overlap between K/L gene clusters from p.Glu50fs*3 neurons and clusters identified in p.Tyr622* vs WT iNs. Red text denotes clusters with average score S upregulated in ABCA7 LoF; blue text denotes clusters with average S downregulated in ABCA7 LoF.
- (B) Heatmap showing Jaccard index overlap between K/L clusters identified in p.Glu50fs* vs. WT iNs and p.Tyr622* vs. WT iNs.
- (C) Heatmap of Jaccard index overlap between K/L gene clusters from p.Glu50fs*3 neurons and clusters identified in human postmortem excitatory neurons.

- (D) Gaussian kernel density plots of gene perturbation scores (S) within each cluster. Positive S indicates upregulation in p.Glu50fs*3. Solid lines denote cluster means. Top enriched pathways with highest intra-cluster connectivity indicated.
- (E) Correlation of per-gene perturbation scores ($S = -\log_{10}(\text{p-value}) \times \text{sign}(\log_2(\text{fold change}))$) between p.Glu50fs*3 vs. WT and p.Tyr622* vs. WT iNs for MitoCarta genes.

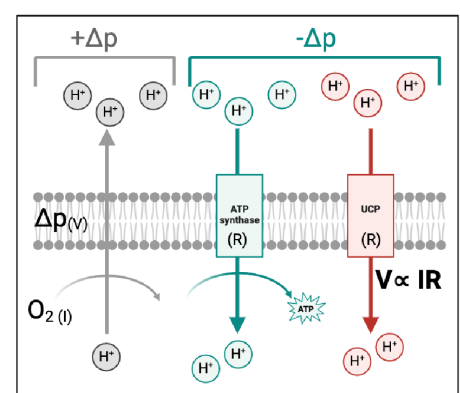
A



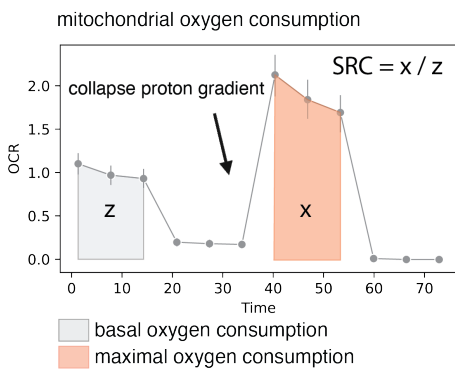
B



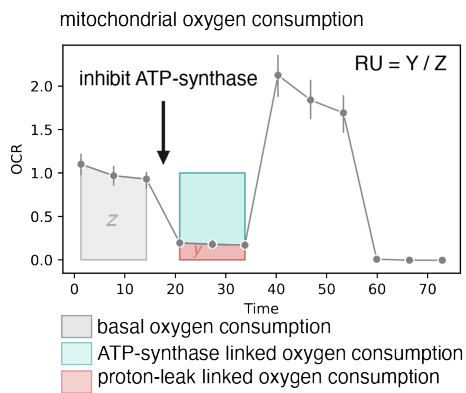
C



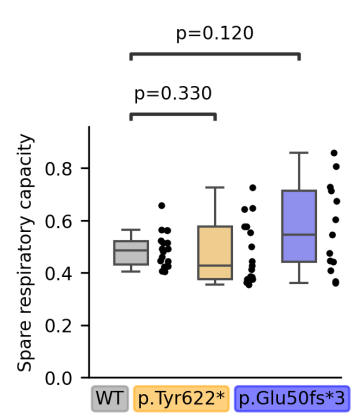
D



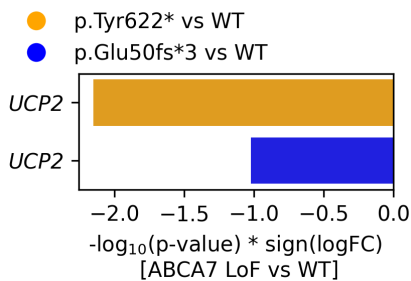
E



F



G



H

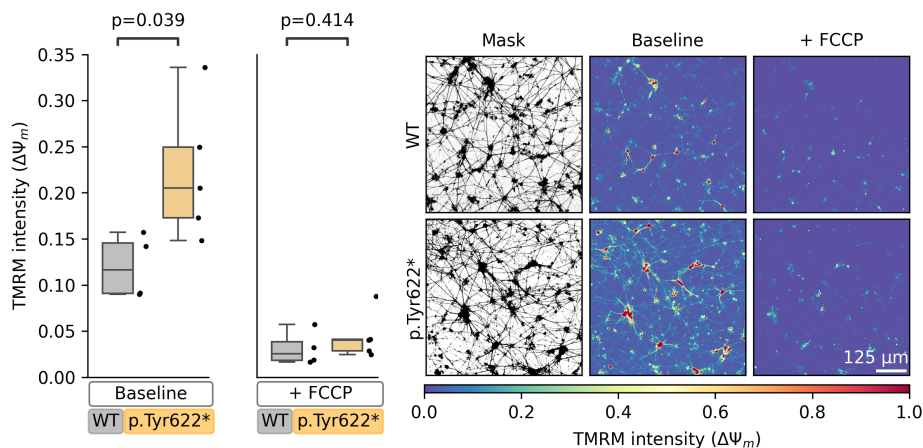
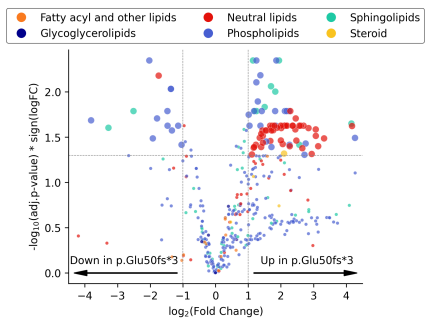


Figure S15: Analysis of Oxygen Consumption Rates in ABCA7 LoF vs. Control iNs.

- (A) Example oxygen consumption rate (OCR) curves from Batch 1 of the two differentiation batches used for analysis in Figure ???. The line plot indicates the per-condition mean estimator, and the error bars indicate the 95% confidence interval.
- (B) Representative per-well traces from (A).
- (C) Schematic indicating the relationship between oxygen consumption as a measure of proton current (I), which sustains the proton motive force (voltage, V). Regulation of ATP synthase and uncoupling protein (UCP) activity modifies resistance (R) and depletes the proton motive force.
- (D) Schematic indicating measurement of maximal and basal oxygen consumption to compute SRC.
- (E) Schematic indicating measurement of uncoupled oxygen consumption.
- (F) SRC computed for WT, ABCA7 p.Glu50fs*3, and ABCA7 p.Tyr622* iNs. P-values computed by independent sample t-test. N wells = 18 (WT), 17 (p.Tyr622*), 13 (p.Glu50fs*3) across two independent differentiation batches and Seahorse experiments.
- (G) UCP2 mRNA levels by genotype.
- (H) Mitochondrial membrane potential quantified by average TMRM fluorescence intensity per masked region (thresholded at 75th percentile) under baseline conditions and after addition of FCCP in ABCA7 LoF and WT iNs cultured for 4 weeks. Each datapoint represents average intensity per well. $N = 4$ (WT), 5 (p.Tyr622*) wells. Statistical comparison by independent-sample t -test. Same plot and images as shown under baseline conditions in Figure ??.

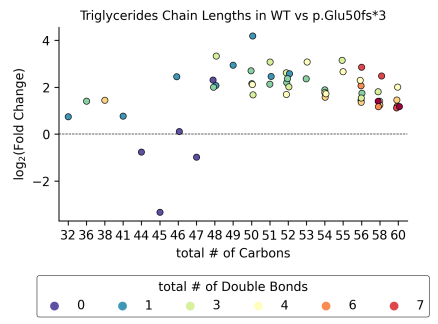
A



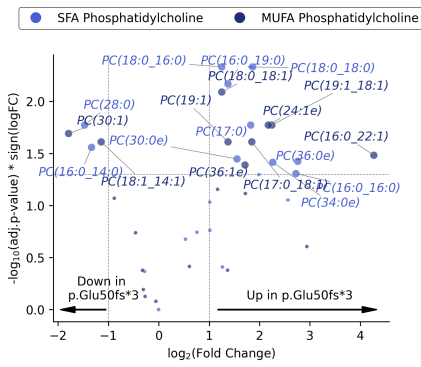
B

WT vs p.Glu50fs*3 Lipid Changes					
	Up	Down	Total	% Perturbed	Subclass
TG	45	0	45	83.3	triglyceride
PC	18	10	28	21.7	phosphatidylcholine
Cer	8	2	10	21.7	Ceramides
PS	1	1	2	8.7	phosphatidylserine
MG	0	1	1	14.3	monoglyceride
StE	1	0	1	100.0	Stigmasteryl Ester
PG	1	0	1	16.7	phosphatidylglycerol
MLCL	1	0	1	10.0	Cardiolipin
CL	1	0	1	4.5	Cardiolipin
ZyE	1	0	1	25.0	zymosteryl
Hex1Cer	1	0	1	14.3	Simple Glc series
DG	1	0	1	6.2	diglyceride

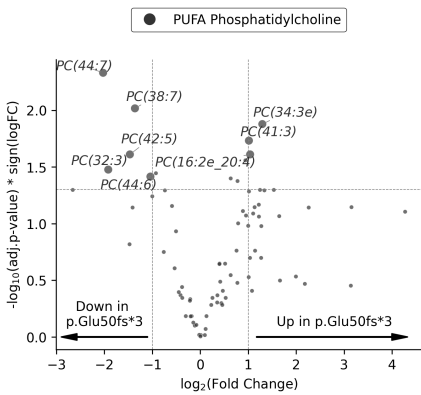
C



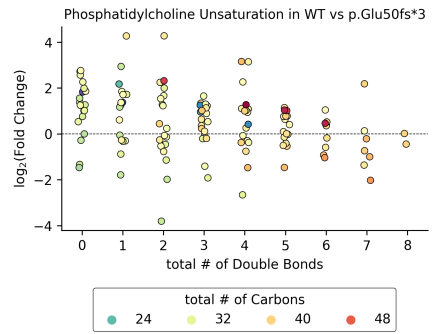
D



E



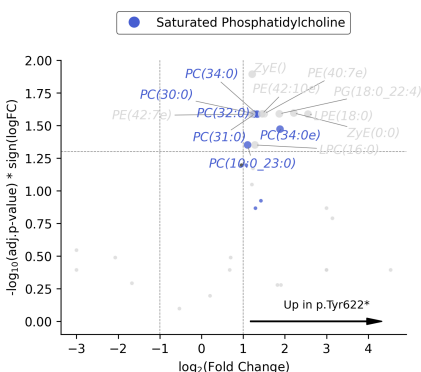
F



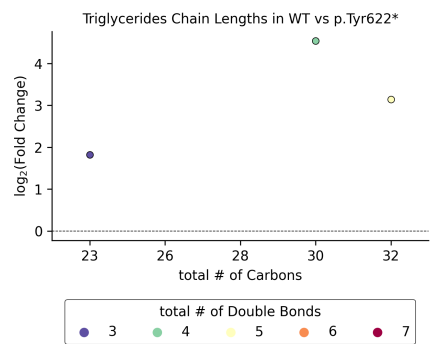
G

WT vs p.Tyr622* Lipid Changes					
	Up	Down	Total	% Perturbed	Subclass
PC	6	0	6	60.0	phosphatidylcholine
PE	3	0	3	60.0	phosphatidylethanolamine
ZyE	2	0	2	100.0	zymosteryl
LPC	1	0	1	25.0	lysophosphatidylcholine
LPE	1	0	1	100.0	lysophosphatidylethanolamine
PG	1	0	1	50.0	phosphatidylglycerol

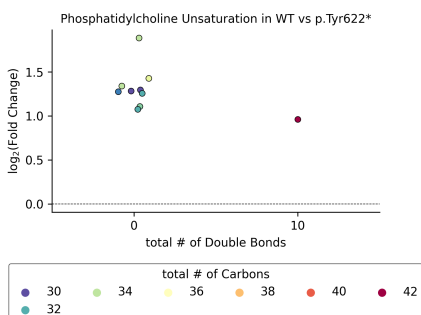
H



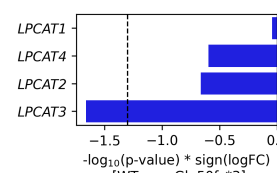
I



J



K



L

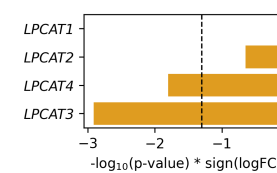


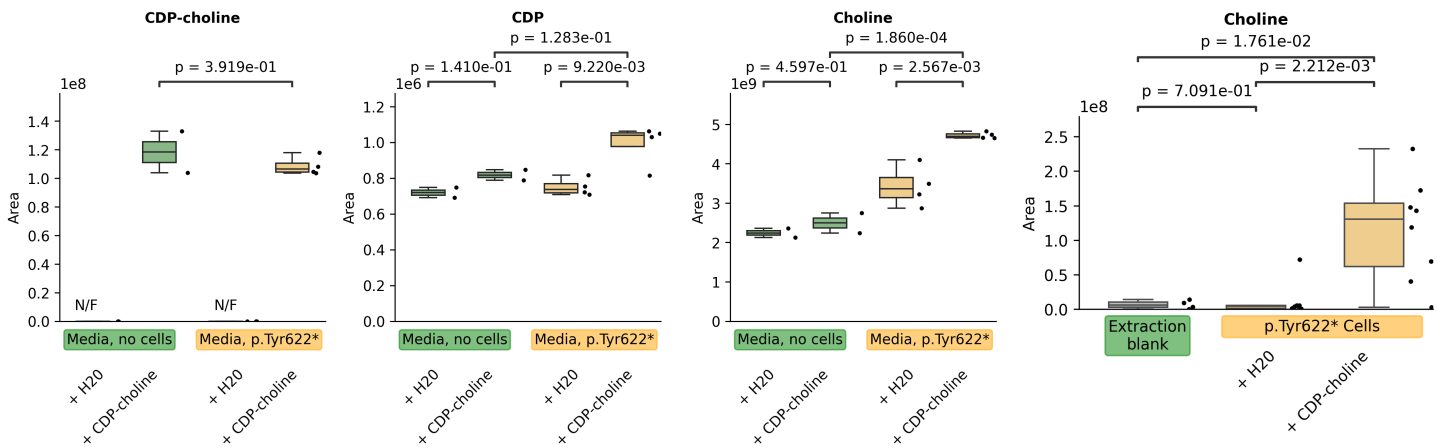
Figure S16: LC-MS Lipidomics in ABCA7 LoF iNs.

(A) Volcano plot of significantly perturbed lipid species identified by LC-MS in p.Glu50fs*3 vs. WT iNs (BH FDR-adjusted $p < 0.05$, $|\log_2(\text{FC})| > 1$), colored by lipid class. $N = 6$ wells per genotype.

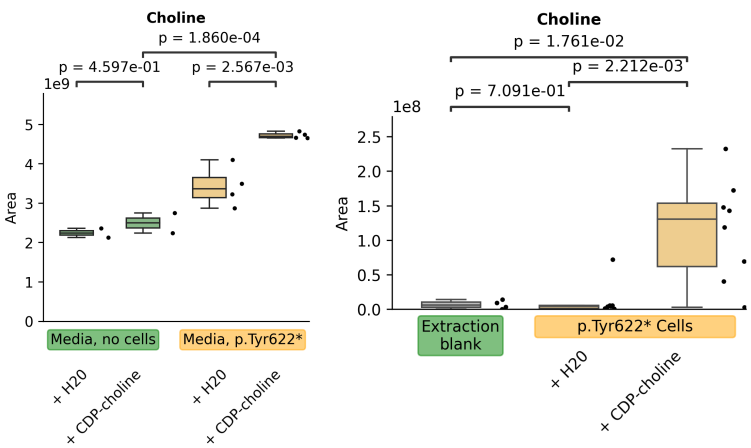
(B) Significantly perturbed lipid species from (A), summarized by lipid subclass.

- (C) Distribution of triglyceride fold changes grouped by fatty acid chain length and saturation for p.Glu50fs*3 vs. WT iNs.
- (D) Volcano plot highlighting significantly perturbed phosphatidylcholine species containing saturated or monounsaturated fatty acids (SFA/MUFA; BH FDR-adjusted $p < 0.05$, $|\log_2(\text{FC})| > 1$) for p.Glu50fs*3 vs. WT iNs.
- (E) Volcano plot highlighting significantly perturbed phosphatidylcholine species containing polyunsaturated fatty acids (PUFA; BH FDR-adjusted $p < 0.05$, $|\log_2(\text{FC})| > 1$) for p.Glu50fs*3 vs. WT iNs.
- (F) Distribution of phosphatidylcholine fold changes grouped by fatty acid chain length and saturation for p.Glu50fs*3 vs. WT iNs.
- (G) Table summarizing significantly perturbed lipid species by lipid subclass in p.Tyr622* vs. WT iNs ($N = 10$ WT, 8 p.Tyr622* wells; BH FDR-adjusted $p < 0.05$, $|\log_2(\text{FC})| > 1$).
- (H) Volcano plot showing lipid species from (G), colored by lipid class; phosphatidylcholines highlighted in blue, for p.Tyr622* vs. WT iNs.
- (I,J) Same analysis as (C,F), but comparing p.Tyr622* vs. WT iNs.
- (K,L) Expression changes (mRNA) of LPCAT genes comparing p.Tyr622* vs. WT and p.Glu50fs*3 vs. WT iNs.

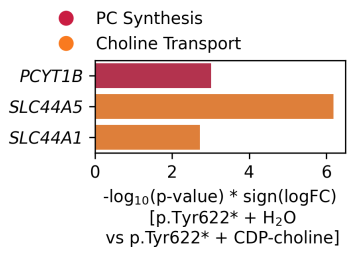
A



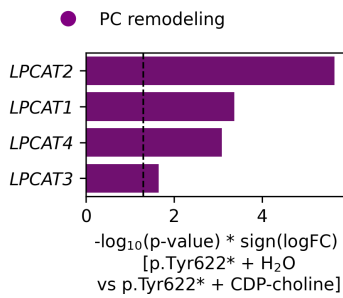
B



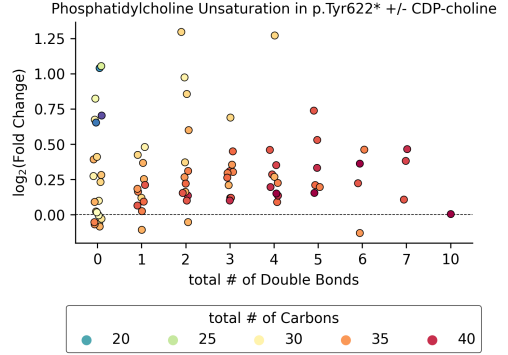
C



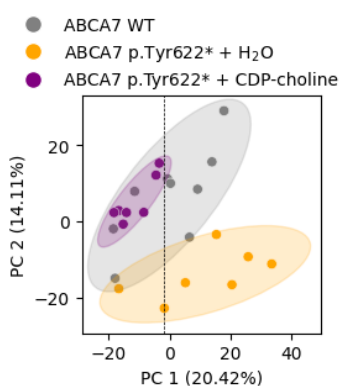
D



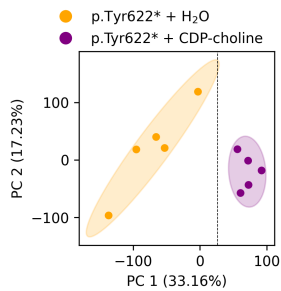
E



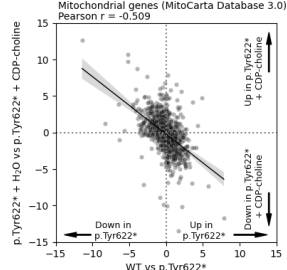
F



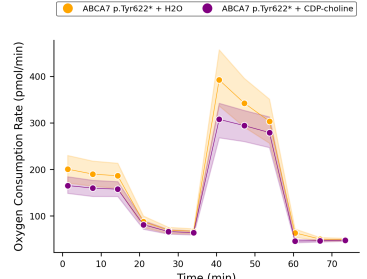
G



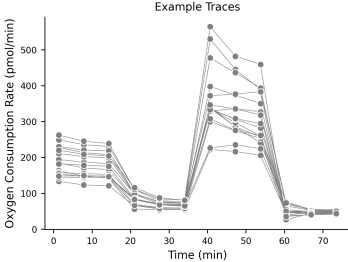
H



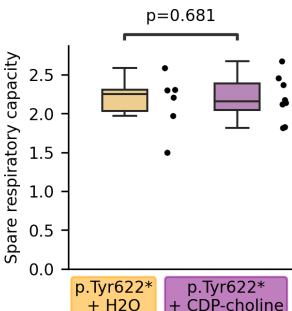
I



J



K



L

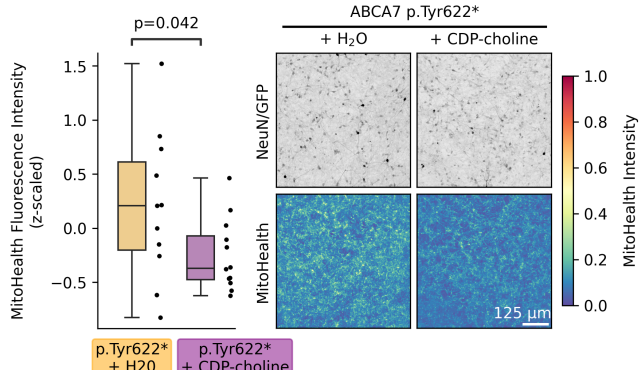
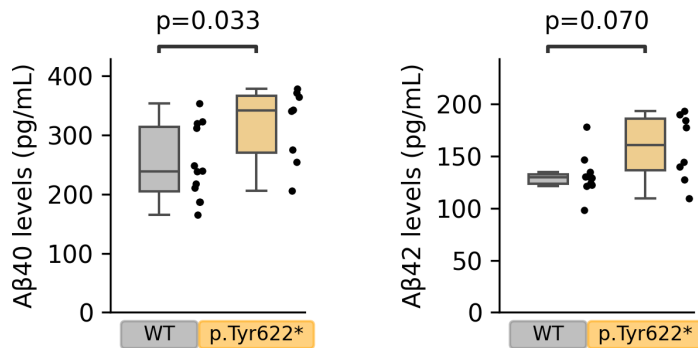


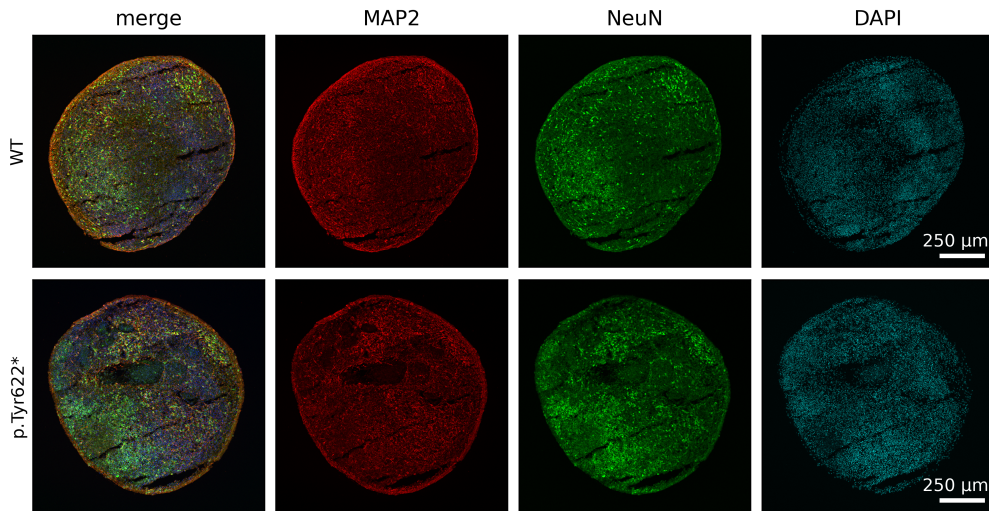
Figure S17: Effects of CDP-choline Treatment in p.Tyr622* iNs.

- (A) Choline metabolites detected in media by targeted LC-MS. $N = 2$ for media without cells, $N = 4$ for cell-conditioned media; N/F indicates not detected.
- (B) Choline metabolites detected intracellularly by targeted LC-MS. $N = 8$ per genotype, $N = 4$ blanks.
- (C) Selected choline synthesis and transport genes differentially expressed in p.Tyr622* ± CDP-choline iNs (mRNA-seq).
- (D) LPCAT gene expression changes in p.Tyr622* ± CDP-choline iNs (mRNA-seq).
- (E) Distribution of phosphatidylcholine species fold-changes by fatty acid chain length and saturation in p.Tyr622* ± CDP-choline iNs.
- (F) PCA plot of untargeted LC-MS metabolite profiles from p.Tyr622* ± CDP-choline and WT iNs.
- (G) PCA plot of mRNA-seq data from p.Tyr622* ± CDP-choline iNs.
- (H) Correlation of gene perturbation scores (S) for mitochondrial-localized genes comparing p.Tyr622* ± CDP-choline iNs versus p.Glu50fs*3 vs. WT iNs.
- (I) Example Seahorse oxygen consumption rate (OCR) curves. Lines represent per-condition means; error bars indicate 95% confidence intervals.
- (J) Representative per-well OCR traces from (I).
- (K) Quantification of spare respiratory capacity (SRC) from OCR curves in (I). Statistical comparisons by independent-sample t -tests; $N = 6$ wells (p.Tyr622* + H₂O), $N = 8$ wells (p.Tyr622* + CDP-choline). Boxes indicate quartiles; whiskers extend to data within 1.5×IQR from quartiles.
- (L) Quantification of mitochondrial membrane potential via neuronal HCS MitoHealth dye fluorescence intensity. Statistical comparisons by linear mixed-effects model on per-NeuN+ volume averages, with well-of-origin as random effect. $N = 11$ wells (p.Tyr622*), $N = 9$ wells (p.Glu50fs*3), $N = 8$ wells (WT); ~3000 cells per condition from three differentiation batches. Individual data points represent per-well averages. Right: Representative images shown as mean-intensity projections of NeuN+ staining and corresponding MitoHealth and Hoechst signals within quantified NeuN+ volumes. Each NeuN/GFP image intensity was scaled relative to its maximum value, followed by gamma correction ($\gamma = 0.5$) for visualization.

A



B



C

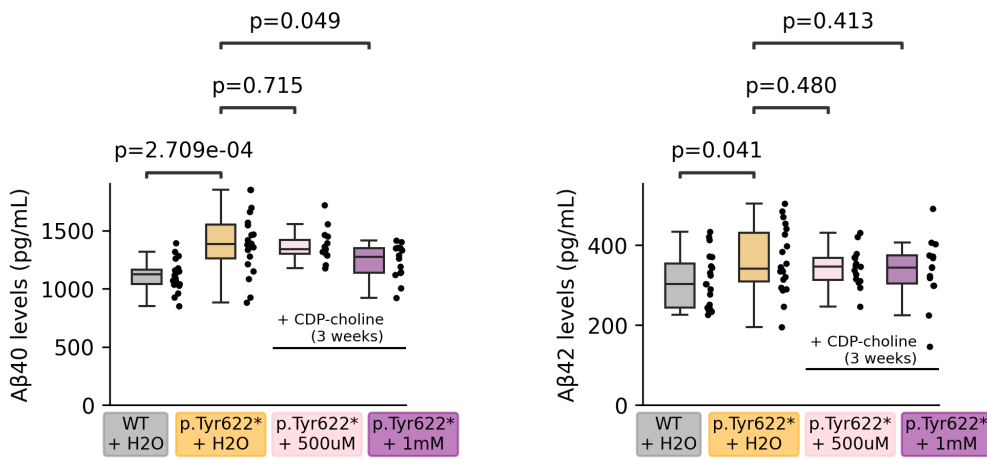


Figure S18: CDP-choline Treatment in Cortical Organoids

- (A) Amyloid- β levels quantified by ELISA from media of 4-week-old iNs.
- (B) Representative images of cortical organoid slices from indicated genotypes.
- (C) Amyloid- β levels quantified by ELISA from media of cortical organoids (176 days old), grouped by genotype and treated with 500 μ M or 1 mM CDP-choline for 3 weeks. Samples correspond to organoids in Figure ??K, analyzed one week prior to assays presented there.

Supplementary Tables

Table S1: Annotation of ABCA7 loss of function variants used in this study.

rsID	HGVS.c	HGVS.p	Annotation	AD association	N in cohort
rs113809142	c.4416+2T>G	NA	splice donor variant [130]	Steinberg et al (2015), Nature Genetics, Table 1 [131]	1
rs200538373	c.5570+5G>C	NA	splice region variant [130, 131]	Steinberg et al (2015), Nature Genetics, Table 1 [131]	4
rs538591288	c.4208delT	p.Leu1403fs	frameshift variant [130]	Steinberg et al (2015), Nature Genetics, Table 1 [131]	1
rs547447016	c.2126_2132delAGCAGGG	p.Glu709fs	frameshift variant [130]	Steinberg et al (2015), Nature Genetics, Table 1 [131]	4
rs201060968	c.3641G>A	p.Trp1214*	stop gained	NA	1
19_1053362_G_A	c.3255G>A	p.Trp1085*	stop gained	NA	1

Table S2: PCR/Sanger sequencing (SS) primers.

Primer	Sequence
rs547447016_FOR	5'-ACGCTGGCCTGGATCTACTC-3'
rs547447016_REV	5'-TGCATGCGTGTGCCAAGAAG-3'
chr19.1053362G>A_rs201060968_FOR	5'-CTGAAGCACCCCTTGTCAC-3'
chr19.1053362G>A_rs201060968_REV	5'-GAAAGCGCTTGAGAAGCAGGG-3'
chr19.1053362G>A_REV_SS	5'-GCTGCTCATAAACACGCTATTCATCCTTC-3'
rs201060968_FOR_SS	5'-CATTGCTGGCCTAGACGTAA-3'
ABCA7_p.Glu50fs*3_FOR	5'-GTGACGAAAGCGTTAACGCC-3'
ABCA7_p.Glu50fs*3_REV	5'-GCAGTGGCTTGGTGGAAAG-3'
ABCA7_p.Tyr622*_FOR	5'-CTGGTTCTGGTGCTCAAG-3'
ABCA7_p.Tyr622*_REV	5'-CCTACGGCAGACGTCTTCAG-3'

Table S3: Experimentally-determined 3D ABCA7 structures used in molecular dynamics simulations.

System	PDB ID	State
CLOSE-G1527	8EOP	HOLO
CLOSE-A1527	8EOP	HOLO
OPEN-G1527	8EE6	APO
OPEN-A1527	8EE6	APO

Table S4: Enrichments of MitoCarta mitochondrial pathways in WT vs p.Tyr622* mRNA

Term	score	P-value	FDR	Genes
Apoptosis	1.900274	0.012581	0.415774	BID; CASP3; CYCS; BCL2L1; BIK
OXPHOS	1.894438	0.012752	0.415774	NDUFA4; TMEM126A; ATP5MG; SDHAF2; NDUFA1; COX6A1; COX14; CYCS; COA4; NDUFS4; ATP5PB; ATP5MC3; NDUFAF2; MT-ND2
Protein import and sorting	1.755279	0.017568	0.415774	TIMM8A; TIMM10; DNAJC19; SAMM50; TIMM23; TOMM22
OXPHOS subunits	1.552584	0.028017	0.477391	NDUFA4; ATP5MG; NDUFA1; COX6A1; CYCS; NDUFS4; ATP5PB; ATP5MC3; MT-ND2
Mitochondrial dynamics and surveillance	1.473414	0.033619	0.477391	BID; ATP5MG; SAMM50; CASP3; CYCS; BCL2L1; FUNDC1; BIK; FUNDC2
Amino acid metabolism	-1.374004	0.042267	0.263353	DLST; COMT; SLC25A44; MAOA; ABAT; SFXN3; GCAT; ALDH5A1; MCCC2; AADAT
Detoxification	-1.395286	0.040245	0.263353	EPHX2; DHRS2; CYB5B; CAT; TXNRD2; MAOA; CYB5R3
EF hand proteins	-1.441227	0.036205	0.263353	RHOT2; SLC25A23; SLC25A25
Lipid metabolism	-1.441792	0.036158	0.263353	EPHX2; SLC25A1; ACADVL; GPAT2; CPT1C; ACADL; IDI1; ACP6; CROT; CYB5R3; CYP27A1; ACAD10
Amidoxime reducing complex	-1.576863	0.026493	0.238440	CYB5R3; CYB5B
Vitamin metabolism	-1.639877	0.022915	0.232016	MMAB; DHRS4; PLPBP; PNPO; RFK; PC; SFXN3
Gluconeogenesis	-1.844185	0.014316	0.165654	PCK2; PC; SLC25A1
Catechol metabolism	-1.857772	0.013875	0.165654	COMT; MAOA
TCA-associated	-1.887037	0.012971	0.165654	ACLY; PCK2; PC; SLC25A1
ABC transporters	-2.026052	0.009418	0.165654	ABCB6; ABCD2; ABCB8
Xenobiotic metabolism	-2.103329	0.007883	0.165654	EPHX2; DHRS2; CYB5B; MAOA; CYB5R3
Vitamin B6 metabolism	-2.314663	0.004845	0.165654	PNPO; PLPBP

Metabolism	-4.519649	0.000030	0.002448	NMNAT3; DHRS4; CAT; GPAT2; DLAT; FECH; PNPO; SLC25A25; MCCC2; MMAB; COQ9; SLC25A1; PLPBP; ACLY; TXNRD2; ABAT; RFK; TK2; PC; IDI1; PCK2; EPHX2; DHRS2; ACADVL; IDH2; CPT1C; CROT; ALDH5A1; AADAT; ACAD10; TSTD1; CYB5B; DLST; SLC25A44; ABCB6; GATM; SLC25A23; MAOA; ACADL; SFXN3; ACP6; GCAT; COMT; CYP27A1; CYB5R3
------------	-----------	----------	----------	---

Table S5: Enrichments of MitoCarta mitochondrial pathways in p.Tyr622* + H₂O vs p.Tyr622* + CDP-choline mRNA

Term	score	P-value	FDR	Genes
EF hand proteins	4.457699	0.000035	0.003451	SLC25A12; SLC25A23; SLC25A25; EFHD1; MICU2; SLC25A13; MICU3; SLC25A24
Small molecule transport	3.256577	0.000554	0.027418	ABCB10; SLC25A25; MPV17L; ABCD3; ABCD1; SLC25A12; SLC25A1; SLC25A13; MICU3; SFXN1; SLC25A29; SLC25A39; SLC25A43; MICU2; SFXN5; STARD7; SLC25A24; ABCD2; SLC25A15; SLC25A22; SLC25A23; VDAC1; MPV17
Calcium homeostasis	3.079591	0.000833	0.027474	SLC25A12; SLC25A23; SLC25A25; EFHD1; VDAC1; LETM1; SLC25A13; MICU2; MICU3; SLC25A24
Metabolism	2.846777	0.001423	0.033450	ABCB10; NT5DC2; ACSL6; ME3; CS; SLC25A12; PDSS2; HSD17B4; ACLY; TK2; ALDH3A2; IDI1; NADK2; ACADS; CPT2; STARD7; AADAT; ACAD10; AK3; NNT; SOD2; CHCHD7; SLC25A23; OGDH; NMNAT3; MT-CO1; GLS; GPAT2; SLC25A25; OAT; D2HGDH; SLC25A1; ABAT; RFK; SFXN1; ALDH1B1; OXCT1; TST; HIBCH; FHIT; FH; GLYCTK; LACTB; PNPO; SERAC1; ME2; GSR; AGPAT5; PCK2; SLC25A29; EPHX2; GLDC; SFXN5; PDK3; ALDH5A1; SPHK2; SLC25A24; TSTD1; MTFMT; ACP6; NT5M; ALDH9A1; GCAT; KMO; ECI1; CAT; DLAT; COQ2; PPM1K; PRXL2A; MCC2; CISD3; SPTLC2; SLC25A13; SLC25A15; FASN; ALDH7A1; DLST; GATM; AK4; ACADSB

Signaling	2.772263	0.001689	0.033450	NLRX1; SLC25A12; PPTC7; SLC25A23; SLC25A25; EFHD1; VDAC1; LETM1; MACROD1; SLC25A13; MICU2; PDE2A; MICU3; SLC25A24; DELE1
TCA-associated	2.563737	0.002731	0.045055	SLC25A1; ACLY; ME2; SFXN5; ME3; D2HGDH; PCK2
Fusion	2.466941	0.003412	0.048261	OPA1; MIGA2; MFN2; MIGA1; MFN1
Carbohydrate metabolism	1.960909	0.010942	0.123756	OXCT1; CS; SLC25A12; SLC25A1; FH; DLAT; ACLY; ME2; GLYCTK; DLST; OGDH; SLC25A13; ME3; SFXN5; PDK3; D2HGDH; PCK2
Organelle contact sites	1.856642	0.013911	0.123756	FKBP8; SPIRE1; MIGA2; MFN2; MFN1; VDAC1
ABC transporters	1.852052	0.014059	0.123756	ABCB10; ABCD1; ABCD2; ABCD3
Phospholipid metabolism	1.850381	0.014113	0.123756	GPAT2; SERAC1; SPTLC2; LACTB; ACP6; STARD7; AGPAT5; SPHK2
Amino acid metabolism	1.823889	0.015001	0.123756	GLS; OAT; PPM1K; MCCC2; SLC25A12; ABAT; SLC25A13; SFXN1; SLC25A29; GLDC; ALDH5A1; AA-DAT; HIBCH; ALDH9A1; SLC25A15; ALDH7A1; DLST; GCAT; ACADSB; KMO
Nucleotide metabolism	1.357357	0.043918	0.334453	AK3; NT5DC2; SLC25A23; SLC25A25; GATM; AK4; TK2; NT5M; SLC25A24; FHIT
OXPHOS assembly factors	-1.423365	0.037725	0.363536	FOXRED1; TIMMDC1; COA3; COA6; COX7A2L; SDHAF3; FMC1; COX16; RAB5IF; NDUFAF6; SD-HAF2; SURF1; TIMM21; BCS1L; COA7; NDUFAF1; COX14; LYRM2; TMEM70
Protein import and sorting	-1.445375	0.035861	0.363536	MTX2; TIMM8A; TIMM23; TIMM17B; TIMM10; UQCRC1; DNAJC19; PMPCA; TIMM8B; MTX1; TIMM21; TIMM22; TOMM5; GRPEL1
CIII subunits	-1.603039	0.024944	0.293782	UQCR10; CYC1; UQCRH; UQCRC1; UQCRCFS1

mtRNA granules	-1.605563	0.024799	0.293782	MRPL47; ERAL1; MTPAP; ALKBH1; PTCD2; MRPS7; TFB1M; TRUB2; RMND1; TRMT10C	
CII subunits	-1.645356	0.022628	0.293782	SDHD; SDHC; SDHB	
Complex II	-2.114075	0.007690	0.135856	SDHAF2; SDHAF3; SDHC; SDHB; SDHD	
OXPHOS subunits	-2.580372	0.002628	0.055714	UQCR10; ATP5MG; SDHB; ATP5PB; UQCRH; NDUFA10; COX5B; COX7A2L; NDUFB3; NDUFA4; CYC1; SDHD; MT-ND4L; UQCRCFS1; ATP5IF1; NDUFA1; NDUFV1; COX6A1; NDUFB8; ATP5F1A; SDHC; NDUFB6; NDUFA6; NDUFS4; COX7A2; UQCRC1; NDUFS2; ATP5F1C	
Mitochondrial dogma	central	-2.864986	0.001365	0.036163	MRPL4; MRPL18; COA3; MTRES1; MRPL46; MTIF3; MRPS23; MRPL37; MRPL45; MRPL36; TRUB2; MRPS10; MRPL24; PTCD2; MRPL40; MRPS18C; UNG; TFB1M; METTL5; MRPS12; MRPL14; GATC; MRPL34; MRPL32; MRPL16; TSFM; MTPAP; MRPL47; APEX1; MRPS21; ALKBH1; TEFM; MRPL55; MRPL39; MRPS7; MRPS26; MRPL22; TIMM21; MRPL15; MTERF2; NGRN; MRPS18A; TRMT10C; MTERF1; ERAL1; MRM3; COX14; MRPS31; MRPL13; PTCD3; MRPS14; DAP3; MTERF3; MRPL27; MRPS28; RARS2; MRPS18B; RMND1; MRPS15

OXPHOS	-3.420637	0.000380	0.013414	UQCR10; FOXRED1; TIMMDC1; ATP5MG; COA3; SDHB; ATP5PB; UQCRH; NDUFA10; COX5B; COA6; COX7A2L; NDUFB3; NDUFA4; CYC1; SDHAF3; FMC1; SDHD; MT-ND4L; UQCRFS1; ATP5IF1; RAB5IF; COX16; NDUFAF6; SD-HAF2; SURF1; NDUFV1; NDUFA1; COX6A1; TIMM21; NDUFB8; BCS1L; COA7; NDUFA12; NDUFAF1; ATP5F1A; COX14; SDHC; ND-UFA6; NDUFB6; LYRM2; NDUFS4; COX7A2; UQCRC1; TMEM70; NDUFS2; ATP5F1C
Translation	-4.653989	0.000022	0.001176	MRPL4; MRPL18; COA3; MTRES1; MRPL46; MTIF3; MRPS23; MRPL37; MRPL45; MRPL36; MRPS10; MRPL24; MRPL40; MRPS18C; TFB1M; MRPS12; MRPL14; GATC; MRPL34; MRPL32; MRPL16; TSFM; MRPL47; MRPS21; MRPL55; MRPL39; MRPS7; MRPS26; MRPL22; TIMM21; MRPL15; NGRN; MRPS18A; ERAL1; MRM3; COX14; MRPS31; MRPL13; PTCD3; DAP3; MRPS14; MTERF3; MRPL27; MRPS18B; RARS2; MRPS28; RMND1; MRPS15
Mitochondrial ribosome	-6.408523	0.000000	0.000041	MRPL4; MRPL18; MRPL46; MRPS23; MRPL37; MRPL45; MRPL36; MRPS10; MRPL24; MRPL40; MRPS18C; MRPS12; MRPL14; MRPL34; MRPL32; MRPL16; MRPL47; MRPS21; MRPL55; MRPL39; MRPS7; MRPS26; MRPL22; MRPL15; MRPS18A; MRPS31; MRPL13; PTCD3; DAP3; MRPS14; MRPL27; MRPS18B; MRPS28; MRPS15

Table S6: External datasets used.

Description	Access	Reference
postmortem human PFC proteomic data	https://www.synapse.org/#!Synapse:syn21449368	[132]
Reference 1: Cell type specific marker genes for human brain	https://osf.io/vn7w2/	[133]
Reference 2: Cell type specific marker genes for human brain	https://osf.io/vn7w2/	[134]
Gene Ontology Biological Process 2023	https://maayanlab.cloud/Enrichr/#1 NA ibraries	NA
NeuN+/- bulk RNA-sequencing from postmortem human brain	https://osf.io/vn7w2/	[51]
WikiPathways 2019 Human	https://maayanlab.cloud/Enrichr/#1 NA ibraries	NA
snRNAseq from postmortem human PFC from p.Ala1527Gly variant-carriers and controls	https://www.synapse.org/#!Synapse:syn52293417	[53]
Human MioCarta3.0	https://www.broadinstitute.org/maticarta/mitocarta30-inventory-mammalian-mitochondrial-proteins-and-pathways	NA
Human prefrontal cortex layer markers based transcriptomics on dissected layers	https://www.nature.com/articles/nn.4548#article-info	[126]
Human dorsolateral prefrontal cortex spatial transcriptomics markers	https://www.nature.com/articles/s41593-020-00787-0#article-info	[127]

Table S7: Antibodies used.

Antibody name	Company	Catalog No.
NeuN	Synaptic Systems	266004
Tuj1	BioLegend	MMS-435P
SM312 (pan-axonal marker)	Bioread	837904
MAP2	Biolegend	822501

Extended Data

Data S1. ABCA7 PTC variants identified in the snRNA-seq cohort

Data S2. Metadata for selected individuals from the ROSMAP cohort used in this study

Data S3. snRNA-seq quality control metrics

Data S4. Differential gene expression statistics by cell type

Data S5. Gene Ontology (GO) pathway enrichment results

Data S6. WikiPathways enrichment results in excitatory neurons

Data S7. Kernighan-Lin (K/L) gene cluster assignments

Data S8. RNA-seq differential expression statistics in NGN2-induced neurons

Data S9. Lipidomics differential abundance statistics in NGN2-induced neurons

Data S10. Targeted metabolomics on cells and media, with and without CDP-choline treatment

References

- [1] World Health Organization. *Dementia Fact Sheet*. Accessed: 2025-03-28. 2023. URL: <https://www.who.int/news-room/fact-sheets/detail/dementia>.
- [2] Alzheimer's Association. "2016 Alzheimer's disease facts and figures". en. In: *Alzheimers. Dement.* 12.4 (Apr. 2016), pp. 459–509.
- [3] Ida K Karlsson et al. "Measuring heritable contributions to Alzheimer's disease: polygenic risk score analysis with twins". en. In: *Brain Commun* 4.1 (Jan. 2022), fcab308.
- [4] J C Lambert et al. "Meta-analysis of 74,046 individuals identifies 11 new susceptibility loci for Alzheimer's disease". en. In: *Nat. Genet.* 45.12 (Dec. 2013), pp. 1452–1458.
- [5] Riccardo E Marioni et al. "Correction: GWAS on family history of Alzheimer's disease". en. In: *Transl. Psychiatry* 9.1 (June 2019), p. 161.
- [6] Iris E Jansen et al. "Genome-wide meta-analysis identifies new loci and functional pathways influencing Alzheimer's disease risk". en. In: *Nat. Genet.* 51.3 (Mar. 2019), pp. 404–413.
- [7] Brian W Kunkle et al. "Genetic meta-analysis of diagnosed Alzheimer's disease identifies new risk loci and implicates A β , tau, immunity and lipid processing". en. In: *Nat. Genet.* 51.3 (Mar. 2019), pp. 414–430.
- [8] Douglas P Wightman et al. "A genome-wide association study with 1,126,563 individuals identifies new risk loci for Alzheimer's disease". en. In: *Nat. Genet.* 53.9 (Sept. 2021), pp. 1276–1282.
- [9] Céline Bellenguez et al. "New insights into the genetic etiology of Alzheimer's disease and related dementias". en. In: *Nat. Genet.* 54.4 (Apr. 2022), pp. 412–436.
- [10] Michael E Belloy et al. "APOE Genotype and Alzheimer Disease Risk Across Age, Sex, and Population Ancestry". en. In: *JAMA Neurol.* 80.12 (Dec. 2023), pp. 1284–1294.
- [11] Stacy Steinberg et al. "Loss-of-function variants in ABCA7 confer risk of Alzheimer's disease". en. In: *Nat. Genet.* 47.5 (May 2015), pp. 445–447.
- [12] Arne De Roeck, Christine Van Broeckhoven, and Kristel Sleegers. "The role of ABCA7 in Alzheimer's disease: evidence from genomics, transcriptomics and methylomics". en. In: *Acta Neuropathol.* 138.2 (Aug. 2019), pp. 201–220.
- [13] Christiane Reitz et al. "Variants in the ATP-binding cassette transporter (ABCA7), apolipoprotein E 4, and the risk of late-onset Alzheimer disease in African Americans". en. In: *JAMA* 309.14 (Apr. 2013), pp. 1483–1492.
- [14] Henne Holstege et al. "Exome sequencing identifies rare damaging variants in ATP8B4 and ABCA1 as risk factors for Alzheimer's disease". en. In: *Nat. Genet.* 54.12 (Dec. 2022), pp. 1786–1794.

- [15] Nicholas N Lyssenko and Domenico Praticò. “ABCA7 and the altered lipidostasis hypothesis of Alzheimer’s disease”. en. In: *Alzheimers. Dement.* 17.2 (Feb. 2021), pp. 164–174.
- [16] Kilan Le Guennec et al. “ABCA7 rare variants and Alzheimer disease risk”. en. In: *Neurology* 86.23 (June 2016), pp. 2134–2137.
- [17] Paul Hollingworth et al. “Common variants at ABCA7, MS4A6A/MS4A4E, EPHA1, CD33 and CD2AP are associated with Alzheimer’s disease”. en. In: *Nat. Genet.* 43.5 (Apr. 2011), pp. 429–435.
- [18] Adam C Naj et al. “Common variants at MS4A4/MS4A6E, CD2AP, CD33 and EPHA1 are associated with late-onset Alzheimer’s disease”. en. In: *Nat. Genet.* 43.5 (May 2011), pp. 436–441.
- [19] Woojin Scott Kim, Cynthia Shannon Weickert, and Brett Garner. “Role of ATP-binding cassette transporters in brain lipid transport and neurological disease”. en. In: *J. Neurochem.* 104.5 (Mar. 2008), pp. 1145–1166.
- [20] Radosveta Koldamova, Nicholas F Fitz, and Iliya Lefterov. “ATP-binding cassette transporter A1: from metabolism to neurodegeneration”. en. In: *Neurobiol. Dis.* 72 Pt A (Dec. 2014), pp. 13–21.
- [21] Sumiko Abe-Dohmae et al. “Human ABCA7 supports apolipoprotein-mediated release of cellular cholesterol and phospholipid to generate high density lipoprotein”. en. In: *J. Biol. Chem.* 279.1 (Jan. 2004), pp. 604–611.
- [22] Nan Wang et al. “ATP-binding cassette transporter A7 (ABCA7) binds apolipoprotein A-I and mediates cellular phospholipid but not cholesterol efflux”. en. In: *J. Biol. Chem.* 278.44 (Oct. 2003), pp. 42906–42912.
- [23] Maiko Tomioka et al. “Lysophosphatidylcholine export by human ABCA7”. en. In: *Biochim. Biophys. Acta Mol. Cell Biol. Lipids* 1862.7 (July 2017), pp. 658–665.
- [24] Antonino Picataggi et al. “Specificity of ABCA7-mediated cell lipid efflux”. en. In: *Biochim. Biophys. Acta Mol. Cell Biol. Lipids* 1867.7 (July 2022), p. 159157.
- [25] Faraz Quazi and Robert S Molday. “Differential phospholipid substrates and directional transport by ATP-binding cassette proteins ABCA1, ABCA7, and ABCA4 and disease-causing mutants”. en. In: *J. Biol. Chem.* 288.48 (Nov. 2013), pp. 34414–34426.
- [26] Shu-Cheng Fang et al. “Structural insights into human ABCA7-mediated lipid transport”. In: *Structure* 33.3 (Mar. 2025), 583–593.e5. ISSN: 0969-2126. doi: 10.1016/j.str.2024.12.015. URL: <http://dx.doi.org/10.1016/j.str.2024.12.015>.
- [27] Tomonori Aikawa, Marie-Louise Holm, and Takahisa Kanekiyo. “ABCA7 and Pathogenic Pathways of Alzheimer’s Disease”. en. In: *Brain Sci* 8.2 (Feb. 2018).

- [28] Nobukiyo Tanaka et al. “Roles of ATP-binding cassette transporter A7 in cholesterol homeostasis and host defense system”. en. In: *J. Atheroscler. Thromb.* 18.4 (2011), pp. 274–281.
- [29] Lena Duchateau et al. “CSF biomarker analysis of ABCA7 mutation carriers suggests altered APP processing and reduced inflammatory response”. en. In: *Alzheimers. Res. Ther.* 15.1 (Nov. 2023), p. 195.
- [30] Keiji Kawatani et al. “ABCA7 deficiency causes neuronal dysregulation by altering mitochondrial lipid metabolism”. en. In: *Mol. Psychiatry* (Dec. 2023), pp. 1–11.
- [31] Hüseyin Tayran et al. “ABCA7-dependent Neuropeptide-Y signalling is a resilience mechanism required for synaptic integrity in Alzheimer’s disease”. en. In: *bioRxiv* (Jan. 2024).
- [32] Ni Wang et al. “Neuronal ABCA7 deficiency aggravates mitochondrial dysfunction and neurodegeneration in Alzheimer’s disease”. en. In: *Alzheimers. Dement.* 21.3 (Mar. 2025), e70112.
- [33] Kanayo Satoh et al. “ATP-binding cassette transporter A7 (ABCA7) loss of function alters Alzheimer amyloid processing”. en. In: *J. Biol. Chem.* 290.40 (Oct. 2015), pp. 24152–24165.
- [34] Nobutaka Sakae et al. “ABCA7 Deficiency Accelerates Amyloid- β Generation and Alzheimer’s Neuronal Pathology”. en. In: *J. Neurosci.* 36.13 (Mar. 2016), pp. 3848–3859.
- [35] Sharon L Chan et al. “ATP-binding cassette transporter A7 regulates processing of amyloid precursor protein in vitro”. en. In: *J. Neurochem.* 106.2 (July 2008), pp. 793–804.
- [36] Michelle Bamji-Mirza et al. “Genetic Variations in ABCA7 Can Increase Secreted Levels of Amyloid- β 40 and Amyloid- β 42 Peptides and ABCA7 Transcription in Cell Culture Models”. en. In: *J. Alzheimers. Dis.* 66.2 (2018), pp. 853–854.
- [37] Woojin S Kim et al. “Deletion of Abca7 increases cerebral amyloid- β accumulation in the J20 mouse model of Alzheimer’s disease”. en. In: *J. Neurosci.* 33.10 (Mar. 2013), pp. 4387–4394.
- [38] Yuhong Fu et al. “ABCA7 Mediates Phagocytic Clearance of Amyloid- β in the Brain”. en. In: *J. Alzheimers. Dis.* 54.2 (Sept. 2016), pp. 569–584.
- [39] Tomonori Aikawa et al. “ABCA7 haplodeficiency disturbs microglial immune responses in the mouse brain”. en. In: *Proc. Natl. Acad. Sci. U. S. A.* 116.47 (Nov. 2019), pp. 23790–23796.
- [40] Tomonori Aikawa et al. “ABCA7 Regulates Brain Fatty Acid Metabolism During LPS-Induced Acute Inflammation”. en. In: *Front. Neurosci.* 15 (Apr. 2021), p. 647974.

- [41] Mariet Allen et al. “loss-of-function variants, expression, and neurologic disease risk”. en. In: *Neurol Genet* 3.1 (Feb. 2017), e126.
- [42] Yue Liu et al. “Plasma lipidome is dysregulated in Alzheimer’s disease and is associated with disease risk genes”. en. In: *Transl. Psychiatry* 11.1 (June 2021), p. 344.
- [43] Logan Brase et al. “Single-nucleus RNA-sequencing of autosomal dominant Alzheimer disease and risk variant carriers”. en. In: *Nat. Commun.* 14.1 (Apr. 2023), p. 2314.
- [44] Joel W Blanchard et al. “APOE4 impairs myelination via cholesterol dysregulation in oligodendrocytes”. en. In: *Nature* 611.7937 (Nov. 2022), pp. 769–779.
- [45] Faten A Sayed et al. “AD-linked R47H-TREM2 mutation induces disease-enhancing microglial states via AKT hyperactivation”. en. In: *Sci. Transl. Med.* (Dec. 2021).
- [46] Brie Wamsley et al. “Molecular cascades and cell type-specific signatures in ASD revealed by single-cell genomics”. en. In: *Science* 384.6698 (May 2024), eadh2602.
- [47] Tushar Kamath et al. “Single-cell genomic profiling of human dopamine neurons identifies a population that selectively degenerates in Parkinson’s disease”. en. In: *Nat. Neurosci.* 25.5 (May 2022), pp. 588–595.
- [48] Lena Duchateau, Nicole Wawrzyniak, and Kristel Sleegers. “The ABC’s of Alzheimer risk gene ABCA7”. en. In: *Alzheimers. Dement.* (Mar. 2024).
- [49] Erik C B Johnson et al. “Large-scale proteomic analysis of Alzheimer’s disease brain and cerebrospinal fluid reveals early changes in energy metabolism associated with microglia and astrocyte activation”. en. In: *Nat. Med.* 26.5 (May 2020), pp. 769–780.
- [50] Hansruedi Mathys et al. “Single-cell transcriptomic analysis of Alzheimer’s disease”. en. In: *Nature* 570.7761 (June 2019), pp. 332–337.
- [51] Gwyneth M Welch et al. “Neurons burdened by DNA double-strand breaks incite microglia activation through antiviral-like signaling in neurodegeneration”. en. In: *Sci Adv* 8.39 (Sept. 2022), eabo4662.
- [52] Aravind Subramanian et al. “Gene set enrichment analysis: a knowledge-based approach for interpreting genome-wide expression profiles”. en. In: *Proc. Natl. Acad. Sci. U. S. A.* 102.43 (Oct. 2005), pp. 15545–15550.
- [53] Hansruedi Mathys et al. “Single-cell atlas reveals correlates of high cognitive function, dementia, and resilience to Alzheimer’s disease pathology”. en. In: *Cell* 186.20 (Sept. 2023), 4365–4385.e27.
- [54] Le Le Thi My et al. “Cryo-EM structures of human ABCA7 provide insights into its phospholipid translocation mechanisms”. en. In: *EMBO J.* (Dec. 2022).
- [55] John Jumper et al. “Highly accurate protein structure prediction with AlphaFold”. en. In: *Nature* 596.7873 (Aug. 2021), pp. 583–589.

- [56] Arne De Roeck et al. “Deleterious ABCA7 mutations and transcript rescue mechanisms in early onset Alzheimer’s disease”. en. In: *Acta Neuropathol.* 134.3 (Sept. 2017), pp. 475–487.
- [57] Seok-Man Ho et al. “Rapid Ngn2-induction of excitatory neurons from hiPSC-derived neural progenitor cells”. en. In: *Methods* 101 (May 2016), pp. 113–124.
- [58] Ajit S Divakaruni et al. “Analysis and interpretation of microplate-based oxygen consumption and pH data”. en. In: *Methods Enzymol.* 547 (2014), pp. 309–354.
- [59] Xia Gu et al. “Measurement of mitochondrial respiration in adherent cells by Seahorse XF96 Cell Mito Stress Test”. en. In: *STAR Protoc* 2.1 (Mar. 2021), p. 100245.
- [60] Ajit S Divakaruni and Martin Jastroch. “A practical guide for the analysis, standardization and interpretation of oxygen consumption measurements”. en. In: *Nat. Metab.* 4.8 (Aug. 2022), pp. 978–994.
- [61] Ajit S Divakaruni and Martin D Brand. “The regulation and physiology of mitochondrial proton leak”. en. In: *Physiology* 26.3 (June 2011), pp. 192–205.
- [62] Mika B Jekabsons and David G Nicholls. “In Situ Respiration and Bioenergetic Status of Mitochondria in Primary Cerebellar Granule Neuronal Cultures Exposed Continuously to Glutamate *”. en. In: *J. Biol. Chem.* 279.31 (July 2004), pp. 32989–33000.
- [63] Akansha Jain et al. “Mitochondrial uncoupling proteins protect human airway epithelial ciliated cells from oxidative damage”. en. In: *Proc. Natl. Acad. Sci. U. S. A.* 121.10 (Mar. 2024), e2318771121.
- [64] Rahul Kumar et al. “Uncoupling proteins as a therapeutic target for the development of new era drugs against neurodegenerative disorder”. en. In: *Biomed. Pharmacother.* 147.112656 (Mar. 2022), p. 112656.
- [65] Stéphane Demine, Patricia Renard, and Thierry Arnould. “Mitochondrial uncoupling: A key controller of biological processes in physiology and diseases”. en. In: *Cells* 8.8 (July 2019), p. 795.
- [66] Dmitry B Zorov et al. “Neuroprotective potential of mild uncoupling in mitochondria. Pros and cons”. en. In: *Brain Sci.* 11.8 (Aug. 2021), p. 1050.
- [67] Bruno S Monteiro et al. “Mitochondrial uncoupling proteins (UCPs) as key modulators of ROS homeostasis: A crosstalk between diabetes and male infertility?” en. In: *Antioxidants (Basel)* 10.11 (Oct. 2021), p. 1746.
- [68] Maiko Tomioka et al. “Lysophosphatidylcholine export by human ABCA7”. en. In: *Biochim. Biophys. Acta Mol. Cell Biol. Lipids* 1862.7 (July 2017), pp. 658–665.
- [69] Antonino Picataggi et al. “Specificity of ABCA7-mediated cell lipid efflux”. en. In: *Biochim. Biophys. Acta Mol. Cell Biol. Lipids* 1867.7 (July 2022), p. 159157.

- [70] Henry A Boumann et al. “The two biosynthetic routes leading to phosphatidylcholine in yeast produce different sets of molecular species. Evidence for lipid remodeling”. en. In: *Biochemistry* 42.10 (Mar. 2003), pp. 3054–3059.
- [71] Bo Wang and Peter Tontonoz. “Phospholipid remodeling in physiology and disease”. en. In: *Annu. Rev. Physiol.* 81.1 (Feb. 2019), pp. 165–188.
- [72] Yang Zhao et al. “Identification and characterization of a major liver lysophosphatidyl-choline acyltransferase”. en. In: *J. Biol. Chem.* 283.13 (Mar. 2008), pp. 8258–8265.
- [73] Henry A Boumann et al. “Depletion of phosphatidylcholine in yeast induces shortening and increased saturation of the lipid acyl chains: Evidence for regulation of intrinsic membrane curvature in a eukaryote”. en. In: *Mol. Biol. Cell* 17.2 (Feb. 2006), pp. 1006–1017.
- [74] Grzegorz Sienski et al. “disrupts intracellular lipid homeostasis in human iPSC-derived glia”. en. In: *Sci. Transl. Med.* 13.583 (Mar. 2021).
- [75] Benedikt Westermann. “Mitochondrial fusion and fission in cell life and death”. en. In: *Nat. Rev. Mol. Cell Biol.* 11.12 (Dec. 2010), pp. 872–884.
- [76] Arne De Roeck et al. “An intronic VNTR affects splicing of ABCA7 and increases risk of Alzheimer’s disease”. en. In: *Acta Neuropathol.* 135.6 (June 2018), pp. 827–837.
- [77] Ashling Giblin et al. “Neuronal polyunsaturated fatty acids are protective in ALS/FTD”. en. In: *Nat. Neurosci.* (Feb. 2025).
- [78] Naoto Takada et al. “Phospholipid-flipping activity of P4-ATPase drives membrane curvature”. en. In: *EMBO J.* 37.9 (May 2018), e97705.
- [79] Mike F Renne and Anton I P M de Kroon. “The role of phospholipid molecular species in determining the physical properties of yeast membranes”. en. In: *FEBS Lett.* 592.8 (Apr. 2018), pp. 1330–1345.
- [80] Harvey T McMahon and Emmanuel Boucrot. “Membrane curvature at a glance”. en. In: *J. Cell Sci.* 128.6 (Mar. 2015), pp. 1065–1070.
- [81] Yang Yang et al. “Plasma membrane curvature regulates the formation of contacts with the endoplasmic reticulum”. en. In: *Nat. Cell Biol.* 26.11 (Nov. 2024), pp. 1878–1891.
- [82] Stephanie Ballweg et al. “Regulation of lipid saturation without sensing membrane fluidity”. en. In: *Nat. Commun.* 11.1 (Feb. 2020), p. 756.
- [83] Roberto Covino, Gerhard Hummer, and Robert Ernst. “Integrated functions of membrane property sensors and a hidden side of the unfolded protein response”. en. In: *Mol. Cell* 71.3 (Aug. 2018), pp. 458–467.
- [84] Henry A Boumann et al. “The two biosynthetic routes leading to phosphatidylcholine in yeast produce different sets of molecular species. Evidence for lipid remodeling”. en. In: *Biochemistry* 42.10 (Mar. 2003), pp. 3054–3059.

- [85] Stephen Thomas Decker and Katsuhiko Funai. “Mitochondrial membrane lipids in the regulation of bioenergetic flux”. en. In: *Cell Metab.* 36.9 (Sept. 2024), pp. 1963–1978.
- [86] Jelske N van der Veen et al. “The critical role of phosphatidylcholine and phosphatidylethanolamine metabolism in health and disease”. en. In: *Biochim. Biophys. Acta Biomembr.* 1859.9 (Sept. 2017), pp. 1558–1572.
- [87] Yoshihiro Adachi et al. “Coincident phosphatidic acid interaction restrains Drp1 in mitochondrial division”. In: *Mol. Cell* 63.6 (Sept. 2016), pp. 1034–1043.
- [88] Daniele Bano, Dan Ehninger, and Giacinto Bagetta. “Decoding metabolic signatures in Alzheimer’s disease: a mitochondrial perspective”. en. In: *Cell Death Discovery* 9.1 (Dec. 2023), pp. 1–4.
- [89] Yao Zong et al. “Mitochondrial dysfunction: mechanisms and advances in therapy”. en. In: *Signal Transduction and Targeted Therapy* 9.1 (May 2024), pp. 1–29.
- [90] Stéphane Demine, Patricia Renard, and Thierry Arnould. “Mitochondrial Uncoupling: A Key Controller of Biological Processes in Physiology and Diseases”. en. In: *Cells* 8.8 (July 2019).
- [91] Anna Picca et al. “Mitophagy in human health, ageing and disease”. en. In: *Nature Metabolism* 5.12 (Nov. 2023), pp. 2047–2061.
- [92] Brenda Morant-Ferrando et al. “Fatty acid oxidation organizes mitochondrial supercomplexes to sustain astrocytic ROS and cognition”. en. In: *Nat Metab* 5.8 (Aug. 2023), pp. 1290–1302.
- [93] Diogo Trigo et al. “Mitochondria, energy, and metabolism in neuronal health and disease”. en. In: *FEBS Lett.* 596.9 (May 2022), pp. 1095–1110.
- [94] Anna Park et al. “Mitochondrial matrix protein LETMD1 maintains thermogenic capacity of brown adipose tissue in male mice”. en. In: *Nat. Commun.* 14.1 (June 2023), pp. 1–14.
- [95] Gerald S Shadel and Tamas L Horvath. “Mitochondrial ROS signaling in organismal homeostasis”. en. In: *Cell* 163.3 (Oct. 2015), pp. 560–569.
- [96] S S Korshunov, V P Skulachev, and A A Starkov. “High protonic potential actuates a mechanism of production of reactive oxygen species in mitochondria”. In: *FEBS Lett.* 416.1 (Oct. 1997).
- [97] Ulrik Wisløff et al. “Cardiovascular Risk Factors Emerge After Artificial Selection for Low Aerobic Capacity”. en. In: *Science* (Jan. 2005).
- [98] Zane B Andrews, Sabrina Diano, and Tamas L Horvath. “Mitochondrial uncoupling proteins in the CNS: in support of function and survival”. en. In: *Nat. Rev. Neurosci.* 6.11 (Oct. 2005), pp. 829–840.

- [99] Gabriel Robert and J Richard Wagner. “ROS-Induced DNA Damage as an Underlying Cause of Aging”. en. In: *Advances in Geriatric Medicine and Research* 4.3 (Oct. 2020).
- [100] Cédric Volanti, Jean-Yves Matroule, and Jacques Piette. “Involvement of oxidative stress in NF-kappaB activation in endothelial cells treated by photodynamic therapy”. en. In: *Photochem. Photobiol.* 75.1 (Jan. 2002), pp. 36–45.
- [101] T G Carty Jr et al. “Oxidative stress induces NF-kappaB nuclear translocation without degradation of IkappaBalph”. en. In: *Circulation* 100.19 Suppl (Nov. 1999), pp. II361–4.
- [102] R Schreck, K Albermann, and P A Baeuerle. “Nuclear factor kappa B: an oxidative stress-responsive transcription factor of eukaryotic cells (a review)”. en. In: *Free Radic. Res. Commun.* 17.4 (1992), pp. 221–237.
- [103] S I Gavrilova et al. “[Clinical efficacy and safety of choline alfoscerate in the treatment of late-onset cognitive impairment]”. ru. In: *Zh. Nevrol. Psichiatr. Im. S S Korsakova* 118.5 (2018), pp. 45–53.
- [104] Steven H Zeisel and Kerry-Ann da Costa. “Choline: an essential nutrient for public health”. en. In: *Nutr. Rev.* 67.11 (Nov. 2009), pp. 615–623.
- [105] Jan Krzysztof Blusztajn, Barbara E Slack, and Tiffany J Mellott. “Neuroprotective Actions of Dietary Choline”. en. In: *Nutrients* 9.8 (July 2017), p. 815.
- [106] Hansruedi Mathys et al. “Single-cell multiregion dissection of Alzheimer’s disease”. en. In: *Nature* 632.8026 (Aug. 2024), pp. 858–868.
- [107] Hui Wang et al. “Genome-wide epistasis analysis for Alzheimer’s disease and implications for genetic risk prediction”. en. In: *Alzheimers. Res. Ther.* 13.1 (Mar. 2021), p. 55.
- [108] Gibran Hemani, Sara Knott, and Chris Haley. “An evolutionary perspective on epistasis and the missing heritability”. en. In: *PLoS Genet.* 9.2 (Feb. 2013), e1003295.
- [109] David Haig. “Does heritability hide in epistasis between linked SNPs?” en. In: *Eur. J. Hum. Genet.* 19.2 (Feb. 2011), p. 123.
- [110] Or Zuk et al. “The mystery of missing heritability: Genetic interactions create phantom heritability”. en. In: *Proc. Natl. Acad. Sci. U. S. A.* 109.4 (Jan. 2012), pp. 1193–1198.
- [111] Michael S Haney et al. “APOE4/4 is linked to damaging lipid droplets in Alzheimer’s disease microglia”. en. In: *Nature* 628.8006 (Mar. 2024), pp. 154–161.
- [112] Matheus B Victor et al. “Lipid accumulation induced by APOE4 impairs microglial surveillance of neuronal-network activity”. en. In: *Cell Stem Cell* 29.8 (Aug. 2022), 1197–1212.e8.

- [113] Yuan-Ta Lin et al. “APOE4 causes widespread molecular and cellular alterations associated with Alzheimer’s disease phenotypes in human iPSC-derived brain cell types”. en. In: *Neuron* 98.6 (June 2018), 1141–1154.e7.
- [114] Arne De Roeck, Christine Van Broeckhoven, and Kristel Sleegers. “The role of ABCA7 in Alzheimer’s disease: evidence from genomics, transcriptomics and methylomics”. en. In: *Acta Neuropathol.* 138.2 (Aug. 2019), pp. 201–220.
- [115] F Ann Ran et al. “Genome engineering using the CRISPR-Cas9 system”. en. In: *Nat. Protoc.* 8.11 (Nov. 2013), pp. 2281–2308.
- [116] Emily R Miraldi et al. “Molecular network analysis of phosphotyrosine and lipid metabolism in hepatic PTP1b deletion mice”. en. In: *Integr. Biol. (Camb.)* 5.7 (2013), p. 940.
- [117] Steven A Sloan et al. “Generation and assembly of human brain region-specific three-dimensional cultures”. en. In: *Nat. Protoc.* 13.9 (Sept. 2018), pp. 2062–2085.
- [118] Carsen Stringer et al. “Cellpose: a generalist algorithm for cellular segmentation”. en. In: *Nat. Methods* 18.1 (Jan. 2021), pp. 100–106.
- [119] Noemí Esteras et al. “Visualization of mitochondrial membrane potential in mammalian cells”. In: *Methods in Cell Biology*. Methods in cell biology. Elsevier, 2020, pp. 221–245.
- [120] Alexandre Fort et al. “MBV: a method to solve sample mislabeling and detect technical bias in large combined genotype and sequencing assay datasets”. en. In: *Bioinformatics* 33.12 (June 2017), pp. 1895–1897.
- [121] Ilya Korsunsky et al. “Fast, sensitive and accurate integration of single-cell data with Harmony”. en. In: *Nat. Methods* 16.12 (Dec. 2019), pp. 1289–1296.
- [122] F Alexander Wolf, Philipp Angerer, and Fabian J Theis. “SCANPY: large-scale single-cell gene expression data analysis”. en. In: *Genome Biol.* 19.1 (Dec. 2018).
- [123] V A Traag, L Waltman, and N J van Eck. “From Louvain to Leiden: guaranteeing well-connected communities”. en. In: *Sci. Rep.* 9.1 (Mar. 2019), p. 5233.
- [124] Aravind Subramanian et al. “Gene set enrichment analysis: A knowledge-based approach for interpreting genome-wide expression profiles”. en. In: *Proc. Natl. Acad. Sci. U. S. A.* 102.43 (Oct. 2005), pp. 15545–15550.
- [125] B W Kernighan and S Lin. “An efficient heuristic procedure for partitioning graphs”. In: *Bell Syst. Tech. J.* 49.2 (Feb. 1970), pp. 291–307.
- [126] Zhisong He et al. “Comprehensive transcriptome analysis of neocortical layers in humans, chimpanzees and macaques”. en. In: *Nat. Neurosci.* 20.6 (June 2017), pp. 886–895.
- [127] Kristen R Maynard et al. “Transcriptome-scale spatial gene expression in the human dorsolateral prefrontal cortex”. en. In: *Nat. Neurosci.* 24.3 (Mar. 2021), pp. 425–436.

- [128] Ulrich Elsner. *Graph Partitioning: A Survey*. 1997.
- [129] George Karypis and Vipin Kumar. *METIS: A Software Package for Partitioning Unstructured Graphs, Partitioning Meshes, and Computing Fill-Reducing Orderings of Sparse Matrices*. Technical Report TR-97-065. Accessed: 2025-03-28. University of Minnesota, Department of Computer Science, 1997. URL: <http://glaros.dtc.umn.edu/gkhome/fetch/sw/metis/manual.pdf>.
- [130] Mariet Allen et al. “ABCA7 loss-of-function variants, expression, and neurologic disease risk”. en. In: *Neurol. Genet.* 3.1 (Feb. 2017), e126.
- [131] Stacy Steinberg et al. “Loss-of-function variants in ABCA7 confer risk of Alzheimer’s disease”. en. In: *Nat. Genet.* 47.5 (May 2015), pp. 445–447.
- [132] Erik C B Johnson et al. “Large-scale proteomic analysis of Alzheimer’s disease brain and cerebrospinal fluid reveals early changes in energy metabolism associated with microglia and astrocyte activation”. en. In: *Nat. Med.* 26.5 (May 2020), pp. 769–780.
- [133] Daifeng Wang et al. “Comprehensive functional genomic resource and integrative model for the human brain”. en. In: *Science* 362.6420 (Dec. 2018), eaat8464.
- [134] Oscar Franzén, Li-Ming Gan, and Johan L M Björkegren. “PanglaoDB: a web server for exploration of mouse and human single-cell RNA sequencing data”. en. In: *Database (Oxford)* 2019 (Jan. 2019).
- [135] Michael S Haney et al. “APOE4/4 is linked to damaging lipid droplets in Alzheimer’s disease microglia”. en. In: *Nature* 628.8006 (Apr. 2024), pp. 154–161.
- [136] A Lykidis, K G Murti, and S Jackowski. “Cloning and characterization of a second human CTP:phosphocholine cytidylyltransferase”. en. In: *J. Biol. Chem.* 273.22 (May 1998), pp. 14022–14029.
- [137] Jeffrey Cummings et al. “Alzheimer’s disease drug development pipeline: 2024”. nl. In: *Alzheimers Dement. (N. Y.)* 10.2 (Apr. 2024), e12465.
- [138] Gwyneth Welch and Li-Huei Tsai. “Mechanisms of DNA damage-mediated neurotoxicity in neurodegenerative disease”. en. In: *EMBO Rep.* 23.6 (June 2022), e54217.
- [139] Simone M Crivelli, Aisyulu Gaifullina, and Jean-Yves Chatton. “Exploring the role of mitochondrial uncoupling protein 4 in brain metabolism: implications for Alzheimer’s disease”. en. In: *Front. Neurosci.* 18 (Sept. 2024), p. 1483708.
- [140] Na Sun et al. “Human microglial state dynamics in Alzheimer’s disease progression”. en. In: *Cell* 186.20 (Sept. 2023), 4386–4403.e29.
- [141] Le Thi My Le et al. “Cryo-EM structures of human ABCA7 provide insights into its phospholipid translocation mechanisms”. en. In: *EMBO J.* 42.3 (Feb. 2023), e111065.